5-2012

Mott Transition and Electronic Structure in Complex Oxide Heterostructures

Jian Liu
University of Arkansas, Fayetteville

Mott Transition and Electronic Structure in Complex Oxide Heterostructures

Mott Transition and Electronic Structure in Complex Oxide Heterostructures

A dissertation submitted in partial fulfillment
of the requirements for the degree of
Doctor of Philosophy in Physics

By

Jian Liu
Nanjing University
Bachelor of Science in Physics, 2004
University of Houston
Master of Science in Physics, 2006

May 2012
University of Arkansas

Abstract

Strongly correlated electron systems, particularly transition metal oxides, have been a focus of condensed matter physics for more than two decades since the discovery of high-temperature superconducting cuprates. Diverse competing phases emerge, spanning from exotic magnetism to unconventional superconductivity, in proximity to the localized-itinerant transition of Mott insulators. While studies were concentrated on bulk crystals, the recent rapid advance in synthesis has enabled fabrication of high-quality oxide heterostructures, offering a new route to create novel artificial quantum materials.

This dissertation details the investigation on ultrathin films and heterostructures of $3d^7(t_{2g}^6 e_g^1)$ systems with spin (S=1/2) and orbital degeneracies. Perovskite $RNiO_3$ (R = rare earth) was chosen as a representative model, since its Ni 3+ valence corresponds to the low-spin $3d^7$ configuration. The heteroepitaxial growth of $RNiO_3$ ultrathin films and heterostructures was studied by laser molecular beam epitaxy. To achieve a layer-by-layer growth mode crucial for stabilizing the proper stoichiometry and creating sharp interfaces, a fast pumping plus interruption growth method was developed.

In addition to conventional transport measurement, resonant x-ray absorption spectroscopy was used to characterize the resulting electronic structures. The results demonstrate that the effect of polarity mismatch on the initial growth may lead to a chemical pathway for compensating the dipolar field. By utilizing the x-ray linear dichroic effect, an asymmetric heteroepitaxial strain-induced d orbital response in $LaNiO_3$ was revealed. Moreover, the interfacial lattice constraint was found to modulate the Ni-O covalency in $RNiO_3$ by simultaneously tuning the Madelung energy and the $p-d$ hybridization, leading to a self-doped mechanism that controls the collective phase behavior in $NdNiO_3$.

The electronic reconstructions in correlated quantum wells were also investigated in superlattices of $LaNiO_3/LaAlO_3$. In proximity to the confinement limit, a Mott-type metal-insulator

transition was observed with tendency towards charge ordering as a competing ground state. The interfacial Ni-O-Al bond was found to highly suppress the apical ligand hole density and result in confinement-induced orbital polarization. The key role of the interfacial boundary in selecting the many-body electronic ground state was directly demonstrated in quantum wells of $NdNiO_3$.

This dissertation is approved for recommendation
to the Graduate Council

Dissertation Director:

_____

Dr. Jak Chakhalian, Ph.D.

Dissertation Committee:

_____

Dr. Laurent Bellaiche, Ph.D.

_____

Dr. Surendra P. Singh, Ph.D.

_____

Dr. Paul Thibado, Ph.D.

_____

Dr. Ryan Tian, Ph.D.

Dissertation Duplication Release

I hereby authorize the University of Arkansas Libraries to duplicate this dissertation when needed for research and/or scholarship.

Agreed _____

Jian Liu

Acknowledgements

I would like to make sincere acknowledgement to all the wonderful friends and colleagues who have offered me scientific, technical or personal help during my graduate career.

This includes all the members in the Artificial Quantum Matter Laboratory. The last few years are memorable as we worked, studied, and grew together. I also want to thank all the collaborators not just for their tremendous contributions but also the invaluable knowledge of physics on various subjects that they have taught me. In particular, I am specially grateful for the generous support from Dr. John Freeland. In addition to being a great collaborator, he has always been a mentor and a close friend for me throughout my doctoral research. My special thank is also rendered to Dr. Jinghua Guo. As a gracious mentor, his support opened the door for me to resonant soft x-ray scattering. Without all these great people, the completion of this dissertation would not be possible.

In addition, I would like to thank the Raymond H. Hughes Graduate Fellowship and the Robert D. Maurer Physics Research Fund. I am extremely honored as a recipient of these prestigious awards which are enormously encouraging in this early stage of my career. I also want to thank the Advanced Light Source Doctoral Fellowship from the Lawrence Berkeley National Laboratory. It gave me precious and fantastic opportunities to extensively broaden my scope and get exposed to diverse state-of-the-art synchrotron techniques and cutting-edge research. I extremely appreciate the American Physical Society as well for giving me the Iris Ovshinsky Award. I am honored to be recognized by the research community.

As synthesis is significantly involved in my dissertation study, I want to thank Dr. Paul Chu and all the members of his group that I worked with, especially Ruling Meng, at the University of Houston. The priceless research experience there triggered my interests in sample growth and fundamentally changed my perspective as a physicist to material synthesis.

I genuinely appreciate all the giving and sharing from the Ramirez couple, Ralph and Karen Ramirez. They have treated my wife and me as their family since we came to the States and always

been there whenever we need assistance. It is my fortune to know them and I will always consider them as my family.

Finally, I would like to express my deepest gratitude to my advisor, Dr. Jak Chakhalian, for his guidance and support. It is my great honor to be his first doctoral student. He led me into the fascinating world of physics and polished me into a professional scientist. His marvelous vision and enthusiasm to science are always inspiring to me. I will never forget the time when we were chasing the Holy Grail of condensed matter physics.

Dedication

Dedication to my lovely wife, Yi, and my wonderful parents, Shisen and Hong.

Contents

Chapter 1

Introduction

1.1 Correlated Oxides

Complex oxides are a class of solid state electronic systems that exhibit strong electron-electron interaction. According to the conventional band theory which has been the most successful quantum theory for solids, these materials are supposedly good conductors or metals with a partially filled conduction band. In reality, they are however often insulators where electrons are trapped locally on their parent atoms. The underlying mechanism is derived from the strong Coulomb repulsion among the conduction electrons. These materials usually involve electrons that are packed within the spatially confined d-shell of transition metal elements. As a result, these localized d-electrons display atomic-like behaviors in their charge, spin and orbital degrees of freedom. On the other hand, compared with other correlated electron systems, the presence of oxygen ions gives rise to rather strong hybridizations between their $2p$ states and the $3d$ states of the transition metal ions, and tends to delocalize the many-body effects of the heavy d-electrons. The fine balance between this strong $p-d$ hybridization and the strong correlation-driven localization results in a rich variety of exotic electronic and magnetic quantum phases that can emerge at significantly high temperatures.

Another compelling character of complex oxides is the diversity of the available compounds, especially those consisting of the abundant transition metal elements in the $3d$ row. This diversity can also be attributed to the existence of various types of structures of the metal-oxygen network. One of most attractive classes is the perovskite structure named after the eminent Russian mineralogist, Count Lev Alexevich von Peroski. Perovskite oxides have a common formula as ABO_3 with a cubic or near cubic structure (see Fig. 1.1) [103]. Due to the distribution of the oxygen ions, there are the two different kinds of atomic sites for the metal ions which are often referred as the

A-site and the B-site. Specifically, transition metal ions often take the B-site surrounded by six oxygen ions in a BO_6 octahedron, while the A-site is occupied by rare earth elements. As a result, the perovskite structure can be view as a three dimensional (3D) cubic network of corner-sharing BO_6 octahedra with the A-sites on the centers of the cubes.

One of the major advantages of the perovskite structure is its great susceptibility to structural distortion away from the perfect cubic setting. The most common distortion comes from different cation ion radiuses, r_A and r_B. In an ideal cubic lattice, r_A and r_B are required to satisfy $r_A + r_O = \sqrt{2}(r_B + r_O)$, where r_O is the oxygen ionic radius. Whenever r_A and r_B deviate from this relation, the cubic unit cell will be distorted. The amount of the distortion can be quantified with a tolerant factor t which is defined as

$$t = \frac{r_A + r_O}{\sqrt{2}(r_B + r_O)} \tag{1.1}$$

. While $t = 1$ for zero distortion or a perfect cubic unit cell, t is typically smaller than one. In this case, to fill the void between the A-site and oxygen ions, the octahedral network will distort by rotating the octahedra around the cubic axe so that the oxygen ions are pushed closer to the A-sites. The tolerance to this octahedral rotation is the reason that so many elements can be fit into the perovskite structure with different combinations. There are two important consequences of this rotation; one is the symmetry-lowering of the crystal structure from the cubic space group, while the other one is the reduction of the B-O-B bond angle from 180^o, which decreases the overlapping of the bridging oxygen p orbital with the orbitals on the two B-sites and hence lowers the probability of the carrier hopping across the bond. Tuning these properties by substituting the A-site with elements with different ionic radiuses but the same valence is called chemical pressure. Decreasing the tolerant factor or increasing the chemical pressure typically lowers the crystal symmetry in an order as cubic ($Pm\bar{3}m$) to rhombohedral ($R\bar{3}c$) to orthorhombic (Pbnm) (see Fig. 1.1). In an distorted structure, the original cubic building blocks are called pseudocubes.

Another important advantage of the perovskite structure is related to the fact that the cubic structure can be viewed as layered structures consisting of atomic planes that have rather high rotation symmetries. For example, the perovskite structure can be constructed by stacking alternating

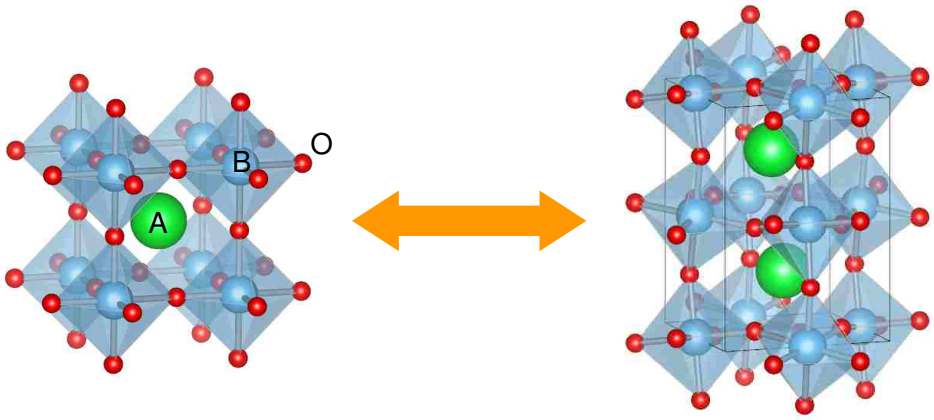

Figure 1.1: Perovskite ABO_3 structure. Left: the cubic unit cell. Right: the orthorhombic unit cell due to distortion. The orthorhombic unit cell is larger than the cubic unit cell due to the lower symmetry.

AO and BO_2 planes along the $< 100 >$ directions. In this case, the BO_2 planes are essentially square lattices and the oxygen-sites from the AO planes act as apical oxygen ions of the final octahedra. Other interesting directions also include $< 111 >$, $< 110 >$ and so on. The presence of these high-symmetry axes enable many different opportunities to create heterostructures with high-symmetry coherent interfaces. Its combination with the diversity of the available compounds brings perovskites to the center of the field of oxide heterostructures. However, before discussing oxide heterostructures, we will first describe the basis for understanding the electronic structure in correlated oxides.

1.1.1 Electronic Structure

Ionic Model

A good starting point for describing the microscopic picture of oxides (not limited to perovskite oxides) is the ionic model, because of the much larger electronegativity of oxygen compared with metal elements (here denoted as M). In this model, the metal ions give up their valence electrons to oxygen and become positively charged, while each oxygen ion gains two electrons to fill up its $2p$-shell; the formal amount of charges in the unit of $\mid e \mid$ on an metal ion is equal to its valence state. For instance, in NiO, the valence state of Ni is 2+ and O is 2-. As a result, when all these ions are

put together, there will be strong electrostatic interactions among them. The attractions between cations and anions drive the crystal formation and give rise to the cohesion energy gain. Thus, the metal ions are typically surrounded by negatively charged oxygen ions, and vice versa. The total electrostatic potential applied on a lattice site by all other ions is call the site Madelung potential V_{Mad}. While the summation over all surrounding ions is usually reduced by utilizing symmetry arguments, one can easily see that the primary contributions come from the near neighbors due to the inverse proportion to the ion-ion distance. Thus, the Madelung potential is negative on metal ions and positive on oxygen ions. But they are usually multiplied by a negative sign to describe electron energy since electrons are the real "glue" for solid formation.

Madelung potentials are the most dominant energies in ionic crystals typically on the order of tens of electronvolts, determining the structural stability. Without the Madelung potentials, e.g. in isolated atoms, it actually costs energy to dissociate electrons from metal atoms and bind them to oxygen atoms. In a solid, however, this energy barrier is reversed by the large difference in the site Madelung potentials between cations and anions, stabilizing the valence electrons on oxygen ions. The resulting energy required to excite an electron from oxygen ions back to metal ions is called the charge-transfer energy Δ and given by

$$\Delta = I(\mathrm{O}^{2-}) - A(\mathrm{M}^{v+}) + e[V_{\mathrm{Mad}}(\mathrm{M}) - V_{\mathrm{Mad}}(\mathrm{O})] - \frac{e^2}{d_{\mathrm{M-O}}} \tag{1.2}$$

where $I(\mathrm{O}^{2-})$ is the ionization energy for an O^{2-} ion and $A(\mathrm{M}^{v+})$ is the electron affinity energy for a metal ion M^{v+}. $d_{\mathrm{M-O}}$ is the distance between the two ions. As can be seen, while $I(\mathrm{O}^{2-})$ and $A(\mathrm{M}^{v+})$ are atomic properties, the Madelung potential difference $V_{\mathrm{Mad}}(\mathrm{M}) - V_{\mathrm{Mad}}(\mathrm{O})$ is the solid state effect that determines Δ, to first-order approximation. Higher-order corrections, due to the excitonic binding (the last term) for example, usually reduce the magnitude of Δ to a few electronvolts. In many highly ionic crystals, such as dielectrics, Δ is often approximately equal to the charge gap or band gap.

While the Madelung potential takes into account the monopole part of the site electrostatic

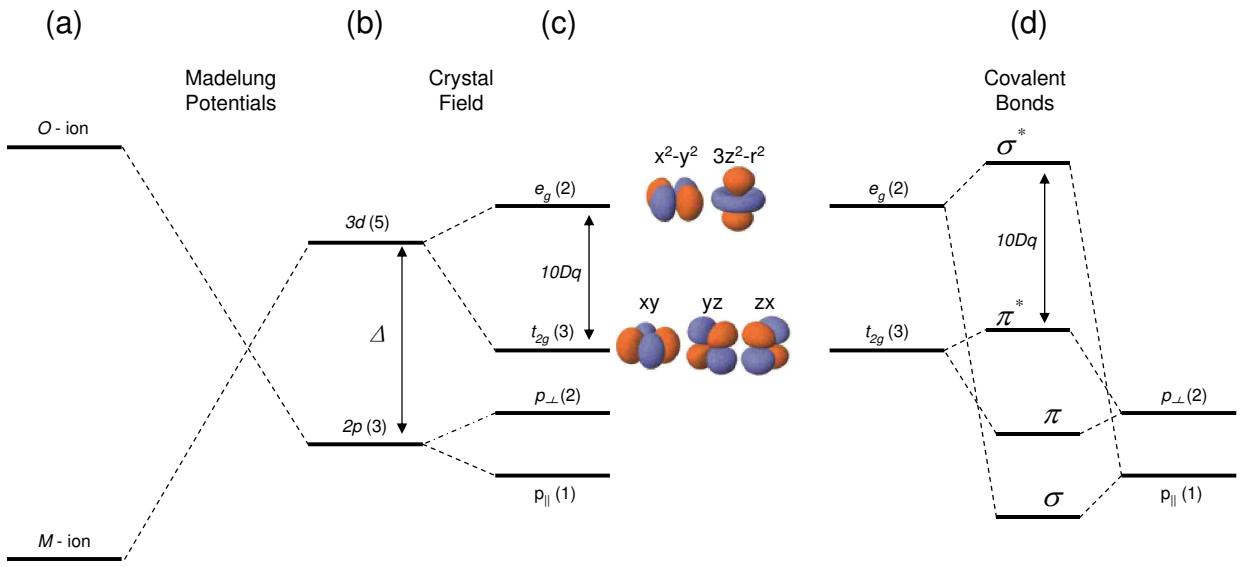

Figure 1.2: Covalent bonds formed by $3d$ and $2p$ orbitals. (a) a σ bond between an e_g orbital ($3z^2 - r^2$) and two apical p_z orbital. (b) a π bond between a t_{2g} orbital (xy) and four in-plane $p_{x,y}$ orbitals. To show the phases, orbitals are cut in half vertically and horizontally in (a) and (b), respectively.

potential, the finite number of the nearest-neighboring ions always has a nonspherical distribution, resulting in the higher-order multipole terms in the local field. This is particularly important when the valence electron orbitals of the centered site have anisotropic spatial distributions, e.g. p- and d-orbitals; the degeneracy of such an atomic orbital manifold is lifted by the multipole electric field from the near neighbors, which is called the crystal field effect. For instance, in a 180^o M-O-M bond, the three O $2p$ orbitals are splitting to a $2p_{\|}$ orbital parallel to the bond and the other two $2p_{\perp}$ orbitals that are normal to the bond and also normal to each other. The $2p_{\|}$ orbital has a downward energy shift because its nodes are pointing to the positively charged metal ions, while $2p_{\perp}$ orbitals are shifted upward. As such, in a MO_6 octahedron, the five d-orbitals of the transition metal ion are split into two groups, the e_g group and the t_{2g} group, under the cubic crystal field (see Fig. 1.2(c)). The e_g group has a two-fold degeneracy, consisting of the $3z^2 - r^2$ and $x^2 - y^2$ orbitals. The t_{2g} group has a three-fold degeneracy, consisting of the xy, yz and zx orbitals. The e_g and t_{2g} groups are shifted upward and downward, respectively, and their energy separation is denoted as $10Dq$. In addition, since the local crystal field breaks the spherical symmetry of an isolated

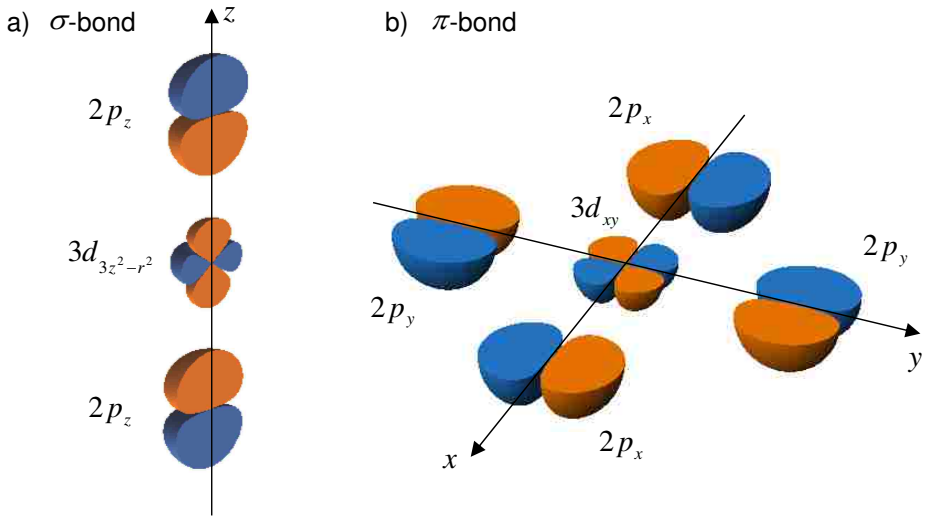

Figure 1.3: Covalent bonds formed by $3d$ and $2p$ orbitals. (a) a σ bond between an e_g orbital ($3z^2 - r^2$) and two apical p_z orbital. (b) a π bond between a t_{2g} orbital (xy) and four in-plane $p_{x,y}$ orbitals. To show the phases, orbitals are cut in half vertically and horizontally in (a) and (b), respectively.

ion, the original orbital angular moments from atomic physics are now quenched. Lowering the crystal field symmetry will further lift the remaining orbital degeneracy. This crystal field effect is particularly strong on transition metal ion because the radial extension of their d-orbitals is large enough for the electron to feel the anisotropic crystal field but also small enough for them to be considered as localized states.

$p-d$ Hybridization

From the ionic model discussed above, we have described the energy levels of all the atomic electron states. That is, all the diagonal matrix elements on the basis of atomic orbitals can be determined. On the other hand, the off-diagonal matrix elements are often nonzero due to the fact that the atomic states of the metal and oxygen ions are not orthogonal to each other. They have finite overlapping in their electron wavefunctions, i.e. $\langle \varphi_M | \varphi_O \rangle \neq 0$, which allows electrons to hop or resonate between different ions by hybridizing the p and d orbitals. The hopping integral $t_{pd} = \langle \varphi_M | H | \varphi_O \rangle$ quantifies the degree of covalent M-O bonding, where H is the single-electron Hamiltonian. In the case of a MO_6 octahedron described above, the e_g orbitals hybridize with

the $2p_{\|}$ orbitals to form the so-called σ bonds, while t_{2g} and $2p_{\perp}$ orbitals form the so-called π bonds (see Fig. 1.3). Other combinations vanish by the symmetry in the orbital phases. The $p-d$ hybridization in a covalent bond can be in-phase or out-of-phase; the former is lower in energy and called the bonding state while the latter is higher in energy and called the antibonding state, denoted as σ^* or π^*.

In most cases, because Δ is large enough, the $p-d$ hybridization can be treated as a perturbation and one often assign the bonding states to be the "new" $2p$ states and the antibonding states as the "new" M d states. In this approximation, the d and p states are considered to be raised and lowered, respectively, by t_{pd}^2/Δ. Moreover, due to the larger $p-d$ overlapping and stronger hybridization in the σ^* bonds than the π^* bonds ($t_{pd\sigma} > t_{pd\pi}$), the crystal field splitting $10Dq$ becomes larger than that in the pure ionic model. When many of these octahedra form a network in a crystal structure, the inter-octahedral hopping delocalizes these bonding or antibonding states and form dispersive σ, π, σ^* and π^* bands with bandwidths W proportional to $t_{pd\sigma}$ or $t_{pd\pi}$, which is described by the band theory. Due to the large radial extension of the oxygen orbitals, they may also form nonbonding bands by O-O overlapping without hybridizing with the metal ions.

Electronic Correlation

From above, one can see how energy bands are constructed by starting with the local electronic states and delocalizing them into extended Bloch wavefunctions. Filling the valence electrons in the local states and the bands should yield the same electronic structure, which is true for band insulators such as $SrTiO_3$ with full bonding bands and empty antibonding bands. However, for most transition metal oxides, the metal site has extra electrons remaining to be filled, resulting in a partially filled antibonding band. While one would expect them to be good metals or conductors, they are actually insulators in reality. The charge gap there is, thus, caused by a different nature from band formation. What was missing in the single-electron picture is the electron-electron correlation. As electrons experience their mutual repulsion, filling or moving one electron in the electronic structure affects all other electrons. In particular, due to the strong onsite Coulomb

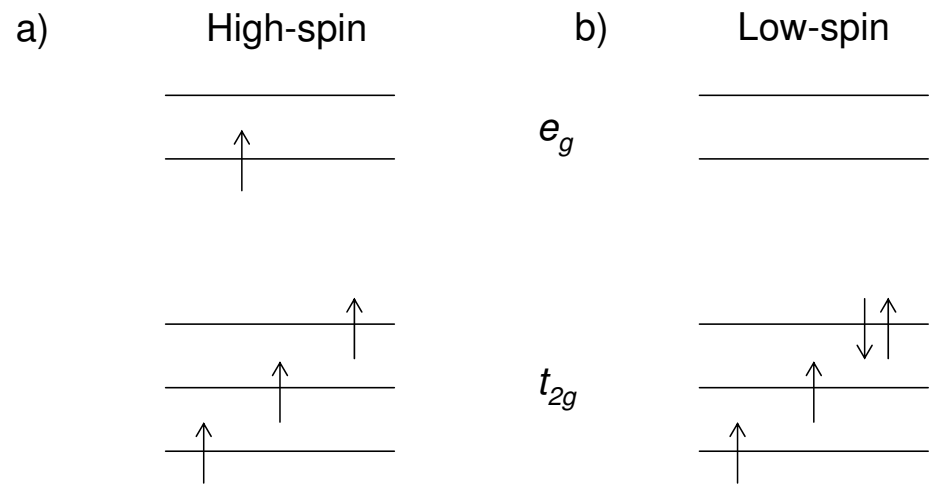

Figure 1.4: High-spin (a) and low-spin (b) states of the d^4 configuration in an octahedral crystal field.

repulsion U, the d-electrons are preferably distributed equally on every metal site in the ground state. Electron transfer from one site to another would cost extra energy U, causing the d-electron localization. This mechanism is described by the famous so-called Hubbard model, where the original partially filled conduction band is split into the so-called upper Hubbard band and lower Hubbard band separated by U. These bands are no longer single-electron dispersive bands but many-body states with strong local characters; the lower Hubbard band stands for the ground state with the same number of electrons on each site, while the upper Hubbard band denote excited states with an electron moved from one site to another. Note that, U is a self-consistent parameter and often expressed in terms of the competing energy W or t_{pd}, since the Coulomb repulsion is subject to screening in solid. This model contains the most basic ingredient of strongly correlated electron systems. Systems with insulating behavior driven by this correlation mechanism are called Mott insulators.

This correlation effect is particularly strong and important for transition metal oxides because the relatively short spatial extension of the d orbitals confines the electrons in a small region, and results in small t_{pd}. Meanwhile, since the five d orbitals can accommodate up to ten electrons, a partially filled d-shell have many possible local filling configurations which are called multiplet. The local ground state and excited states can be determined by considering the onsite electron-

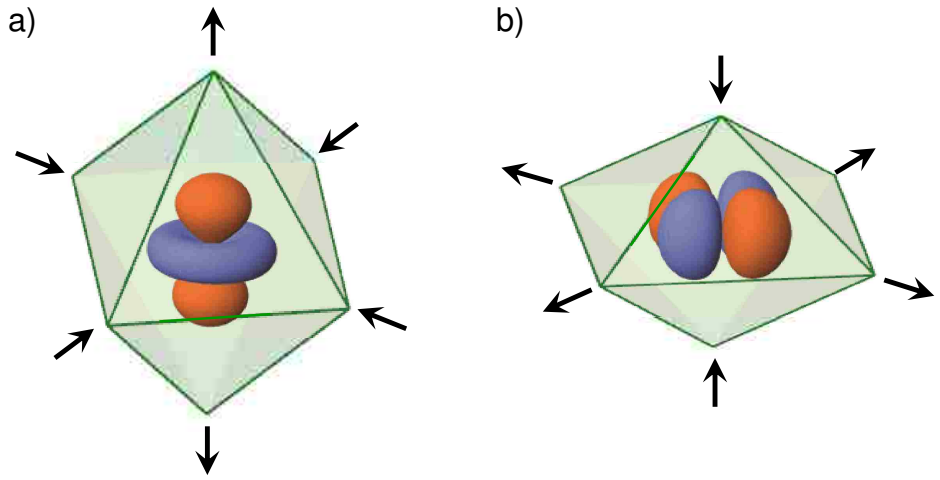

Figure 1.5: Jahn-Tell distortions for stabilization of the $3z^2 - r^2$ (a) and $x^2 - y^2$ (b) orbitals under octahedral crystal field.

electron interaction. To minimize the mutual repulsion, electrons prefer to occupy different orbitals and have their spins parallel aligned due to the exchange interaction. This is essentially the first Hund's rule and the energy gain for a pair of spin-parallel electrons is denoted as J_{H}, carrying the atomic characters. The presence of local magnetic moments is, thus, an essential character of strong correlation. The second and third Hund's rules are usually less important, especially for $3d$ transition metal oxides, because the orbital momentums are quenched by the crystal field effect as mentioned earlier. The crystal field splitting $10Dq$ also competes with J_{H} when the filling involves both the e_g and t_{2g} groups. For instance, in a d^4 configuration, e.g. a Mn^{3+} ion in an octahedral crystal field, while the first three d-electrons occupy each of the three t_{2g} orbitals with up spins, the forth electron has to overcome the crystal field splitting to take a spin-up state on one of the e_g orbitals (see Fig. 1.4(a)). Otherwise, when the crystal field is larger than the total Hund's rule stabilization energy ($3J_{\mathrm{H}}$), the forth electron has to take a spin-down state on one of the t_{2g} orbitals (see Fig. 1.4(b)). While the former case favored by the Hund's rule is called the high-spin state, the latter favored by the crystal field is called the low-spin state. There could also be intermediate-spin states when two or more electrons need to make such a selection in the competition, e.g. Co^{3+} ions.

With the spin state determined, the remaining degree of freedom in the onsite filling configura-

tion is orbital. From the example above, one can see that, in either high-spin or low-spin state, the forth electron has multiple orbitals to choose from due to the oribital degeneracy in the e_g and t_{2g} manifolds. This remanent orbital degeneracy occurs under crystal fields with high symmetry, such as the cubic crystal field of an uniform octahedron. While the spherically symmetric electrostatic (Madelung) potential prefers to equalize the bonds with the ligands and maintain this degeneracy, occupying one of the degenerate orbitals introduces an electric quadruple moment that would deform the crystal field and lift the orbital degeneracy. A typical example is when there is only one electron in the double degenerate e_g orbitals under an octahedral crystal field. The electron density in the lobes of the $3z^2 - r^2$ and $x^2 - y^2$ orbitals pushes the out-of-plane and in-plane oxygen ions away, respectively. This effect is eventually balanced by the energy loss in the elastic deformation of the lattice. The resulting elongation or compression tetragonal distortion on the octahedron in turn deforms the crystal field and lowers the energy of the $3z^2 - r^2$ or $x^2 - y^2$ orbital. This effect is called the Jahn-Teller (JT) effect, which predicts that a distortion must occur to lower the symmetry and remove the orbital degeneracy (see Fig. 1.5). Octahedrally coordinated Mn^{4+} (d^4), Cr^{2+} (d^4) and Cu^{2+} (d^9) ions are typical examples of strong JT effect on e_g orbitals.

Long-Range Orderings of Spin and Orbital

One may notice that, while the JT effect describe the removal of the local orbital degeneracy, it does not predict which orbital has a lower/higher energy. In solids, it often depends on the surrounding crystal structure. For instance, in a network of octahedra, elongation distortion of an octahedron may lead to compression distortion on the neighbors. The final result is a structural phase transition with orbital degeneracy removed on each site, which is called cooperative JT effect or orbital ordering. This is a reflection of how the local degrees of freedom of correlated d-electrons form long-range collective orderings with spontaneous broken symmetry.

Another example is the magnetic orderings for lifting the local spin degeneracy. While the correlation localizes d-electrons and results in local moments as discussed above, the total spin of each site fluctuates between the up and down states. The relatively small but finite hopping

amplitude, however, allows spins on different sites to communicate with each other. For instance, consider a 180^o M-O-M bond with one electron and one orbital on both M sites for simplicity. A virtual hopping, where the electron on the left hops to the right via the O ion and then an electron on the right hops back to the left, is allowed by the Heisenberg uncertainty principle, but only when the electrons on the two M sites have antiparallel spins due to the Pauli principle. By treating this virtual hopping as a second order perturbation, one can obtain an energy gain from this antiferromagnetic (AFM) exchange coupling. Extending this coupling to the entire lattice gives rise to an antiferromagnetic ordering, which is the most common magnetic ordering in Mott insulators. This exchange mechanism is called superexchange. The sign of the superexchange coupling may change to be ferromagnetic (FM), when changing the M-O-M bond to 90^o or there is orbital ordering. FM superexchange is usually relatively weak and generally driven by the Hund's rule when multiple orbitals on the same site are involved in the intermediate state of the virtual hopping. The determination of the sign of superexchange is summarized by the so-called Goodenough-Kanamori-Anderson rules.

There are also situations where the orbital ordering depends on the superexchange. This can be understood by considering the superexchange between two neighboring sites with orbital degeneracy on both. Different combinations of orbital configurations on the two site may have different virtual hopping processes, leading to differences in sign and/or strength of the exchange coupling. The one that has the largest energy gain is certainly more favorable. As a result, both spin and orbital degeneracies are removed by the superexchange. Generalizing it into the whole lattice will give rise to highly interrelated magnetic ordering and orbital ordering without involving JT distortion.

1.1.2 Mott Metal-Insulator Transition and the ZSA Scheme

With strong correlation turned on, we have seen how the behaviors of electrons and their multiple degrees of freedom are fundamentally different in Mott insulators from that described by the conventional band theory. The mutual couplings among the multiple degrees of freedom also af-

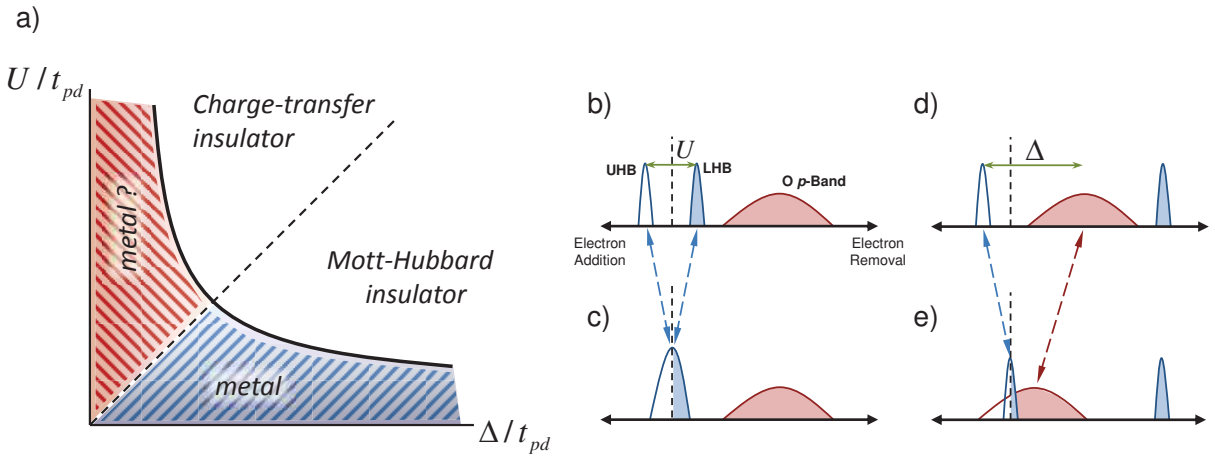

Figure 1.6: (a) ZSA diagram for transition metal compounds. Energy diagrams for addition and removal of electrons are showed and (b) to (e). (b) and (c) are Mott-Hubbard types with and without the charge gap, respectively. UHB and LHB denote the upper and low Hubbard bands, respectively. (d) and (e) are charge-transfer types with and without the charge gap, respectively.

ford numerous possibilities both at the atomic level and in the long-range orderings. While all these properties and physics originate from the local characters of correlated electrons, it is even more intriguing to ask what would happen when we delocalize the d-electrons or metallize Mott insulators. Delocalization of correlated electrons is in fact a long-standing fundamental question in condensed matter physics, because the localized-to-itinerant crossover connects regions and phases of distinct nature. For transition metal oxides, this crossover is the correlation-driven metal-insulator (MI) transition, which is also called the Mott transition. Driving a system across this transition allows one to investigate the underlying physics and access various potential orderings and phases, since the system does not have a straightforward solution for the ground state around the MI boundary and is subject to all kinds of instabilities.

While correlation is essential to the charge gap formation, there are two types of Mott insulators in transition metal oxides, due to the presence of oxygen ions. Their metallization by closing the charge gaps has very different consequences. This classification is summarized in the so-called Zaanen-Sawatzky-Allen (ZSA) diagram (see Fig. 1.6(a)) [109]. The first one is called the Mott-Hubbard type, where the charge excitation across the gap corresponds to moving one d-electron from its original site to another, i.e. $d^n d^n \longrightarrow d^{n+1} d^{n-1}$. The energy loss of this $d-d$ excitation

is essentially U (ignoring the onsite multiplet effect for simplicity). The charge gap in this case has the same character as that between the upper and lower Hubbard bands (see Fig. 1.6(b)), described by the Hubbard model discussed earlier. To approach the MI boundary of the Mott-Hubbard type, one can close the gap by reducing U or increasing the hopping amplitude t_{pd}. That is, by tuning the ratio of U and t_{pd}, one modulates the competition between correlation and delocalization, which is called bandwidth-control. Upon passing some critical value of U/t_{pd}, a metallic state is stabilized with a strong "memory" of the correlation (see Fig. 1.6(c)). Since the Hubbard model captures the essence of this correlation and is relatively simple, the MI transition of the Mott-Hubbard type has been intensively studied [42]. Many studies showed that such a bandwidth-control MI transition is first order because the two phases have distinct statistics and the thermodynamic properties often have to jump across the phase transition. In the weak correlation limit ($U/t_{pd} \ll 1$) around the bottom of the ZSA diagram, the simple metal region is recovered and the single-electron approximation becomes valid.

The second type is call the charge-transfer type, where the low-energy charge excitation corresponds to transferring a $2p$-electron on the ligand O ion to a M site, i.e. $d^n p^6 \longrightarrow d^{n+1} p^5 \equiv d^{n+1}\underline{L}$ ($\underline{L}$ denotes a ligand hole). The energy cost here is the charge-transfer energy Δ described in Eq. 1.2 in the ionic model. In contrast to band insulators where the electron is transferred to a single-electron state, the correlation effect here is integrated into Δ via the affinity energy $A(\mathrm{M}^{v+})$ of the transition metal site. The charge gap is, thus, formed between the broad occupied O band and the upper Hubbard band (see Fig. 1.6(c)). This situation occurs when it takes less energy to remove an electron from an O^{2-} ion than from a M^{v+} ion; $\Delta < U$ for the charge-transfer type versus $\Delta > U$ for the Mott-Hubbard type. Therefore, the charge-transfer type is often found with high oxidation states, i.e. large v, or late transition metals, e.g. Co, Ni and Cu. When $U, \Delta \gg t_{pd}$, both types are deep inside the Mott insulating phase and are qualitatively the same with localized d-electrons and spin moments, since the O $2p$ states are always filled. Quantitative differences are reflected in the their low-energy dynamics, such as different virtual hopping intermediate states with/without involving oxygen ions and consequently different superexchange strengths.

When the charge gap is closed at a small Δ, the localized d^{n+1} states would be merged into the O continuum band in the charge-transfer type, drastically different from the Mott-Hubbard type. In this process, a significant amount of ligand holes are created by transferring $2p$-electrons onto the d states (see Fig. 1.6(d)), which is call self-doping [46]. One may expect the system becomes a metal with mobile $2p$-holes and extra local moments since the $d^{n+1}\underline{L}$ configuration becomes lower in energy than the d^n configuration and dominant in the ground state. Meanwhile, when Δ is largely reduced, t_{pd} can no longer be considered as a small effect. Even a small t_{pd} could cause substantial covalent mixing of the p and d characters in the wavefunctions, leading to a strongly hybridized ground state of the d^n and $d^{n+1}\underline{L}$ configurations. Describing hybridization between local correlated states and extended band-like states is, however, extremely challenging, because the former is described in real space while the later is characterized in the moment space. The nature of the MI boundary in the charge-transfer region is thus much less understood than that of the Mott-Hubbard type. In addition, the presence of the ligand holes may also modify the exchange coupling between the metal sites. For instance, with a ligand hole in a 180^o M-O-M bond, the $2p$-hole will be filled by a d-electron from either side in the intermediate state of the virtual hopping, favoring a FM coupling between the M sites over the AFM superexchange. This exchange mechanism involving a ligand hole is called covalent exchange.

1.2 Heterostructure and Interface

1.2.1 Mismatches at Correlated Interface

As we have discussed in the previous section, the charge, spin, orbital and lattice degrees of freedom are strongly coupled with each other in correlated electron systems. As a result, a small perturbation on one of them may lead to drastic modifications to the others and the macroscopic properties of the whole system. Prominent examples include the famous colossal magnetoresistance (CMR) manganites and high-T_c superconductive cuprates. While the great tunability of correlated oxides is often accessed in bulk by using control parameters, such as chemical doping, chemical pressure, hydrostatic pressure, magnetic field, electric field and so on, heterostructuring

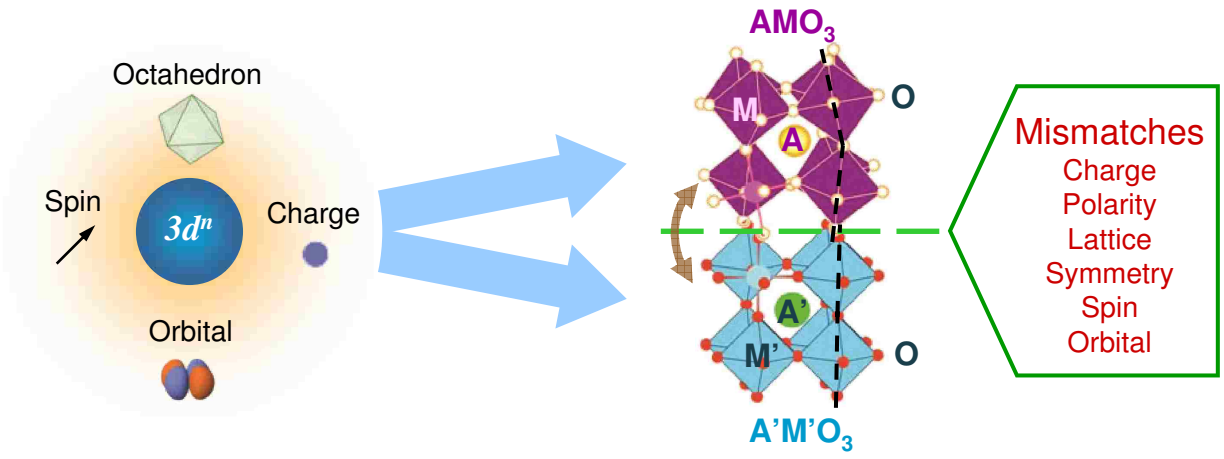

Figure 1.7: Interfacing complex oxides with different characters creates mismatches in the multiple degrees of freedom of the *d*-electrons.

has emerged as a new fascinating playground for manipulating correlated electrons and stabilizing novel quantum states that do not exist in the bulk. The fruitful physics in oxide heterostructures originates from the mismatches of the multiple degrees of freedom at interfaces which break the translational symmetry of the constituting materials. To resolve these mismatches, reconstructions must set in and the interface essentially becomes a new correlated system.

A notable example is the two dimensional (2D) electron gas at the $LaAlO_3/SrTiO_3$ interface [69], which is one of the most intensively and extensively studied oxide heterostructures. The presence of this conductive interface between two band insulators was first believed to be a result of resolving the polarity mismatch between systems with different charge structures, e.g. $La^{3+}Al^{3+}O_3^{2-}$ versus $Sr^{2+}Ti^{4+}O_3^{2-}$, by transferring electrons from the surface to the interface [69]. A supporting evidence for this scenario is the observed minimum thickness of the polar structure required for the presence of metallicity [97]. Later on, the interface was, however, found to have severe intermixing of cations and oxygen deficiency [65, 102], which introduce carriers in $SrTiO_3$. This doping effect is likely related to the low oxygen partial pressures used to grow the heterostructure. In fact, it was recently reported that the thermal cycle of the growth alone can metallize the surface of $SrTiO_3$ without depositing the $LaAlO_3$ layer [59]. Moreover, spectroscopic studies have not found the polar electric field within the polar structure. Nevertheless, the numerous studies has

showed rather unusual electronic, magnetic and structural properties of this 2D electron gas [9]. The underlying physics is still under debate since the system is subject to multiple effects including polarity mismatch, nonstoichiometry, disorder and the correlation nature of the d-band in $SrTiO_3$. We will have more discussion on the issue of polarity mismatch in Chapter 3.

Another fabulous example is the interface between high-T_c superconductive cuprates and CMR manganites, such as $YBa_2Cu_3O_7$ (YBCO) and $La_{2/3}Ca_{1/3}MnO_3$ (LCMO), respectively. Due to the incompatibility of d-wave superconductivity and ferromagnetism, these two order parameters were found to mutually suppress each other in YBCO/LCMO heterostructures with a large length scale [88, 36]. On the other hand, a coupling of the superconducting layers was observed and has been attributed to a long range proximity effect [76]. Moreover, a surprising inverse spin-switch effect, where parallel alignment of the ferromagnetic LCMO layers enhances the transition temperature of the sandwiched YBCO layer, has been recently found [66]. To account for these unconventional long-range proximity effects, the microscopic exchange interaction [13, 91, 22] and orbital reconstruction [12] at the YBCO/LCMO interfaces are believed to be crucial [82]. The microscopic studies of the interfacial couplings in YBCO/LCMO superlattices have showed a net magnetic moment induced in the interfacial CuO_2 plane with an intriguing AFM coupling to Mn [13, 91, 101] (see Fig. 1.8(a)). This antiparallel spin alignment was surprising since virtual hopping would predict FM coupling according to the Goodenough-Kanamori-Anderson rules. It was then explained by the observations of interfacial electronic reconstruction and orbital reconstruction [12]; the strong covalent Cu-O-Mn bond creates an interfacial antibonding state (see Fig. 1.8(b)) that has a significant weight of the Cu $3z^2 - r^2$ orbital and draws the holes from the Cu $x^2 - y^2$ orbital. This delicate picture manifests the interfacial reconstructions of all degrees of freedom and their mutual coupling.

While the two examples above involve interfaces between materials with very different chemical compositions, there are also prototypical cases that are primarily designed to induce charge mismatch. These interfaces are formed between materials within the same family but with different A-site cations, such as $LaTiO_3/SrTiO_3$, $LaMnO_3/SrMnO_3$, and $La_2CuO_4/(La,Sr)_2CuO_4$. Since

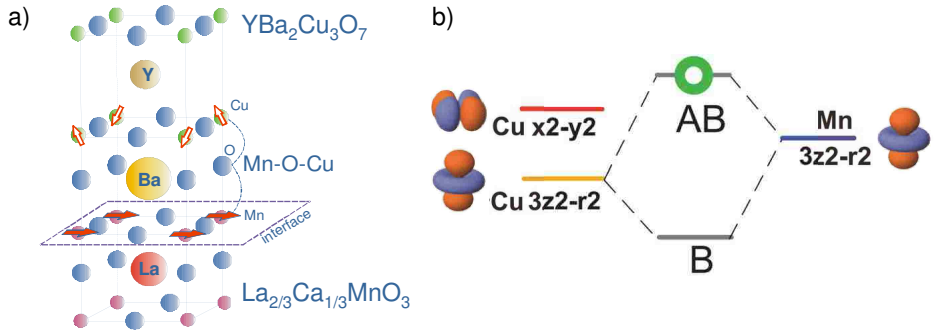

Figure 1.8: (a) interfacial structure between YBCO and LCMO from Ref. [13]. (b) scheme of covalent bonding between Cu and Mn from Ref. [12].

La and Sr have different charge counts, these materials are often randomly mixed in the bulk to achieve mixed valence of the transition metal ions in solid solutions; the two valence states of the transition metal ions are distributed relatively uniformly throughout the system. This chemical doping in correlated oxides has been showed to result in metal-insulator transition, CMR effect, high-T_c superconductivity, and so on [42]. However, the random distributions of La and Sr also lead to local disorders. This can be resolved by artificially separating them in heterostructures where the mixed valence is induced via interfacial charge transfer. Moreover, the doped charge carriers are now confined to a quasi-2D region near the interface. As a result, conductive interfaces between a Mott insulator and a band insulator were found in $LaTiO_3/SrTiO_3$ [70]. CMR effect and enhanced magnetism were also observed in $LaMnO_3/SrMnO_3$ [55]. Superconductivity with enhanced T_c was showed to exist within only one atomic plane near the interface of $La_2CuO_4/(La,Sr)_2CuO_4$ [52].

Compared with interfacial charge transfer which can be more or less comprehended as a doping effect, magnetic interfaces with primary mismatches between the spin degree of freedom appear to be more intriguing and challenging to probe. An early example is the FM interface between an AFM insulator $CaMnO_3$ and a paramagnetic metal $CaRuO_3$ [94]. Another appealing case is the exchange bias effect between FM $La_{2/3}Sr_{1/3}MnO_3$ and multiferroic $BiFeO_3$. While exchange bias is a well known phenomenon under interfacial magnetic frustration, the use of multiferroic $BiFeO_3$ enables one to control the exchange bias effect via electric field instead of magnetic field [104].

1.2.2 Interfacing $RNiO_3$-based e_g^1 System

The emergence of novel properties at complex oxide heterostructures interfaces stimulates the ultimate goal of rational design for new correlated electron phases of matter. However, the combination of the many-body physics and the multicomponent interfacial environment imposes formidable challenges to material theory. While state of the art theoretical tools such as density functional theory and dynamical mean field theory have been extensively used to study and predict the behaviors of oxide interfaces, they often experience difficulties even in interpreting the constituting materials in the bulk. It takes close cooperations among many-body techniques, band structure calculations and quantum chemical methods to establish a bottom-up approach to build correlated interfaces with desired properties.

Prompted by the discovery of high-T_c superconductivity in cuprate compounds there has been a surge of activity to discover materials with even higher transition temperatures [4]. Towards this grand challenge, a recent proposal has been put forward to use heterostructuring and orbital engineering to construct a cuprate-like e_g^1 system without Cu. The proposed prototype employs a quantum well structure that involves alternating unit-cell thin layers of a correlated metal $LaNiO_3$ (LNO) and band-gap dielectric $LaAlO_3$ (LAO) along the (001) direction [14] (see Fig. 1.9). It utilizes the $3d^7$ low-spin configuration (S=1/2) of the Ni 3+ valence state in perovskite nickelates $RNiO_3$ (R = rare earth) where the single unpaired electron occupies the degenerate e_g orbitals. Both *t-J* model and LDA+DMFT calculations [14, 34] suggest that the quantum confinement together with the electronic correlations should make it possible to localize or empty the $3z^2 - r^2$ band leaving the e_g electron in the $x^2 - y^2$ band. This is similar to cuprates which have the single unpaired hole occupying the $x^2 - y^2$ band. Epitaxial strain is also suggested as a mean of the orbital control to manipulate the $3z^2 - r^2$ orbital to appear above $x^2 - y^2$ and play the analogous role of the axial orbital of the high-T_c cuprates. As a result, a 2D spin-half Mott insulating state with AFM coupling in the NiO_2 plane may be realized, akin to the parent phase of the CuO_2 plane in the high-T_c cuprates.

While quantum confinement is the key in this proposed model system, it has actually been a

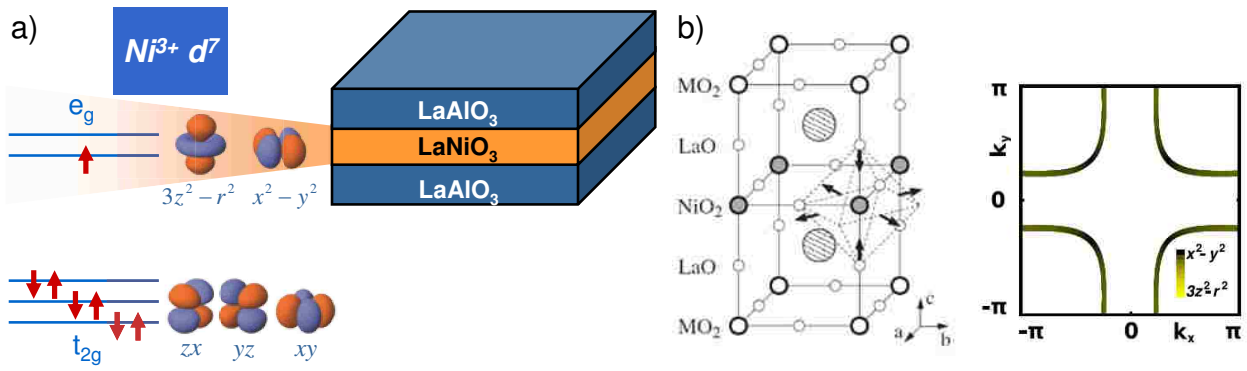

Figure 1.9: (a) electronic configuration of the $3d^7$ low-spin configuration of the Ni 3+ valence state and a quantum well structure consisting of a LNO layer confined by LAO. (b) the proposed structure with alternating unit-cell thin layers of LNO and LAO along the (001) direction and the resulting cuprate-like 2D Fermi surface.

powerful way to create novel 2D electronic systems for a long time. In general, it constrains the electrons by squeezing a 3D system along one of the directions. When the size of the confinement reaches the wavelength of the electrons, the system is fundamentally changed to a new regime with a very different electronic structure. This method has been applied to many conventional materials such as semiconductors. In Mott quantum well structures, an ultrathin electronically active slab of correlated oxide is then constrained in an epitaxial heterostructure where the vertical hopping of the d-electrons is typically suppressed by dielectric oxide blocks, e.g. LAO. The difficulties in synthesis have been the obstacle for applying this method on complex oxides. But the addition of correlation into the underlying physics makes Mott quantum wells even more interesting. Recent achievements in high-quality growth of oxide heterostructures have indeed paved a way to explore this direction. In fact, recent work on quantum wells of t_{2g} systems have found competing pathways to polarity compensation [95], confinement-induced orbital reconstruction [89] and dimensionality-controlled metal-insulator transition [108]. Appealing many-body phenomena have also been predicted, including proposals of half-metallic semi-Dirac points [74] as well as various engaging orderings of charge, spin and orbital [43].

Although relatively less experimental study has been devoted to quantum wells of e_g electrons, e_g^1 systems are known to have rich physics demonstrated by the prominent examples of CMR

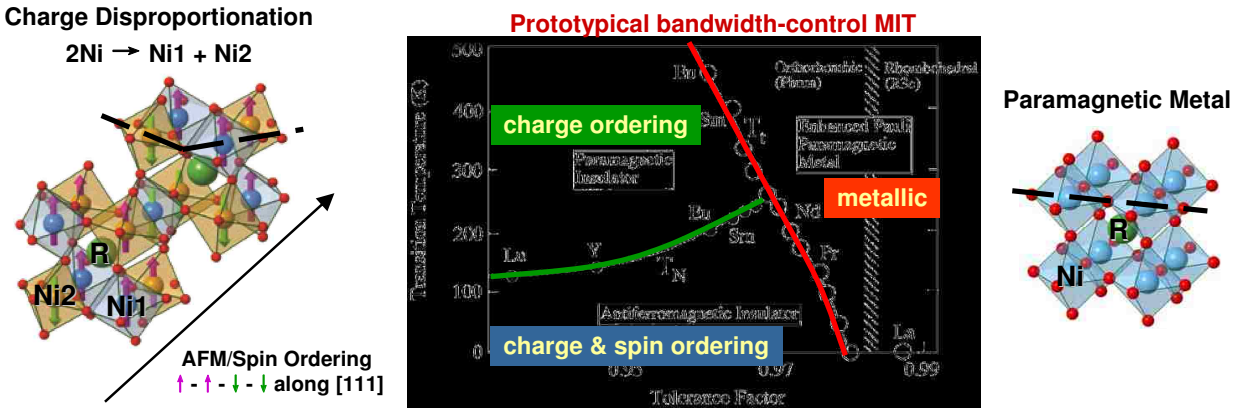

Figure 1.10: Bulk phase diagram of $RNiO_3$ with temperature versus the tolerant factor from Ref. [111]. The left and right pictures show the perovskite structures with different degrees of distortion. While the right corresponds to the metallic phase, the left shows the charge ordering and spin ordering in the AFM insulating phase.

manganites and high-T_c cuprates in the bulk. Therefore, in addition to serving as a test platform for the proposed cuprate-like scenario mentioned above, $RNiO_3$-based quantum wells represent a prototypical e_g^1 system for exploring different latent quantum phases and building the foundation of functional tailoring in Mott quantum wells. In fact, other possible novel quantum states have been suggested, such as exotic topological phases in quantum wells of LNO confined along the (111) direction [81, 107]. On the other hand, before investigating quantum wells, it is crucial and instructional to review the physics in $RNiO_3$ revealed by bulk studies.

The correlated electron behaviors of $RNiO_3$ can be summarized in the bulk phase diagram with temperature versus the tolerant factor or A-site ionic radius showed in Fig. 1.10. It can be immediately seen that the system exhibits a well controlled metal-insulator boundary which can be related to the degree of internal structural distortion induced by the chemical pressure. The smaller the rare earth ion, the stronger the distortion away from the ideal cubic perovskite structure. As a result, the reducing Ni-O-Ni bond angle suppresses the carrier hopping and enhances the robustness of the insulating state. In particular, LNO is the only member that has a paramagnetic metallic ground state with a rhombohedral structure, while all other members are AFM insulators at low temperatures with a monoclinic structure and paramagnetic metals at high temperatures with a orthorhombic structure. For members with the R = Sm or smaller rare earth, there is also an

intermediate paramagnetic insulating phase in between. That is the AFM transition temperature is smaller than the metal-insulator transition temperature. These two transition temperatures coincide when R = Pr and Nd. Phenomenologically, these two different cases can be distinguished by the presence/absence of thermal hysteresis [11, 58]; the coincided transition is a first order transition while both transitions are second order when they are separated in temperature.

Moreover, within the insulating state, unlike conventional 3D Mott insulator with a G-type AFM ordering, $RNiO_3$ has rather peculiar orderings of charge and spin. Specifically, upon entering the insulating phase, $RNiO_3$ displays a charge ordering pattern consists of a rock-salt-type ordering of two different octahedra with different Ni-O bond lengths [2, 92]. It is believed that this charge ordering occurs via Ni charge disproportionation ($2Ni^{III} \longrightarrow Ni^{II} + Ni^{IV}$). In the AFM state, the magnetic structure has an E'-type spin ordering with equal numbers of FM and AFM Ni-O-Ni bonds, forming a peculiar $\uparrow - \uparrow - \downarrow - \downarrow$ stacking sequence of FM planes along the pseudo-cubic (111) direction [26]. In the cubic notation, it is equivalent to a 4x4x4 super cell.

These unusual orderings in the Mott insulating phase strongly indicates a nontrivial interrelation between the electronic structure and the multiple degrees of freedom of the d-electrons. In particular, the presence of charge ordering raises questions on the nature of the charge gap, i.e. charge ordering versus onsite Coulomb repulsion. Moreover, the presence of FM exchange couplings in the unusual spin ordering was originally considered as a sign of orbital ordering or cooperative Jahn-Teller effect which typically results in local anisotropy in exchange paths. But no significant e_g orbital splitting has been observed, ruling out this possibility. This raises another debate on whether the orbital degeneracy of the localized e_g electrons is lifted. It was proposed that the orbital degeneracy is lifted via the charge disproportionation of the e_g^1 configurations into e_g^2 (high-spin Ni^{II}) and e_g^0 (low-spin Ni^{IV}) sites [56]. While this process appears to be energy costly, it can be stabilized due to the fact that $RNiO_3$ belongs the charge-transfer type in the ZSA scheme with a small charge-transfer energy [60]. That is, the self-doping mechanism discussed in the previous section strongly mixes and hybridizes the $3d^7$ and $3d^8\underline{L}$ configurations, and the strong $p-d$ charge fluctuation may easily stabilize the Ni^{IV} state as the energetically favorable $3d^8\underline{\underline{L}}$ configu-

ration [61]. As described in the previous section, a significant amount of ligand holes on oxygen ions would then naturally explain the FM coupling as the covalent exchange interaction. More importantly, this picture signifies that the critical microscopic parameter in controlling $RNiO_3$ is the Ni-O covalency.

From the discussion above, we can see that even $RNiO_3$ has profound physics by itself that we have yet to fully understand. It again reflects on the intriguing complexity of correlated electron systems, which presents a large degree of ambiguity in selecting a specific electronic ground state for a Mott quantum well, despite its attractive structural simplicity. Thus, $RNiO_3$ is an ideal candidate for investigating the underlying mechanisms of every experimental control parameter in constructing artificial quantum materials. Furthermore, due to its proximity the metal-insulator transition, its response in heterostructures will largely facilitate comprehending the fundamentals at correlated interfaces.

In this dissertation, to bridge the serious gap between our understanding from the bulk and the goal of rationally designed oxide heterostructure, we studied three most fundamental effects in experimentally realized correlated quantum wells, i.e. heteroepitaxial strain, dimensionality and interface coupling. We will start in Chapter 2 by describing the technique used to grow these heteroepitaxial ultrathin layers with *in situ* control and the resonant spectroscopic tool used to probe the electronic structures in these ultrathin layers in a multicomponent environment. Chapter 3 will demonstrate the applications of these methods on $RNiO_3$ and the importance of the growth in obtaining the desired heterostructures of $RNiO_3$. In Chapter 4, the unique effects of heteroepitaxial strain on the e_g orbital splitting, Ni-O covalency and the metal-insulator transition will be discussed in details. The results set the groundwork for studying more complicated heterostructures since lattice mismatch is inevitable at the film-substrate. Even if the lattice parameters are matched, there will be symmetry mismatch at the interface due to the nature of epitaxy. Subsequently, Chapter 5 focuses on the quantum wells of $RNiO_3$. In particular, in virtue of the digital control of the growth on the layer thickness, we will show the investigation on the dimensional crossover in Mott quantum wells. We will also elaborate the orbital response to confinement and demonstrate

the confinement as an alternative route to engineering orbital configuration. This chapter will be finalized by illustrating that the interfacial condition has a vital role in determining the collective ground state of Mott quantum wells. Chapter 6 then serves as a summary and an outlook for future directions of complex oxide heterostructures.

Chapter 2

Experimental Techniques

In this chapter we will introduce the experimental techniques that we use to study correlated interfaces in oxide heterostructures. We will start with the preparation of the most common perovskite substrate $SrTiO_3$ for obtaining atomically flat surfaces with a single termination. We then will discuss the ultrathin film deposition technique, laser molecular beam epitaxy (MBE), used in this dissertation study to create sharp epitaxial oxide interfaces. While oxide thin film deposition has been intensively studied since the discovery of high-temperature superconducting cuprates more than 20 years ago, it was only a few years ago that the new advances have enabled fine control of the growth with atomic precision. In particular, laser MBE has stood out as a powerful method due to its relatively simple structure and high applicability to oxides. It also provides *in situ* real-time monitoring of the surface quality and affords frequent changes of the target materials, which allows convenient exploration on the growth of interfaces of different material combinations.

In oxide heterostructures, it is formidably challenging to characterize the ultrathin layers that are typically a few nanometers thick. Moreover, since interfaces are buried in multicomponent environment, advanced techniques play a critical role in understanding the underlying physics. While conventional methods, such as transport measurement, may still be useful to measure macroscopic properties, microscopic investigation in this dissertation study utilized resonant x-ray spectroscopy, especially x-ray absorption spectroscopy (XAS). As a core-level spectroscopy, XAS is very suitable for probing the local electronic structure described in Chaper 1 for transition metal oxides. With the available third-generation synchrotron facilities, brilliant x-ray sources with tunable energy and polarization are now available, facilitating the extensive application of XAS in nanostructures. We will discuss its basic mechanism and characters.

2.1 Preparation of Atomically Flat Surface of $SrTiO_3$ Substrates

To achieve high-quality growth of oxide heterostructures with sharp interfaces, one of the most important factor is the starting surface quality of the substrate. Surfaces of most commercially available oxide substrates are prepared by chemical-mechanical polishing. The surface roughness is usually less than half of the crystal lattice unit cell. Since perovskite-based oxides often have different atomic planes within the unit cell, the terminating surface plane is not uniquely selected. For instance, the surface of an as-received (001)-oriented $SrTiO_3$ substrate has a mixed SrO/TiO_2 termination (see Fig. 2.1) with a miscut angle of $< 0.3^o$. The growth and the properties of the resulting heterostructures may, however, strongly depends on the starting termination, which is reflected in the $LaAlO_3/SrTiO_3$ system where a 2D electron gas may be stabilized depending on the termination at the interface [69]. Thus, it is important to develop method or treatment to remove one of the two terminations and realize atomically flat surfaces. Since $SrTiO_3$ is probably the most widely used perovskite substrate, a standard treatment based on etching with buffered HF has been established [45]. But, because of the aggressive acidic nature of HF, this method is rather dangerous and often results in chemical damages to the substrate with defects and oxygen vacancies. We will discuss our newly developed HCl-based treatment, with which the single TiO_2-termination can be obtained with surface morphology akin to the HF-based method but less defective damage.

Before the etching treatment, it is important to remove surface impurities and dust particles by rinsing the substrates with ultra-high-purity acetone and ethanol in an ultrasonic bath. In order to achieve a single termination of $SrTiO_3$ substrates, the SrO atomic plane is then dissolved by first soaking the substrates in deionized water for 25 min. During this soaking procedure, the surface SrO forms a hydroxide complex $Sr(OH)\cdot xH_2O$, while the surface TiO_2 remain unchange because it is chemically stable with water. To increase the reactivity, the deionized water is kept at 70^oC in an ultrasonic bath. After that, the surface hydroxide complex groups are etched in an acid solution. This is traditionally accomplished by using buffered HF acid, which is, however, an extremely dangerous chemical and requires special setups. Instead, we developed a substitution with HCl

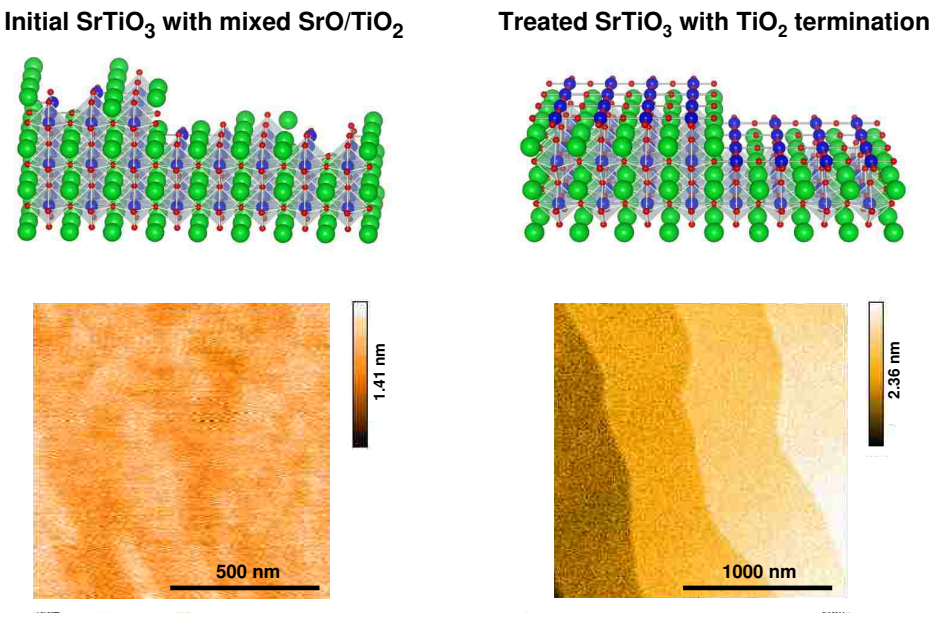

Figure 2.1: $SrTiO_3$ substrates. Left: as-received substrates with mixed SrO/TiO_2 termination. Right: treated substrates with TiO_2 termination and well-defined terraces. Upper: cartoons of surface crystal structures with Sr ions and TiO_6 octahedra. Lower: AFM images of the sufaces.

(50% vol) and HNO_3 (50% vol) acids mixed at a 3:1 ratio. Deionized water is then added to the mixture at a 4:1 ratio. Etching the soaked substrates with this acid solution at 70^oC in an ultrasonic bath removes the $Sr(OH)\cdot xH_2O$ hydroxide complex by forming dissolved SrCl, leaving the TiO_2 termination on the surface. This step takes about 12 min, after which the substrates are rinsed in deionized water to remove the acidic contamination. Finally, the substrates are cleaned again in acetone and ethanol. Up to this point, one obtains TiO_2-terminated $SrTiO_3$ substrates, but the shapes of the TiO_2-terminated terraces on the surface are irregular because the SrO/TiO_2 terminations are originally randomly distributed. To achieve ordered regular TiO_2-terminated terraces, the surface recrystallization is facilitated by annealing the substrates at 1000^oC in 1 bar ultra pure oxygen atmosphere for 30 min. Figure 2.1 shows an atomic force microscopy (AFM) image of a treated $SrTiO_3$ substrate with atomically flat surfaces (surface roughness $\sim$77 pm) within each terrace. The step height of each terrace is 3.905 $\AA$ corresponding to the lattice parameter of the perovskite cubic unit cell. The terraces are also aligned along the miscut direction with long edges along the perpendicular direction.

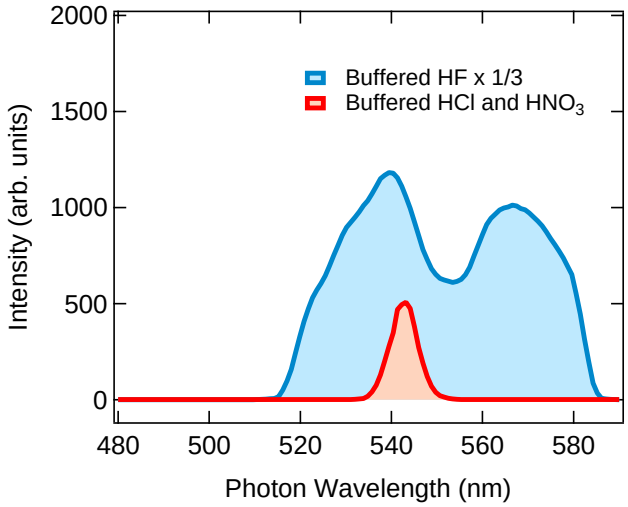

Figure 2.2: Photoluminescence spectra of treated $SrTiO_3$ substrates. For comparison, a spectrum from $SrTiO_3$ substrates treated by the conventional method is included.

With the surface morphology established, we examined the electronic properties and defect states of the treated $SrTiO_3$ substrates by photoluminescence. By using the laser-induced at excitation 370 nm (3.35 eV), defective electronic states inside the band gap (3.2 eV) of $SrTiO_3$ can be detected via the emitted photons from the decay of the excited electrons. Figure 2.2 compares room-temperature photoluminescence spectra in the range of 350-700 nm from $SrTiO_3$ substrates treated with the conventional buffered HF method and our procedure. As shown, the substrate prepared by the conventional route shows a two-peak behavior at 570 nm and 540 nm, while the one treated with our method show only one peak above 540 nm with a significantly smaller intensity. From the integrated intensities of the two spectra, it is clear that our procedure produces much less damage to the substrate.

2.2 Laser Molecular Beam Epitaxy

Laser MBE is a thin film and multilayer deposition method that was recently developed and has been extensively employed, particularly for oxides, in the past several years. Its instrumentation combines two powerful techniques, pulsed laser deposition (PLD) and high-pressure reflection high energy electron diffraction (HP RHEED). While the former carries out the physical process

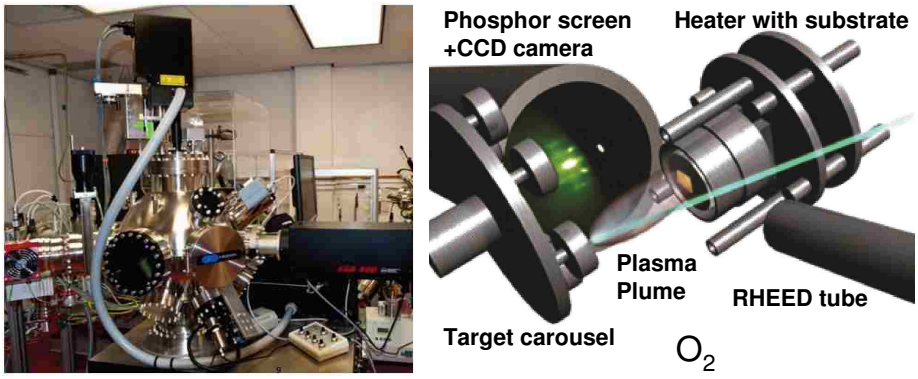

Figure 2.3: Left: a picture of a laser MBE system. Right: schematic inside the deposition chamber.

of the thin film growth, the later allows one to monitor the *in situ* surface quality and coverage in real time, affording feedback for adjusting the growth parameters to achieve control with atomic precision. We will focus on PLD in this section and leave the detailed discussion on RHEED in the next section.

PLD involves ablation of a target with the desired stoichiometry by a high-fluence laser ($1\sim3$ J/cm^2), resulting in a plasma plume consisting of evaporated energetic particles such as atoms, ions and electrons. Since this process typically occurs under (ultra) high vacuum, the plume quickly expands and strongly interacts with a base background pressure varied from 10^{-7} to 10^{-1} Torr before reaching the substrate surface where the adapted species crystalize as a thin film. While the development of PLD can be traced back to the sixties, its widespread in research on oxides did not take place until the discovery of high temperature superconductors in late eighties due to its success in producing high-quality cuprate films. A detailed review on the history, theory and technical development can be found in Ref. [17].

Compared with other deposition methods, PLD has a relatively simple setup because the evaporation of the target material inside the chamber is triggered by an external laser. This advantage also enables convenient target replacement among different materials of interests, which is particularly useful for the growth of different multilayers. In addition, a single laser source can be installed with multiple chambers for different purposes and/or materials by adding a few mirrors in the beam path. The most commonly used laser for oxides is KrF (248 nm) excimer laser due to its

maximized laser-target interaction at the target surface. During this interaction, the mechanism of the energy conversion from the laser pulse into the energetic species in the plume is very complex [17], including multiple steps from ionization, thermal heating to mechanical ejection. However, this highly non-equilibrium process has a rather simple goal that is to remove the target material into the plasma plume with the corresponding stoichiometry. Since the ablation may change the surface stoichiometry, the target is often irradiated by a certain number of pulses before the real deposition to obtain a target surface with a steady chemical composition.

With the plume arriving at the substrate, controlling its interaction with the background gas (mostly oxygen for oxides) around the substrate surface is the key for successful formation of the film with desired morphology. On one hand, while the energetic particles have complicated dynamics within the plasma plume, it is generally believed that collisions with the background gas molecules are necessary to reduce their speeds and thermalize their kinetic energies. This avoids sputtering off the grown film on the substrate or creating defects. On the other hand, the collisions can not be too strong to maintain a high enough temperature of the reacting wavefront of the vapor. Thus, optimization of the degree of thermalization during the flight of the plasma is a critical factor to obtain high-quality films that are fully oxidized and less defective. This is usually achieved via three control parameters, the target-to-substrate distance, the laser fluence and the background gas pressure. While the first one is typically fixed, the latter two can be adjusted synergically.

The ability to vary the background pressure by more than six orders of magnitudes is indeed one of the advantages of PLD. In addition to controlling the propagation of the plume, it is also an important thermodynamic parameter in tuning the stability of the deposited chemical phase, particularly the oxygen content. Due to the pulse nature, the growth dynamics in the ”off” state of the laser is drastically different from that in the ”on” state. As the plume decays, an equilibrium state is rapidly approached where the growth front is governed by the thermodynamic conditions, i.e. the atmosphere pressure and the surface temperature. Subject to these conditions, phases, e.g. metastable phases, that are present under the plume may decompose into phases that are stabler and different in stoichiometry. To obtain the proper phase, a growth phase diagram of pressure

versus temperature is usually established.

2.3 Reflection High Energy Electron Diffraction

RHEED is a grazing incident diffraction method that has been extensively used to characterize the surface structure and quality, particularly in MBE. An overview on the instrumentation, theory and experimentation can be found in Ref. [41]. The availability of well developed electron guns with high brightness facilitates rather simple implementation for *in situ* monitoring. It, however, requires ultra high vacuum environment to operate, which was the major roadblock for the application in PLD for oxides. This difficulty, however, has been overcome recently by using differential pumping.

As a diffraction technique, the scattering geometry with respect to the sample and the momentum of the incident beam determines which part of the reciprocal space is probed. In order to see the small lattice spacing at the level of a few armstrongs by diffraction, the incoming electrons must have a small enough wavelength or a high enough energy which is typically about 20 to 30 keV in RHEED. The glacing incident angle and the relatively small penetration depth of electrons give rise to the extreme surface sensitivity of RHEED, since only the surface atoms participate in the scattering of electrons. Thus, for a flat surface, the incoming electrons can be considered as being diffracted off a two dimensional (2D) lattice plane. The reciprocal space within this 2D plane consists of reciprocal lattice points that have the same transitional and rotational symmetries as in the real space. In the third dimension normal to this 2D plane, these reciprocal lattice points becomes reciprocal rods that extend to infinity, because the real space 2D lattice corresponds to a delta function and the transitional symmetry is absent in this direction. For example, the reciprocal lattice of a square lattice with spacing a is also a square lattice with spacing $2\pi/a$ within the 2D plane, while each reciprocal lattice point becomes a rod perpendicular to the plane (see Fig. 3.1).

In the kinematic approximation where only single elastic scattering events are considered, Bragg's law indicates that the diffraction condition is satisfied when the momentum transferred

to the scattered electron is equal to a reciprocal lattice vector. That is

$$k' - k = G \tag{2.1}$$

where k and k' are the initial and final electron wave vectors, respectively, while G is a reciprocal space vector. Since $|k'| = |k|$, one can construct so-called Ewald's sphere with radius $|k|$ (see Fig. 3.1). Every intersection between the reciprocal rods and Ewald's sphere fulfills the diffraction condition with a corresponding G. Due to the infinite length of the rods, it is easy to see that the (00) rod is always cut by Ewald's sphere, independent on the incident direction. This intersection is called specular reflection because the incident angle is equal to the emergent angle. In other words, the momentum transfer has a zero in-plane component. In an usual geometry of RHEED, the grazing incident beam is along a high-symmetry direction of the surface lattice, such as the $< 10 >$ direction of a 2D square lattice. In this case, all the (0n) rods (n is integer) fall into an effective plane which intersects Ewald's sphere on a circle, so-called the zeroth Laue circle. Thus, all the (0n) rods that intersect this circle must also intersect Ewald's sphere at the same locations and satisfy the diffraction condition. Diffraction caused by (0n) rods other than the (00) rod is usually called off-specular reflection. By a similar agrement, one can show that the intersections between the (-1n) rods and Ewald's sphere also fall onto a ring which is larger and called the first Laue circle. Samples are normally rotatable within the surface plane and one can use different incident directions with their own Laue circles and off-specular reflections.

The diffracted outgoing beams then strike onto a 2D detector which is usually a phosphor screen with a solid angle that is large enough to cover the specular reflection and most other observable reflections. However, since such a detector does not resolve electron energies, it records all elastic and inelastic scattering. In fact, due to the strong interaction between electrons and matters, multiple scattering and dynamic scattering are notably intense and complicated in electron diffraction. These give rise to additional features, such as Kikuchi lines, and modifications to the reflection intensities. Thus, quantitative analysis of RHEED patterns is notoriously challenging.

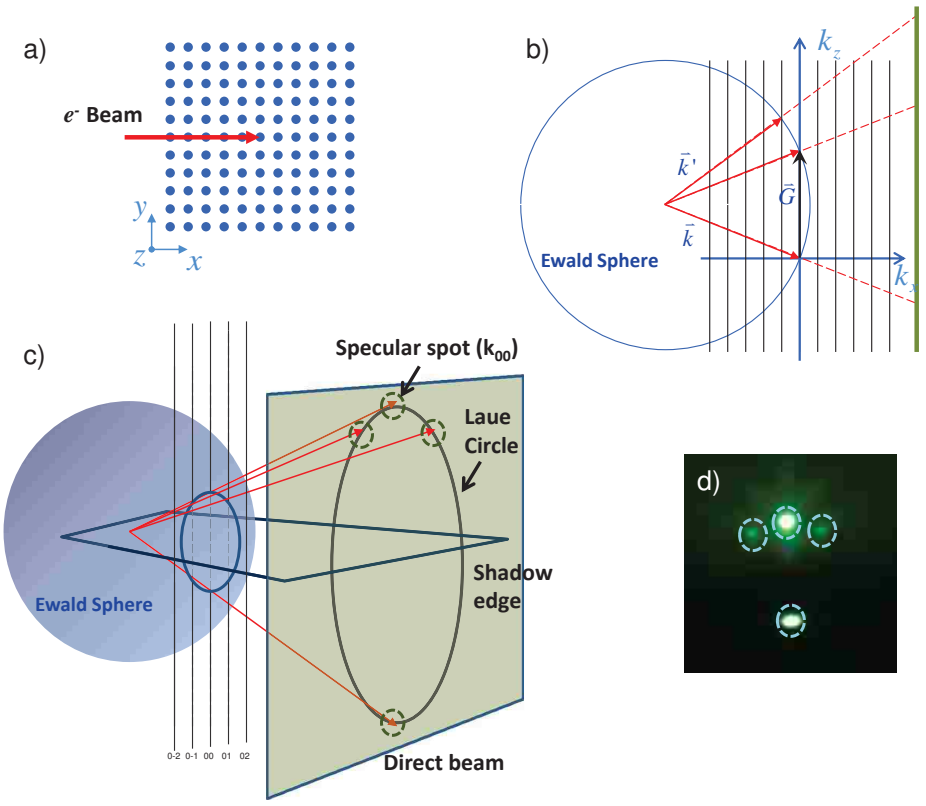

Figure 2.4: (a) the top view of a 2D square lattice. (b) the side view of the reciprocal space with Ewald's sphere indicating reflections that fulfill the diffraction condition. The vertical line on the right denote the detector that intersects the beams. (c) a 3D view of the reciprocal space. (d) a representative RHEED image showing the specular and off-specular reflections and the direct beam.

Nevertheless, qualitative description of the surface crystallinity with some simple modeling often provides fruitful information for monitoring the time-dependent evolution during the growth. For example, when disorder is introduced within a flat surface, the crystalline correlation length is effectively reduced, leading to a finite thickness of the rods in reciprocal space. This increases the intersection areas between the rods and Ewald's sphere along the out-of-plane direction and the original sharp reflection spots on the screen become streaks.

The most extensive use of RHEED is to correlate the time-dependent reflection intensity with the evolving surface roughness or coverage to study the growth dynamics. There are generally three different growth modes [17] (see Fig. 2.5): island growth (Volmer-Weber mode), layer-by-layer (LBL) growth (Frank-Van der Merwe mode), and LBL-to-island growth (Stranski-Krastanov

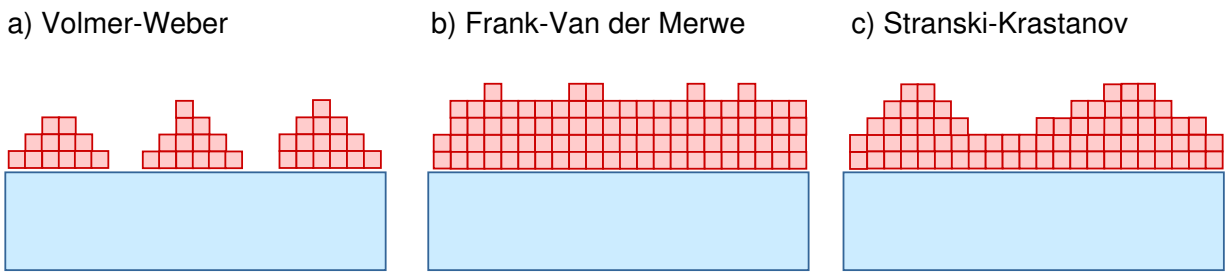

Figure 2.5: Different growth modes: (a) Volmer-Weber mode, (b) Frank-Van der Merwe mode, and (c) Stranski-Krastanov mode.

mode). Island growth occurs via formation of large local 3D clusters which coalesce as the film grows and usually form domain boundaries between them. The surface morphology maintains a constant average surface roughness with ”mountains” and ”basins”. The resulting films often still have oriented crystal structures in the growth direction, but the in-plane coherence with the substrate is lost. In an ideal 2D LBL mode where the growth of the next monolayer does not start until the previous one is complete, the surface roughness is relatively small and exhibits a periodic behavior. That is the surface coverage reaches a maximum (minimum) when the the top layer coverage is at half (complete). LBL mode is characteristic of coherent growth and perfect epitaxy because the interaction/bonding is maximized between the previous layer and the new layer; each atom is maximally coordinated. In the Stranski-Krastanov mode, the growth starts in a LBL fashion and transforms into an island growth regime, which typically occurs when dislocations are formed to relieve the energy imposed by the epitaxial constraint from the substrate. These growth modes can be identified by monitoring the RHEED intensity and pattern. The continuing cycle of LBL growth is reflected on the RHEED intensity oscillation as a function of time, which is illustrated in Fig. 2.6. On the left is an atomically flat surface with some large terraces due to the substrate miscut angle. In this case, the RHEED pattern consists of the bright specular and off-specular reflections, as described earlier. In the middle, one can see that the surface roughness increases during the growth of a monolayer, resulting in decrease in the reflection intensities in the RHEED pattern. When the monolayer is completed as showed on the right, the RHEED intensities and pattern recover, completing the cycle. In the opposite limit, island growth does not involve such

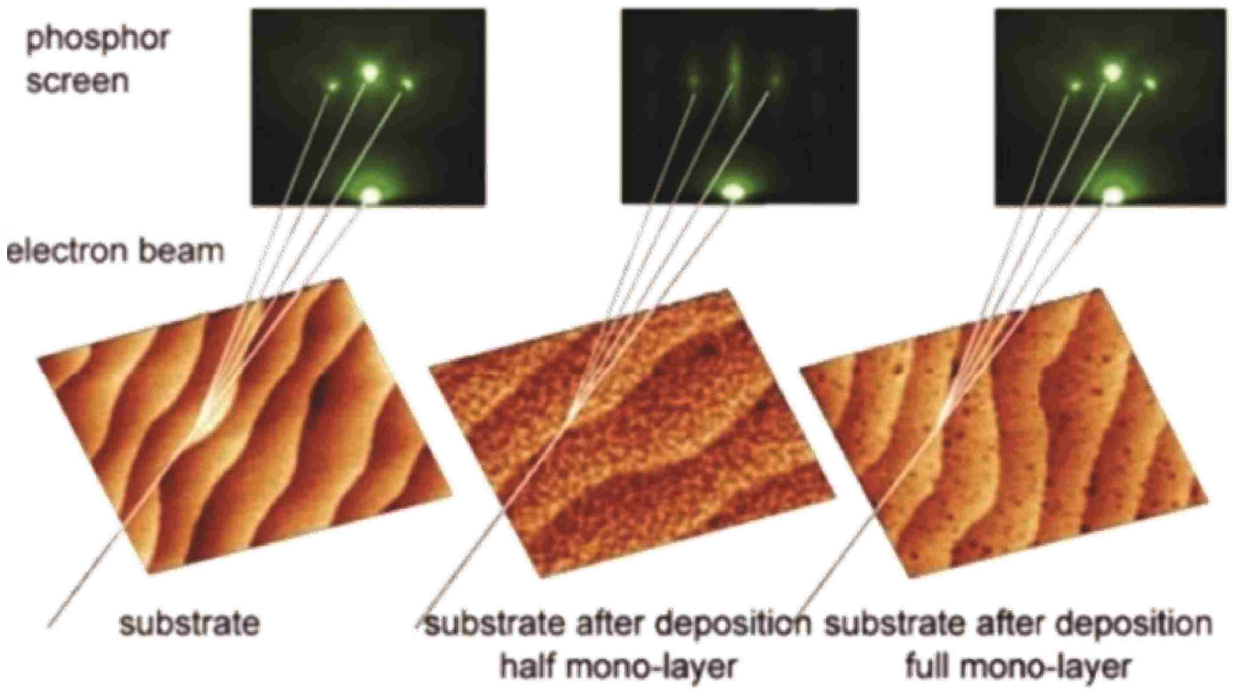

Figure 2.6: RHEED pattern evolution during LBL growth.

a cycling and no RHEED oscillation is observed. In the case of large islands, the surface can no longer be treated as a 2D lattice for interpreting the RHEED pattern which actually reflects the 3D crystal structure within the islands as all the layers contribute to scattering significantly.

In the case of LBL growth, the real situation is often not ideal. For example, the growth of the next monolayer may start before the previous one is completely filled. This may be very energetically favorable when the previous layer has large enough terraces formed and the mobility of the adapted atoms on the top of them is too low to find the terrace step edges to fill the holes. Instead, they start the nucleation of the next monolayer. The corresponding RHEED intensity evolution then has a damping oscillation. This damping behavior may also happen when materials for the next monolayer are already delivered to the surface before the previous layer is completely filled. In other words, the two sequential cycles in the LBL mode are partially overlapped. As a result, the surface roughness can not recover back to the minimum value. This situation may be improved by introducing an interruption between the growth of the two layers as a smoothing period where further recovery of the RHEED intensity is usually observed. A detailed example

will be given in the next chapter.

2.4 Resonant X-ray Spectroscopy and Scattering

2.4.1 Core-Level Spectroscopy

Having described the deposition method, we now turn to the characterization techniques. While the valence electronic structure determines the properties of solids since the valence electrons participate in the chemical bonding between atoms and lose their elementary identity, the inner core electrons of each element remain atomic-like. The unique core-level configurations of each element provide a route to probe the valence electronic states by fingerprinting the contributions from different atomic sites. The related methods typically involve exciting core electrons via striking with energetic particles, such as photons and electrons, are generally classified as core-level spectroscopy [21]. These methods are particularly useful for investigating systems where the valence electronic states are neither completely band-like nor atomic-like due to the spatially confined bonding orbitals of certain elements, including transition metal d-states and rare earth f-states. This relies on the fact that the positively charged core hole left behind by the excitation has a highly localized wavefunction and only interacts with the valence electrons on the same atom. In other words, one sees the local electronic structure by creating an atomic "eye". In addition, when the destination of the excited core electron is one of the atomic levels that are empty or partially empty, this resonance will largely increase the transition possibility and the observed signal. Thus, the advantages of these techniques can be summarized as element-sensitivity, site-selectivity and resonance-enhancement, specially suitable for studying nanostructures.

In core-level spectroscopy, the core levels are denoted as K, L, M and so on, instead of the principle quantum number n =1, 2, 3, and so on. The angular moment is labeled as 1, 2, 3, and so on from high to low energy. For instance, the 1s level is referred as K, and the six $2p$ states are divided into the $2p_{1/2}$ and $2p_{3/2}$ levels by spin-orbit coupling and referred as L_2 and L_3. The binding energy of most core electrons falls into a range from tens of eV to tens of thousands of eV, corresponding to photon energy from soft x-ray to hard x-ray.

2.4.2 X-ray Absorption Spectroscopy

XAS is a powerful core-level spectroscopy for studying electronic structure, particularly for transition metal compounds. In XAS, a core electron is excited to an empty state above the Fermi level by absorbing a photon, creating an excitonic-like final state centered about the core hole. The spectrum is obtained by tuning the x-ray photon energy to reach different empty states. Thus, the intensity or the integrated intensity is proportional to the total number of empty states. Because the excitation does not occurs until the photon energy is high enough for the core electron to reach the Fermi level, the absorption will strongly increase at this threshold energy, which is called the absorption edge. For example, the absorption edges involving the $2p_{1/2}$ and $2p_{3/2}$ core levels are called L_2- and L_3-edge, respectively. The transition probability W from an initial state ψ_i to a final state ψ_f of a system by absorbing a photon is described by Fermi's Golden rule:

$$W \propto |\langle \psi_f | T | \psi_i \rangle|^2 \delta(E_f - E_i - \hbar\omega) \tag{2.2}$$

where (E_f, E_i and $\hbar\omega$) are the energies of the final state, the initial state and the photon energy, respectively. The delta function ensures energy conservation. T is the transition operator that describes the photon-matter interaction, which is given by the electric dipole approximation as

$$T \propto e_q \cdot r \tag{2.3}$$

where e_q is the unit vector of the photon electric field polarization and r is the position. In single electron approximation, ψ_i and ψ_f deduce to the core electron state and an empty band-like free electron state, respectively. The absorption spectrum then maps the unoccupied density of states (DOS) in a band structure (see Fig. 2.7(a)). This is usually a good approximation at O K-edge where a $1s$ core electron is excited to a $2p$ state. The spectrum can then be considered as a $2p$-projected DOS.

However, many-body effects, such as core hole-valence electron interactions and correlation

between valence electrons, may strongly affect the spectrum. This often happens at transition metal L-edges where the excitation corresponds to $\psi_i = 3d^n \rightarrow \psi_f = c3d^{n+1}$ where c denote a $2p_{1/2}$ or $2p_{3/2}$ core hole. As discussed in Chapter 1, depending on the number of electrons and the electron-electron interactions, a partially filled $3d$-shell may have a variety of occupation configurations with different energies. Thus, instead of the single electron picture, the many-body description based on configuration interaction is usually more appropriate to interpret the spectra. For instance, as shown in Fig. 2.7(b), the local ionic configurations are $3d^n$ and $3d^{n+1}\underline{L}$ separated by charge-transfer energy Δ. They are hybridized due to the hopping resonance t_{pd}, forming a bonding state and an antibonding state which are further split depending on the filling configuration within the $3d$-shell. A similar hybridization effect also occurs for the finale states with a core hole and an extra d-electron. While the initial state of XAS is the lowest-energy configuration in the bonding state multiplets, i.e. the ground state (highlighted with a thick bar), different configurations in both bonding and antibonding states can be reached in the final state with different photon energies and probabilities given by Eq. 2.2. By scanning the photon energy across the L_2- and L_3-edges, one effectively samples all the possible configurations with one extra electron added in $3d$-shell, leading to the so-called multiplet structure in the spectrum. With this multiplet structure, one may fingerprint the local electronic structure of the metal ion, such as valence state, spin state, orbital occupation, near-neighbor hybridization, and so on. Despite their different descriptions in the spectral lineshapes at the transition metal L-edge and O K-edge, the integrated intensity is, proportional to the total unoccupied projected DOS, which is called the XAS sum rule.

Another important character of XAS is that one can utilize the polarization of the x-ray and study the anisotropy of the charge, spin and orbital degrees of freedom in the material. The polarization dependence of x-ray absorption is referred as dichroism. When combined with the element-selectivity and resonant enhancement characters of XAS, the dichroic effect can be a very powerful method for investigating nanostructures, as conventional techniques fall. In particular, if circularly polarized lights are used, the effect is called x-ray circular magnetic dichroism (XMCD), which probes the unbalanced spins in the empty states, i.e. the spin polarization or magnetic mo-

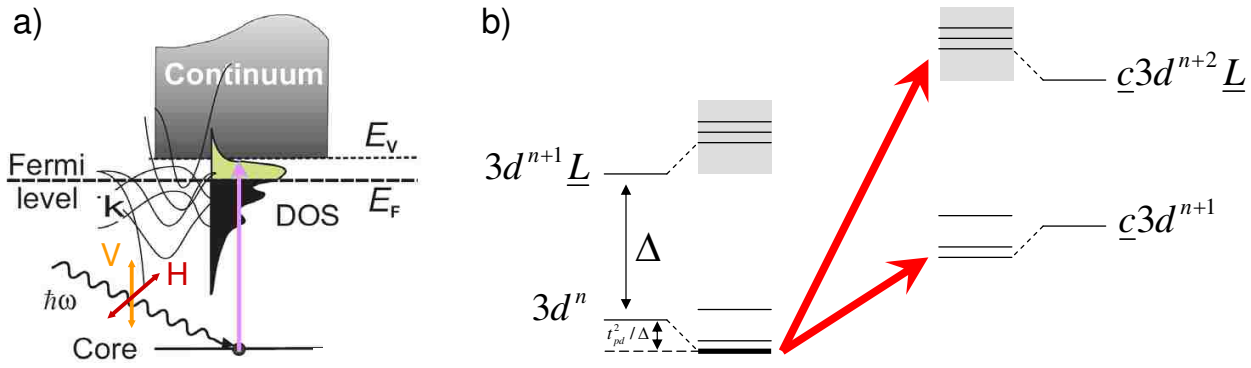

Figure 2.7: Schematics for excitations in XAS. (a) the unoccupied partial density of states is mapped by excitation of core electrons into empty single-electron states above the Fermi level. (b) XAS described in terms of configuration interaction. Red arrows denote the XAS excitations.

ment. The key here is the spin-orbit coupling of the core level which "locks" the spin component and the orbital component with each other for the excited core electron. As a result, the opposite angular moments of the right- and left-circularly polarized photons pick out opposite spins during the transitions. When the valence shell is spin-split, the two polarizations will have different transition probabilities, giving rise to the difference in the absorption intensities. Due to the opposite spin-orbit coupling, this dichroic effect has opposite signs at the L_2- and L_3-edges.

If linearly polarized lights are used, the effect is call x-ray linear dichroism (XLD), which detects the anisotropy in the charge distribution. This anisotropy is due to symmetry breaking that can be caused by local bonding and/or magnetic ordering. As XAS fills the holes in the valence shell with core electrons, rotating the linear polarization of the photon electric field allows one to oscillate the excited core electron in different directions in order to map the anisotropy in the hole density. The bigger the hole density is along a certain direction/axis, the larger the transition probability is with the polarization along the same direction; vice versa. In the case of a d-shell, this anisotropy can be projected onto the hole occupations in the five d-orbitals. As a result, XLD provides an efficient way to directly measure the orbital structure. An prominent example is the superconducting cuprates where the $3d$-shell of Cu has only one hole in the x^2-y^2 orbital (see Fig. 2.8). It is reflected in the drastically different L-edge absorption cross sections between in-plane and out-of-plane polarizations.

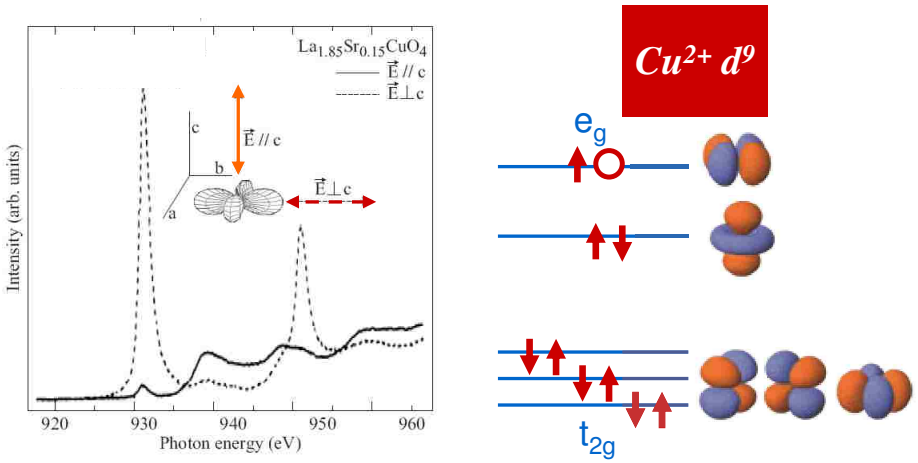

Figure 2.8: Cu L_3-edge spectra of $YBa_2Cu_3O_x$ for in-plane polarizations (E⊥c) and out-of-plane polarization (E‖c) from Ref. [15].

The most straightforward way to obtain absorption is to measure the transmission of x-ray. This method is, however, inapplicable for most materials, particularly in the soft x-ray range ($<$ 1000 eV), due to the relatively short penetration depth. Instead, it is more common to detect the fluorescence or electron escaping originating from the decay of the core hole. While the emitted photons have a similar mean free path to the incident x-ray, the electrons emerging to the sample surface are subject to strong scattering within the sample. Thus, for the same material at the same absorption edge, fluorescence yield has a larger probing depth than electron yield; the former is usually considered to be more bulk-sensitive, while the later is more surface sensitive.

XAS measurements discussed in the following chapters were performed at the 4-ID-C beamline of the Advanced Photon Source at Argonne National Laboratory. This beamline uses a fully electromagnetic undulator as the insertion device in the range from 500 eV to 3000 eV. This device is a circularly polarizing undulator that can provide lights with left or right circular, as well as horizontal- and vertical-linear polarizations. This capability allows one to fix the incident direction or angle with respect to the sample or crystal axes, avoiding geometrical effects during dichroism experiments. For instance, the sample position is kept fixed while linearly polarized light with a 20^o incidence angle is used to probe the e_g holes in the $3z^2 - r^2$ and $x^2 - y^2$ orbital states by rotating the photon electric field parallel ($E \parallel c$) and perpendicular ($E \perp c$) to the out-of-plane direction,

respectively. The beamline has a resolving power of 5000 at 1000 eV, i.e. $\sim$0.1 eV resolution. The endstation for the XAS measurements employs a liquid He flow cryostat that can reach down to 10 K, and a superconducting magnet that can reach up to 7 T. More details on the beamline are described in Ref. [23]. In addition, each spectrum was normalized to the beam intensity monitored by a gold mesh set in front of the samples.

Chapter 3

Heteroepitaxial Synthesis of Perovskite Nickelates

In this chapter, we will discuss the synthesis of $RNiO_3$-based (R = rare earth) ultrathin films and heterostructures via laser molecular beam epitaxy (MBE). Due to the low thermodynamic stability of $RNiO_3$, we will emphasize the mechanism of epitaxial stabilization in thin film deposition. Moreover, to create sharp interfaces, the layer-by-layer (LBL) growth mode is achieved by employing an interrupted method combined with rapid "pumping" during the growth of each unit-cell layer. *Ex situ* characterizations, including atomic force microscopy (AFM) and x-ray diffraction (XRD) will also be discussed. In particular, to demonstrate the application of x-ray absorption spectroscopy (XAS) to heterostructures, we will present the investigation of the effect of polar mismatch on ultrathin $LaNiO_3$/$LaAlO_3$ superlattices (SLs).

3.1 Crystal Growth by Epitaxial Stabilization

Epitaxy generally refers to the growth of a film or a layer with a preferential crystallographic orientation on top of a single crystal substrate. The most important factor in controlling this oriented growth is the crystal plane of the substrate surface which selectively stabilizes a parallel lattice plane of the growing material that has a similar crystal structure or symmetry. As a result, the in-plane positions of the atoms on both sides of this substrate-film interface have one-to-one correspondence. In other words, the in-plane orientation of the film is locked with respect to that of the substrate, while the growth is along the out-of-plane direction. In particular, homoepitaxy refers to the case where the film and the substrate are the same material. Otherwise, it is called heteroepitaxy.

From the energetics point of view, the oriented growth is driven by lowering the formation free energy for the selected direction via forming a coherent interface where mutual bonding is maximized. For instance, in oxide heteroepitaxy, the two oxides often share the perovskite or

perovskite-based crystal structure. In terms of the perovskite pseudocubic unit cell, if the substrate surface is cut along the (001) or (111) plane, the growth of the film will follow the same direction. Choosing different cutting planes allows one to synthesize different hetero-interfaces by design.

Another important consequence of lowering the formation free energy for a selected direction of a specific phase is that one may even synthesize phases that are unstable or nonexistent in the bulk as they become more favorable than other competing phases under epitaxy. This advantage of epitaxial stabilization is particularly important for the thin film deposition of perovskite nickelates. Due to the low thermodynamic stability, the synthesis of $RNiO_3$ requires high temperature and high oxygen pressure ($>$100 bar), and yet yields only micron size single crystalline samples [49]. The lack of sizable single crystals has been a major obstacle for studying the underlying physics. This difficulty can be attributed to the high oxidation state Ni^{III}, while Ni^{II} is most stable. Due to this extreme thermodynamic requirement, any thin film deposition environment, such as oxygen partial pressure less than 1 mbar, is thereby highly unfavorable for the phase formation. As a result, the growth critically relies on the epitaxial stabilization to maintain stoichiometry and avoid decomposition into other stabler phases such as NiO [28]. Any effect that weakens the epitaxial stabilization during the growth, including partial relaxation and 3D island formation, needs be avoided since they immediately causes oxygen deficiency and secondary phases. In fact, relaxation and the induced non-stoichiometry severely hinders the quantitative interpretation of the effect of epitaxial strain on the electronic structure of $RNiO_3$ and is largely responsible for the disagreement among reported results in literature [11]. In order to obtain fully epitaxial stoichiometric nickelate thin films and quantify the role of heterostructuring, perfect epitaxy characteristic of the LBL growth is crucial. In addition, LBL growth is vital in achieving the high morphological quality necessary for hetero-junctions and devices with atomically flat surfaces and interfaces. These challenges highlight the significance of the implementation of *in situ* reflection high energy electron diffraction (RHEED) that monitors the crystal structure of the growth front and the surface quality in real time.

Table 3.1: In-plane pseudocubic lattice constants, a_{sub}, of the used substrates and their corresponding lattice mismatch (ε) with $LaNiO_3$ (3.835 Å) and $NdNiO_3$ (3.803 Å). YAO, SLAO, LAO, SPGO, SLGO, NGO, LSAT, STO, and GSO stand for $YAlO_3$, $SrLaAlO_4$, $LaAlO_3$, $SrPrGaO_4$, $SrLaGaO_4$, $NdGaO_3$, $(La_{0.3}Sr_{0.7})(Al_{0.65}Ta_{0.35})O_3$, $SrTiO_3$, and $GdScO_3$, respectively.

	(YAO)	(SLAO)	(LAO)	(SPGO)	(SLGO)	(NGO)	(LSAT)	(STO)	(GSO)
a_{sub} (Å)	3.692	3.757	3.794	3.812	3.843	3.858	3.868	3.905	3.973
ε_{LNO} (%)	-3.7	-2.0	-1.1	+0.3	+0.3	+0.6	+0.9	+1.8	+3.6
ε_{NNO} (%)	-2.9	-1.2	-0.3	+0.3	+1.1	+1.4	+1.8	+2.7	+4.5

3.2 Epitaxial $RNiO_3$ Ultrathin Films and Heterostructures

We grew (001)-oriented epitaxial ultra-thin layers of $RNiO_3$ (R=La and Nd) as single layer films and SLs with $LaAlO_3$ (LAO) by laser MBE. The lattice mismatch between the substrates and $LaNiO_3$ (LNO) or $NdNiO_3$ (NNO) is listed in Table 3.1. The growth temperature was in the range of 670^o-730^o C. The oxygen partial pressure was maintained at 0.1-0.2 mbar, while the laser fluence was set at $\sim$2 J/cm^2 with the target-to-substrate distance equal to 5 cm. After deposition, in order to achieve the proper oxygen content, samples were post annealed *in-situ* for 30 mins and cooled down to room temperature in one atmosphere of ultra-pure oxygen.

To achieve the perfect epitaxy by LBL growth, the conventional continuous growth method was first used. That is several monolayers were grown continuously as the laser ablates the target at a relatively slow repetition rate, e.g. 3 Hz. A representative evolution of the RHEED specular reflection is shown in Fig. 3.1(a) for the growth of four unit cells (u.c.). As seen, the intensity exhibits four oscillations that are damping rapidly due to the decay of the LBL mode and the presence of unfinished layers. To improve the LBL growth, we then employed the interrupted deposition [7], which requires a fast laser ablation cycle (up to 30Hz) followed by a prolong time-delay between two successive unit cells. For instance, Fig. 3.1(a) shows a typical RHEED specular intensity evolution during the growth of 10 monolayers. Each sharp dip corresponds to the short "laser-on" period of the growth of one monlayer. It is followed by a relatively long "laser-off" delay before the start of the next monolayer. The full recovery of the RHEED specular intensity can be clearly seen, characteristic of the perfect LBL growth. The inset of Fig. 3.1(a) plots the

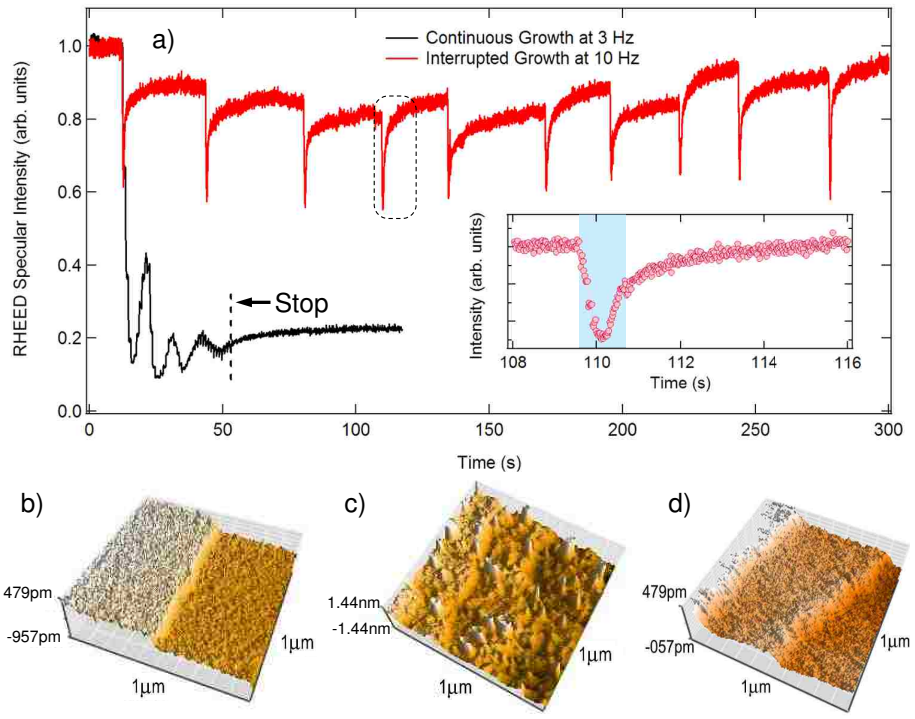

Figure 3.1: (a) A representative RHEED specular intensity evolution during the continuous slow growth and the interrupted growth with fast laser ablation. Inset: the intensity oscillation during the "laser-on" period (highlighted) of the interrupted growth. AFM scans on the surface of a TiO_2-terminated $SrTiO_3$ substrate before the growth (b), after the continuous slow growth (c) and the interrupted growth (d).

detailed evolution during one of these cycles. The "laser-on" period has an oscillation at the end of which the RHEED specular intensity recovers to $\sim$70%. The following "laser-off" period allows the adapted atoms on the top to find and fill the "holes" to complete the growing monolayer and smooth the surface, leading to the full intensity recovery.

This difference of surface morphology between the two growth method was further confirmed by AFM. Figure 3.1(b) shows a typical image of the atomically flat surface of a TiO_2-terminated $SrTiO_3$ (STO) substrate with unit-cell-high (3.9 Å) vicinal steps caused by a finite miscut angle. Figure 3.1(c) shows an image obtained after the continuous slow growth, where small islands of 1-2 u.c. high can be seen. In contrast, a typical image obtained after the interrupted growth with fast ablation displayed in Fig. 3.1(d) indicates that both the atomically flat morphology and the vicinal steps are well preserved. Within each step, the surface roughness is less than 80 pm, the

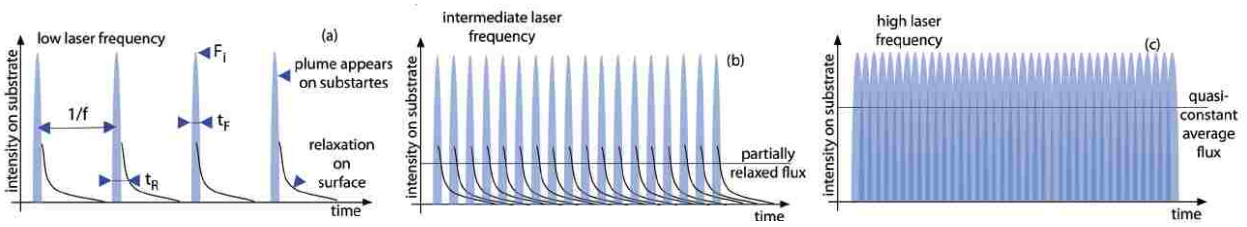

Figure 3.2: Timing diagram showing the modulated flux and relaxation of the island density (adapted from Ref. [44, 19]). During the low-frequency pulsed growth (a), the physical vapor is delivered to the substrate surface where it is relaxed. After increasing the pulse rate (b), the relaxation process becomes more and more delayed. As the frequency (c) reaches the quasi-constant state with average flux, the large degree of supersaturation overcomes the nucleation barrier resulting in the rapid nucleation from the supercritical vapor.

same as the substrate.

To elaborate the role of the laser frequency f during the growth of each unit-cell layer, Fig. 3.2 shows a schematic of the evolution of the growth dynamics. The nucleation and crystallization in pulsed laser deposition (PLD) are primarily governed by two time scales; one is the length of the "flux-on" period t_{F} during which the dense plasma plume typically enforces high supersaturation and nucleation of small islands on the order of one structural unit, while the other is the "relaxation" period t_{R} where the absorbed atoms and small islands reach stabler state by diffusing on the surface to form larger islands or migrate to the edges of larger islands. t_{F} is relatively short on the scale of 10^{-4} to 10^{-3} s [83]. In contrast, t_{R} is about 10^{-2} to 10^{-1} s and much longer [37]. When $t_{\mathrm{R}} \ll 1/f$, the small islands always migrate and reach a steady state before the material is delivered again by the next pulse (see Fig. 3.2(a)). In this case, the LBL growth relies on the condition that the absorbed atoms have enough mobility to find and fill the voids of the incomplete growing layer. Otherwise, the growth will transform into a 3D island fashion due to stacking of several incomplete layers at the growth front. In contrast, when $t_{\mathrm{R}} \sim 1/f$, due to the transitional kinetics imposed by the rapid laser pulsing, the concentration of the small nucleating islands does not fully decay between two consecutive pulses (see Fig. 3.2(b)). In this case, the growing layer is formed by homogeneous coalescence of small islands instead of isolated large islands, reflected in the better recovery of the RHEED specular intensity. If one is able to decrease $1/f$ to the order of t_{F},

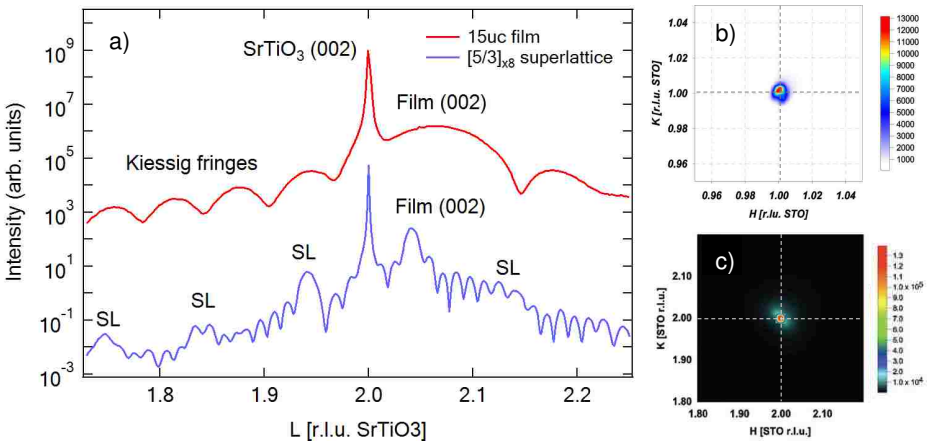

Figure 3.3: (a) representative x-ray diffraction scans around the (003) reflections for a 15-u.c. NNO ultrathin film and a $[(LNO)_5/(LAO)_3]_8$ SL on STO. Reciprocal space maps of the (113) off-specular reflection in the ultrathin film (b) and the SL (c).

the system will see only an average flux of vapor, and the growth will fall into a continuous MBE-like regime (see Fig. 3.2(c)). Finally, since there are fewer and fewer voids as the layer coverage improves, some atoms may remain on the surface. In this case, an interruption on the laser ablation can be introduced to delay the delivery of the next layer so as to wait for the layer completion. This corresponds to the slow recovery of the RHEED specular intensity in the "laser-off" period.

Ex situ XRD was then used to investigate the film structures. Figure 3.3(a) shows the specular $\theta - 2\theta$ scans around the (003) reflection for a 15-u.c. single layer film and a $[(LNO)_5/(LAO)_3]_8$ SL grown on $SrTiO_3$. Total thickness fringes (Kiessig fringes) are clearly seen, indicating coherently grown films. Moreover, their size for the single layer film corresponds to a thicknesses of 15 u.c., which is in excellent agreement with the number of unit cells deduced from RHEED and confirms our LBL control. The film peaks are also seen on the right side of the substrate peak, corroborating the epitaxial perovskite structure and the smaller c-axis lattice parameters of the film than that of the $SrTiO_3$ substrates. Figure 3.3(b) and (c) show the reciprocal space map of the (113) off-specular reflection of both films. We can see that the in-plane components of the reflections are perfectly matched to that of the substrates, revealing the fully strained state.

Finally, to demonstrate the electronic properties of the resulting films, Fig. 3.4 shows the temperature-dependent resistance of a 10 u.c. (<4 nm) LNO film under a tensile strain as large as

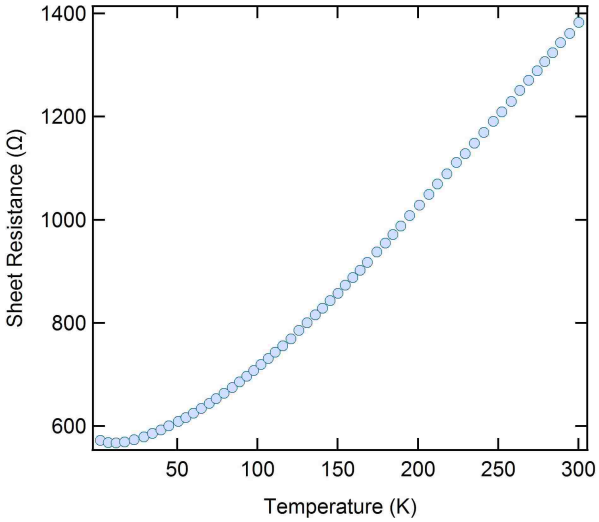

Figure 3.4: Temperature-dependent resistance of a 10-u.c. (<4 nm) LNO ultrathin film grown on $GdScO_3$ substrate which applies a +3.7% lattice mismatch.

+3.7% applied by $GdScO_3$ substrate. Since macroscopic electron transport is subject to scattering from extrinsic localization effects, such as disorder and defects, metallicity is a good measure of the perfection of the underlying lattice and the metallic LNO is a good candidate for this purpose. As seen, the metallic state is well maintained in the ultrathin LNO layer under such a large lattice mismatch. In sharp contrast, reported results in literature showed that, when grown without *in situ* control, the metallicity of LNO films subject to similar or smaller lattice mismatch is already completely suppressed at 5 nm or larger thicknesses, and replaced by a semiconducting behavior [87, 90]. This example corroborates the critical role of perfect epitaxy in controlling the resulting properties, and clearly indicates the improvement on $RNiO_3$ film quality that we have achieved.

3.3 Effect of Polar Mismatch

3.3.1 Introduction

Recently, the problem of polar interfaces has been drawing enormous attention for building interface-controlled devices, since a polar crystal structure grown on a non-polar substrate would be unstable due to the depolarizing fields [70, 67]. An example is showed in Fig. 3.5(a) where two perovskites (e.g. LAO and STO) with different charge structures, such as $A^{3+}B^{3+}O_3^{2-}$ and $A^{2+}B^{4+}O_3^{2-}$, are

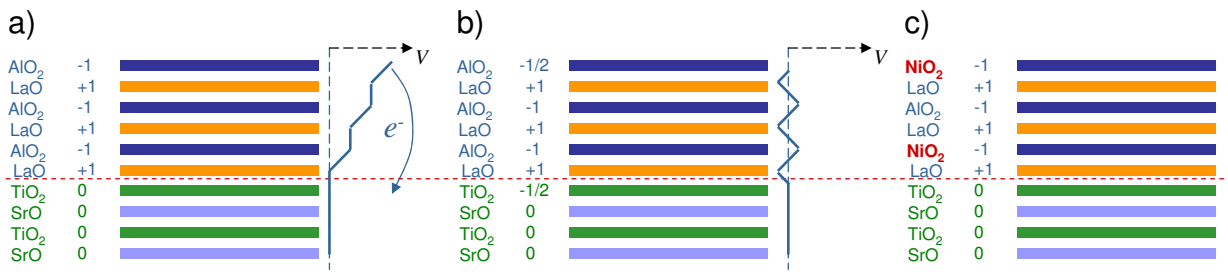

Figure 3.5: Cartoon pictures of polar interfaces of LAO/STO before charge transfer (a), after charge transfer (b), and with some of the LAO layers replaced by LNO in a SL structure (c). V denotes the electron potential.

interfaced together. The +1−-1−+1−-1 alternating stacking sequence on the LAO side would resulting in a diverging electrostatic potential or a diverging electric dipole moment, as the LAO slab becomes thicker and thicker. To avoid this unstable divergence, some mechanism must set in to compensate the potential jump by forcing electronic, structural or chemical (non-stoichiometry) changes. In particular, the active work on this LAO/STO system [35, 40, 65] has suggested an electron transfer to the interfacial TiO_2 that decreases Ti valence by 0.5 at the expense of $0.5e$ charge in the terminating atomic plane (see Fig. 3.5(b)). This mechanism has been intensively discussed to account for the observed 2D electron gas at the LAO/STO interface, although additional effects such as alloying and ionic displacement have been suggested at the interface [64, 77].

A simple fundamental question one can ask is that what if some of the ions at the LAO side are replaced by elements that have multiple valence states. More interestingly, to test the charge-transfer mechanism, we may replace some the LAO layers with LNO (see Fig. 3.5(c)) where Ni is then supposedly converted from 3+ toward 4+ valence state by giving up electrons. In this section, we will show that, instead of Ni^{4+}, an unusual valence state of Ni^{2+} is observed in ultrathin LNO/LAO SLs grown on non-polar (or weakly polar) (001) TiO_2-terminated STO substrates. This is in marked contrast to identical SLs grown on polar LAO, which always exhibit the 3+ valence of the bulk-like LNO. To clarify the origin of these phenomena, we have tracked the changes of the Ni valence as a function of the SL thickness and developed an experimental procedure to monitor and control the electronic state of a transition metal ion.

3.3.2 Results and Discussion

High-quality epitaxial $[(LNO)_1/(LAO)_1]_N$ SLs ($[1/1]_N$ thereafter) with a varying number of repeats N were grown on (001) TiO_2-terminated STO single crystal substrates by laser MBE as described in the previous section. To minimize induced defects, STO substrates were prepared by our chemical wet-etch procedure. A complementary set of SLs were also grown on LAO single crystal substrates. To identify the valence state of Ni, we performed XAS on the Ni $L_{3,2}$-edge. By using XAS, the Ni valence state can be directly and nondestructively fingerprinted for samples as thin as a single unit cell. By utilizing this exquisite sensitivity to the Ni charge state, we were able to detect and trace the effects of charge transfer, local symmetry and non-stoichiometry across the layers. Due to the overlapping La M_4-edge, the spectrum at the Ni L_3-edge is strongly distorted which is the reason for focusing on the Ni L_2-edge. Fig. 3.6 shows the Ni L_2 spectra measured in the bulk sensitive fluorescence-yield mode for the $[1/1]_N$ SLs with different growth sequences. Spectra from bulk LNO and NiO ceramic are also included as Ni^{3+} and Ni^{2+} references, respectively. By direct comparison of the absorption spectra in Fig. 3.6, the sharp difference between the Ni charge state in the $[1/1]_N$ SLs and the bulk-like Ni^{3+} spectra can be seen.

A few important observations are due. Firstly, the $[1/1]_3$ sample with LNO grown directly on the STO surface clearly exhibits a characteristic doublet with a $0.3eV$ shift to lower energy, which matches the Ni^{2+} XAS spectra of the NiO standard at the L_2 edge. This implies that the initial growth results in a phase analogous to heavily oxygen deficient bulk $LaNiO_{3-x}$ [84], such as $LaNiO_{2.5}$ with a Ni valence of 2+. As N is further increased, the Ni valence for the SLs on STO moves progressively towards Ni^{3+} as noted by the difference between the 6-repeat and 20-repeat samples. Although the spectra only give the average over the entire SL, the Ni^{2+} states in the initial layers must be shifted to account for the progression to 3+ as the latter layers are grown; the 6-repeat sample is more 3+ like than the average of 3-repeat and 20-repeat samples. This result implies that growing the polar SLs on a non-polar or weakly-polar substrate such as STO results in a significant chemical compensation and electronic reconstruction during the initial growth. In contrast, the XAS spectra for the same set of SLs grown on LAO show that Ni valence is very close

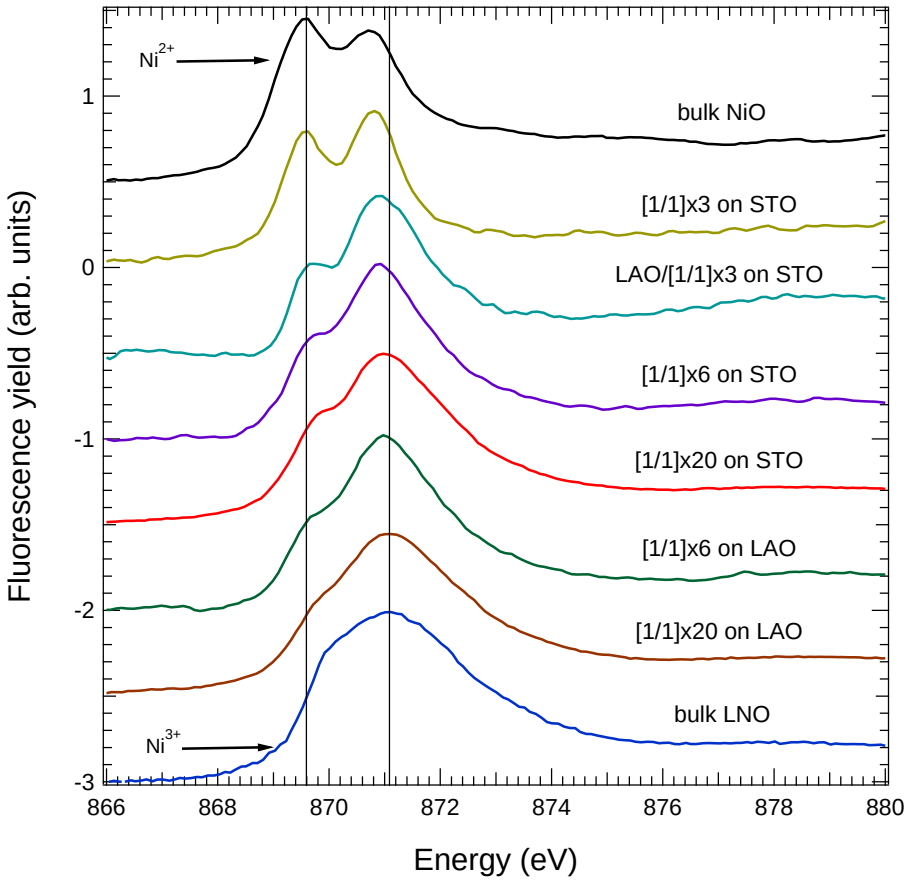

Figure 3.6: X-ray absorption spectra at the Ni L_2-edge of the $[1/1]_N$ SLs grown on STO and LAO. The top black curve represents the Ni^{2+} standard from NiO.

to 3+ as directly evident from XAS on the SLs with N=6 and 20. To exclude the compensating charge transfer between Ti of STO and Ni of LNO, we compared the Ti L-edge spectrum near the SL-substrate interface from the electron yield mode to the Ti spectrum taken on a bare STO substrate (see Fig. 3.7). The measurement unambiguously confirms that no significant change of Ti^{4+} valence takes place near the film-substrate interface, likely due to the high oxygen pressure during the deposition. Next we investigated a possibility to preserve the fragile electronic state of Ni^{3+} ions by fabricating a series of SLs on a 2 u.c. LAO buffer layer deposited on STO. It is clear from the data for the N=3 SL with a LAO buffer shown in Fig. 3.6 that the buffer greatly aids in restoring the electronic state of Ni towards 3+.

Conductivity of bulk LNO has been shown to be sensitive to oxygen deficiency which tightly correlates with Ni valence [84]. To clarify if Ni 2+ valence is connected to oxygen deficiency,

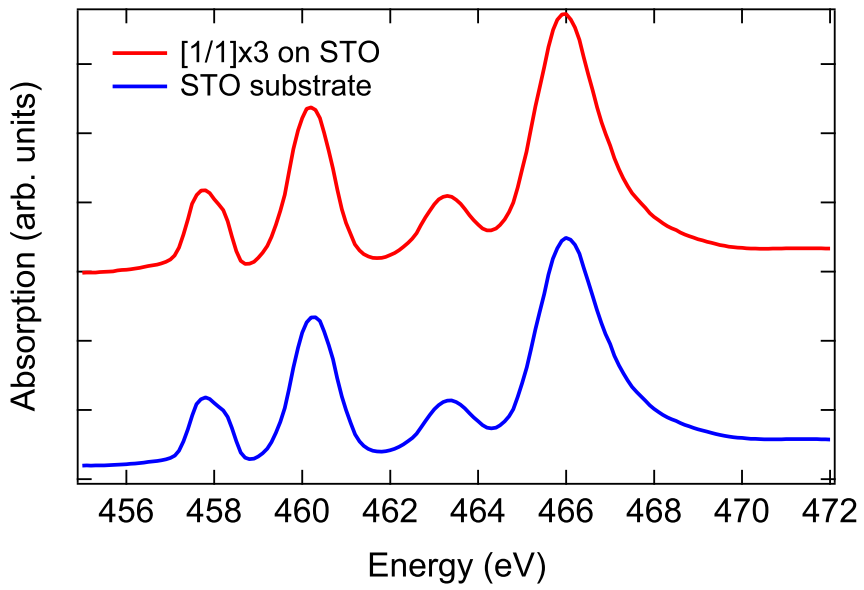

Figure 3.7: X-ray absorption spectra at the Ti *L*-edge of a bare STO substrate (blue) and the $[1/1]_3$ SLs (red) grown on STO.

we annealed the SLs at 900^{o}C in flowing ultra-pure O_2 at 1 bar for 12 hours. Subsequent reduction in N_2 followed by re-oxidation in O_2 was also carried out under the same conditions. DC resistivity measurements were performed after each step using the *van der Pauw* geometry. This experiment revealed that prolonged annealing in O_2 of the as-grown samples has no sizable effect on the resistivity. In contrast, the reduction in nitrogen had strongly increased the resistivity of the samples by several orders of magnitude, while the subsequent re-oxidation restored it back to the as-grown level, indicating that the Ni 2+ valence is not related to simple oxygen deficiency. This experiment provides strong evidence that the observed deviation of Ni valency from 3+ is not due to insufficient oxidation during the deposition but is likely related to the formation of acceptor-like complex defects caused by the polar discontinuity.

Fundamentally, the phase of a material deposited on the surface is determined by enthalpy H. While H is controlled by the environmental thermodynamic parameters (e.g. pressure and temperature), it also intimately depends on the atomic interactions on the surface (i.e. wettability). Thus, the electrostatic interactions within a structure consisting of oppositely charged alternating atomic planes will result in a large increase to H due to polarity mismatch [65], and render

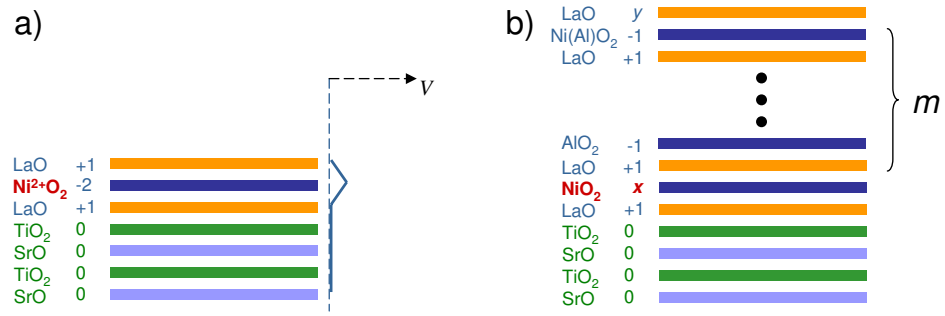

Figure 3.8: The model tri-layer structure consisting of three atomic planes (charge densities on the right) resulted from the excess LaO growth at the initial stage of deposition on STO.

the structure unstable. Experimentally, the probability to grow such a structure from the vapor phase is negligibly small. Instead, it has been proposed that such a polarity mismatch can be generally resolved by transferring $0.5e$/layer from the surface to the polar-nonpolar interface[70, 35]. However, the experimental observation of the large amount of Ni^{2+} present in the ultra-thin SLs contradicts this model. As an alternative, with the presence of Ni^{2+}, intriguing polar compensation by the excess growth of an additional LaO plane can be proposed. As illustrated in Fig. 3.8, at the initial stage of growth, the polarity mismatch could result in a tri-layer structure like .../$Ti^{4+}O_2^{4-}$/$La^{3+}O^{2-}$/$Ni^{2+}O_2^{4-}$/$La^{3+}O^{2-}$, which contains a perovskite unit cell plus an extra LaO plane and notably possesses no total charge or dipole moment. Consequently, Ni is promoted to the 2+ charge state by the strong decrease of the electron potential due to the two LaO planes.

As the growth continues, the later deposited m ($m = 0, 1, 2, ...$) layers of LaO/Al(Ni)O_2 must be accommodated by adjusting the plane charge densities (the charge per u.c. in units of $|e|$) of the bottom NiO_2 plane, x and the surface plane, y. To see their evolution with m, one can derive them simply based on charge neutrality and dipole compensation, assuming all ions of the interlayers maintain their formal valences. If the excess LaO plane remains on the surface, they are given by

$$1 + x + y = 0 \tag{3.1}$$

and

$$[(1 + x) + 2(1 + m)y] - (m + 1) = 0 \tag{3.2}$$

with the distance between the LaO plane and the Al(Ni)O_2 plane, i.e. half unit cell, set to 1. Equation 3.1 ensures the charge conservation between the first unit cell and the surface plane. In Eq. 3.2, the first part takes into account the dipole moments due to deviation from formal charge densities, i.e. the compensating dipole moments, while the second part represents the dipole moment of an uncompensated $m+1$ unit-cell layers. One can then easily obtain x and y as

$$x = -(3m+2)/(2m+1) \tag{3.3}$$

and

$$y = (m+1)/(2m+1) \tag{3.4}$$

in terms of m. The Ni valence in the bottom NiO_2 plane therefore becomes $3-y = 3-(m+1)/(2m+1)$. Note, setting m to zero will correspond to the initial tri-layer structure. On the other hand, one can see that, when $m \to \infty$, the charge density of the bottom NiO_2 plane changes from -2 to -1.5, corresponding to the asymptotical evolution of the Ni valence from 2+ to 2.5+. Although this model is based on simple assumptions, it provides qualitative explanation to the observed progressive recovery of Ni^{3+} at small N without introducing complex factors, such as defects or disorder. In reality, a more gradual vertical distribution of the Ni valence within the whole SL may be expected for these charges that stems from the gradient contribution to H. The corresponding charge distribution function should minimize H at each given thickness. Defects or disorder may also present as competing routes to compensate the polarity mismatch and introduce Ni^{2+} valence state. Nevertheless, our observations demonstrate that the problem of polar mismatch occurs during the growth and can be solved instantaneously by chemically forming metastable structures, instead of transferring electrons after growing the ”ideal” structure.

Chapter 4

Effects of Heteroepitaxial Strain

Heteroepitaxial strain is one of the most important and most extensively utilized control parameters in epitaxy engineering. It is also an inevitable effect because lattice mismatch always exist between two different materials. As directly acting on the lattice of a thin layer of material by interfacial bonding, epitaxial strain is often more efficient than elastic mechanical stress and the resulting property modifications can be dramatic. Therefore, to rationally design a heterostructure, the lattice mismatch is an essential starting point. In this chapter, we will discuss how the bi-axial character of heteroepitaxial strain affects the orbital degree of freedom of d-electrons in $LaNiO_3$ (LNO) ultrathin films, since orbital-lattice interaction, e.g. the crystal field effect and the JT effect, is critical to the local electronic configuration and related long-range orderings as described in Chapter 1. The second part will go further to show the control of heteroepitaxial strain on the $p-d$ covalency via modulating both the self-doping and hybridization. As a result, the metal-insulator (MI) transition and the collective charge- and spin-ordered ground state of $NdNiO_3$ (NNO) ultrathin films can be fine tuned within a larger phase space.

4.1 Orbital Response to Lattice Mismatch

4.1.1 Introduction

Heteroepitaxy is a powerful venue to modify orbital-lattice interactions in correlated materials with strong electron-electron interactions derived from transition metals with open d-shell configurations [39, 53, 93]. However, efforts to rationally control properties that are exceedingly sensitive to small perturbations [20] through the strong orbital-lattice coupling are impeded by a poor understanding of how the epitaxial interfaces impose constraints on the orbital response [98]. Thus, despite the recent progress in strain-induced orbital engineering, a crucial fundamental

question remains: when a single electron occupies a doubly degenerate manifold of d-orbital in an octahedral crystal field, such as in perovskites with Cu^{2+}, Mn^{3+} or low-spin Ni^{3+} cations, how do the interface-imposed epitaxial constraints select the correlated orbital response and electronic configurations?

The exceptional strain-control of the frontier atomic orbitals relies on the susceptibility of the orbital occupations and their energy splitting to bi-axial strain-induced lattice deformations. For this reason, the conventional orbital engineering approach in perovskite oxides is often rationalized as follows: heteroepitaxial strain imposes a tetragonal distortion on the film's primitive unit cell, which results in a modification of the M-O bond lengths of the MO_6 octahedral units. The bond distortions in turn reduced the crystal field symmetry and remove the two-fold e_g orbital degeneracy. Since the $x^2 - y^2$ and $3z^2 - r^2$ orbitals represent in-plane and out-of-plane electron densities, respectively, it is generally anticipated that tensile and compressive strains should symmetrically split their energy levels but with opposite signs. The bands derived from these two orbitals are either lowered or raised relative to their strain-free band center of mass, leading to an orbital polarization with a finite filling. This symmetric strain-induced orbital polarization (SIOP) concept is routinely used to rationalize the orbital responses of many complex oxide systems [98, 1], and also plays a key role in several recent theoretical proposals for replicating high-T_c cuprate physics in perovskite nickelate heterostructures [14, 34] described in Chapter 1. However, the strategy for tuning the correlated ground states in ultra thin films devised from this SIOP concept is violated more often than it applies: for instance, doped manganite thin films exhibit $3z^2 - r^2$ orbital polarization plainly inconsistent with the SIOP model [47, 96] regardless of whether the applied bi-axial strain is tensile or compressive. Ultra thin cuprate bilayers also show variable critical temperatures depending on the layering sequence [29] correlated with the sign of the interface lattice misfit, and a ferromagnetic order can be switched on (or off) depending on the strain state in otherwise diamagnetic cobaltite films [24]. In this section, we will provide insight into the violation of the SIOP model via our investigation on the orbital-lattice interactions in 10-u.c. thick films of orbitally degenerate (e_g^1) LNO.

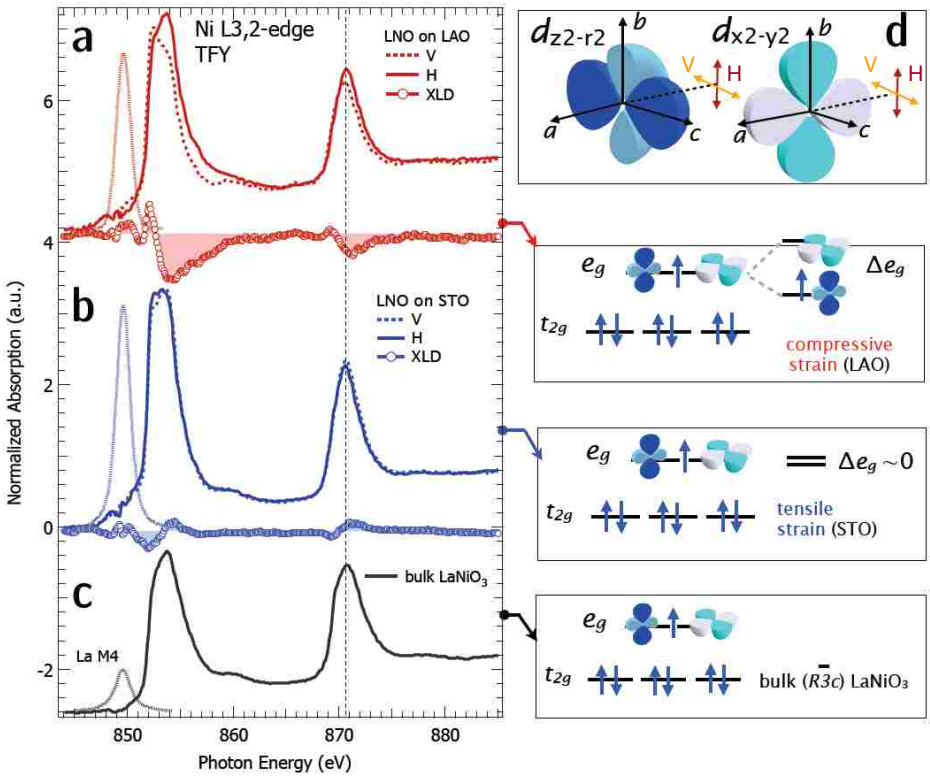

Figure 4.1: Normalized absorption spectra at the Ni *L*-edge taken in the bulk-sensitive fluorescence mode with varying photon polarization (see legend) for films under compressive (red) (a) and tensile (blue) (B) strain, on LAO and STO substrates, respectively. The black curves in (c) represent the bulk (ceramic) LNO data. (RIGHT) Schematic orbital level diagram for bulk LNO and the anticipated strain-induced orbital polarization effect on the e_g doublet.

4.1.2 Results and Discussion

Here we focus on the evolution of the orbital polarization under two representative strain states: compressive and tensile strain on $LaAlO_3$ (LAO) and $SrTiO_3$ (STO) substrates respectively. We synthesized high-quality (001)-oriented 10 unit-cell (u.c.) epitaxial LNO films by laser molecular beam epitaxy (MBE) as described in Chapter 2. Single crystal LAO and STO were used to apply opposite bi-axial strain states; lattice mismatch is -1.1% on LAO and $+1.8\%$ on STO. To probe the response of the Ni $3d$ orbital occupations, we employed x-ray absorption spectroscopy (XAS) with linearly polarized lights, i.e. x-ray linear dichroism (XLD), at the Ni *L*-edge. Figure 4.1 shows the normalized absorption spectra taken by the fluorescence yield mode at room temperature for in-plane (H=$E \perp c$) and out-of-plane (V=$E \parallel c$) polarizations under the two opposite strain states.

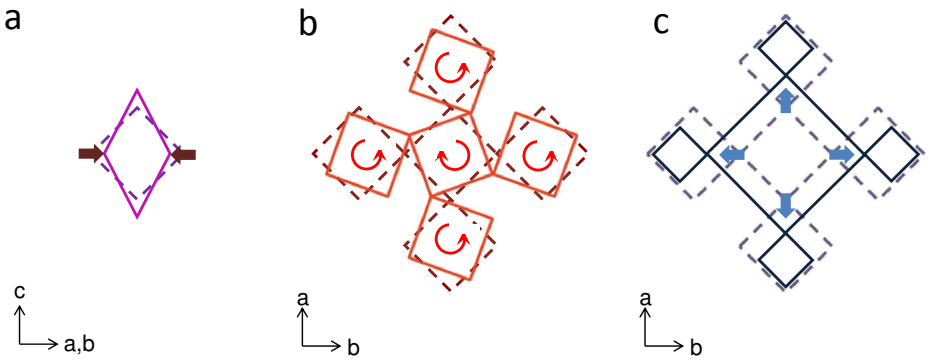

Figure 4.2: Different types of distortions for accommodating lattice mismatch. Dashed diamonds stand for undistorted octahedral network, while the solid ones represent the distorted network. Arrows denote the distortion motions. a) compressed octahedron in accordance with SIOP. b) cooperative octahedral rotation. c) breathing mode.

As seen, each polarization averaged spectra is representative of octahedrally coordinated Ni^{3+} and in good agreement with the spectrum taken on bulk LNO (see Fig. 4.1(c)). There are distinct differences, however, in the polarization dependence between films under compressive and tensile strain. Specifically, as showed in Fig. 4.1(a), the absorption for the out-of-plane polarization is shifted by $\sim$100 meV lower in energy than the in-plane polarization for LNO under compressive strain on LAO. This dichroism indicates a small e_g band splitting between the Ni-derived $x^2 - y^2$ and $3z^2 - r^2$ orbitals (see Fig. 4.1, right) due to the distortion of the spherical charge distribution around the Ni sites by non-uniform Ni-O bond lengths. The sign of the XLD implies that the in-plane Ni-O bonds are moderately compressed relative to the out-of-plane apical Ni-O bonds along the c-axis in agreement with the model of SIOP concept (see Fig. 4.2(a)).

For tensile strain with the same substrate-film orientation, the SIOP model predicts an inversion of the orbital polarization and the population of the $d_{x^2-y^2}$ orbital; however, the polarization dependence of our films on STO is remarkably different. As shown in Fig. 4.1(b), the orbital dichroism is practically absent. This result implies that the uniform Ni-O bond lengths and the highly symmetric crystal field remain seemingly intact despite the large ($\sim +2\%$) tensile strain.

These findings are surprising since, according to the SIOP framework, the larger magnitude of the strain from STO than LAO should also produce a large orbital polarization albeit with an opposite sign. The violation of the SIOP model under the tensile strain demonstrates an asymmet-

rical orbital response to the bi-axial epitaxial strain, and is indicative of other efficient competing mechanisms in accommodating the lattice mismatch. One possibility is the octahedral rotation which can modulate the pseudocubic lattice parameter by changing the Ni-O-Ni bond angle instead of the Ni-O bond length (see Fig. 4.2(b)) [54]. Density functional calculations within the local-spin density approximation (LSDA) plus Hubbard U method were also computed based on our experimentally determined lattice parameters. The resulting structural optimizations are indeed consistent with our findings by XLD. While the structure on LAO consists of a single Ni site with different in-plane and out-of-plane Ni-O bond lengths that lift the formerly bulk-like cubic Ni-site symmetry and the orbital degeneracy, it shows a pronounced pattern of octahedral rotations on STO. Moreover, the tensile strain also stabilize an additional intriguing breathing mode imposed on the NiO_6 octahedral network to accommodate the lattice mismatch (see Fig. 4.2(c)). This 'breathing' octahedral distortion induces a Ni-O bond length disproportionation by splitting the equivalent Ni sites into Ni(1) and Ni(2) that are located at the center of nearly ideal NiO_6 octahedra with different average Ni-O bonds lengths of 2.00 Å and 1.93 Å, respectively.

4.2 Modulating Covalency and Metal-Insulator Transition

4.2.1 Introduction

From the previous section, we can see that the asymmetrical orbital response to heteroepitaxial strain results in a zero net orbital polarization even under a large tensile strain. The lattice mismatch can be largely absorbed by stabilizing a breathing-type distortion via bond disproportionation. Interestingly, an analogous tendency to bond disproportionation is found in the low temperature insulating monoclinic phases of all nickelates with small rare earth and associated with the charge ordering (CO) via charge disproportionation of the formal ionic type $2\mathrm{Ni}^{III} \longrightarrow \mathrm{Ni}^{II} + \mathrm{Ni}^{IV}$ [11, 25]. While the Ni^{II} site corresponds to the d^8 configuration, the Ni^{IV} site consists of the $d^7\underline{L}$ and $d^8\underline{L}^2$ configurations rather than the energetic d^6 state. This is due to the fact that, as a charge-transfer-type Mott system with a small charge-transfer energy Δ, charges fluctuate through $d^7 \longleftrightarrow d^8\underline{L}$ in the metallic state. In the limit of the negative charge-transfer energy regime where the

$d^8\underline{L}$ configuration is dominant, the orbital degeneracy would be effectively removed with the extra electron in the d-shell. In addition, the presence of ligand holes indicates the covalency between Ni and O may play a critical role in the electronic properties.

In correlated systems such as $RNiO_3$, covalency controlled by Δ and the hoping integral t is highly nontrivial because it involves hybridizing electronic states of distinct characters. Specifically, while correlation is derived from the spatially confined d orbitals where the quantum states preserve the atomic characters described by Hund's rule, it is translated into solid state properties by intermixing with the extended continuum states of O $2p$ orbitals. This intermixing drives the localized-itinerant transition, in proximity to which diverse competing ground states may emerge [42], spanning from exotic magnetism to unconventional superconductivity. In this section, we will demonstrate that by taking advantage of interfacial constraint in ultrathin films combined with resonant x-ray spectroscopy we are able to modulate and monitor the covalency in $RNiO_3$ and ultimately the collective phase behavior of Mott materials.

4.2.2 Results and Discussion

Self-Doping

To evaluate the degree of strain-modulated covalency as a practical design parameter, we use resonant XAS measurements at the oxygen K-edge in the electron yield mode to isolate the change in the ligand hole density of the $d^8\underline{L}$ component of the Ni^{3+} ground state. A series of single crystal substrates from $LaAlO_3$ (LAO, lattice mismatch of -1.1%), $SrLaGaO_4$ (SLGO, +0.3%), $SrTiO_3$ (STO, +1.8%), to $GdScO_3$ (GSO, +3.6%) were used to systematically vary the strain applied on LNO. The part of the oxygen spectrum around 528.5 eV shown in Fig. 4.3(a) is often called the pre-peak and corresponds to the transition from core-level O $1s$ states into the unoccupied and strongly Ni $3d$-hybridized O $2p$ states right above the absorption edge, i.e. $3d^8\underline{L} \longrightarrow 3d^8\underline{1s}$. Peaks at higher energies (not shown) are associated with O-hybridized La ($5d, 4f$) and Ni $4s$ states and consistent with the reported bulk results [57]. As discussed in Chapter 2, because of the weak interaction between the O $1s$ core hole and the band-like extended O $2p$ states, the O K-edge spec-

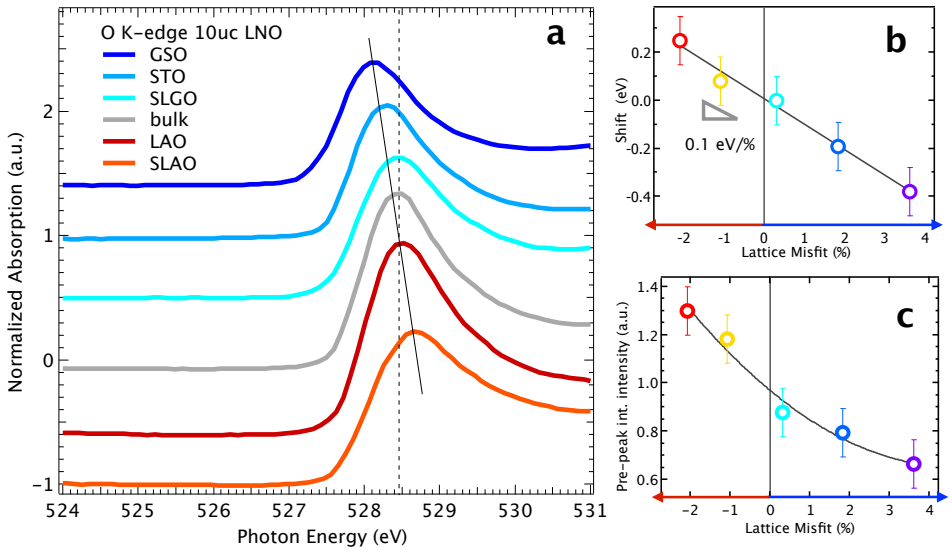

Figure 4.3: Bi-axial strain-induced covalency changes in LNO ultrathin films. (a) low-energy O K-edge pre-peak absorption around 528.5 eV for compressive (red) and a range of tensile (shades of blue) strain states. The higher-energy peaks above 530 eV correspond to the transition into La $5d4f$ and Ni $4s4p$ states and are not showed for clarity. Energy shift (b) and the normalized FWHM (c) relative to the bulk LNO energy position with respect to lattice misfit.

trum can be well approximated as the $2p$-projected partial density of states (DOS) above the Fermi level. Thus, the energy and the width of the observed pre-peak provides a direct measure of the position and the bandwidth of this hybridized conduction band, respectively, and hence the degree of Ni-O bonding.

Unlike the Ni L-edge which is well aligned to the bulk LNO value, the oxygen pre-peak reveals a remarkably systematic and nearly linear dependence of the peak position with strain: as seen in Fig. 4.3(b) it shifts at a rate of almost 100 meV per percentage of lattice mismatch. We recap that the position of this pre-peak is measured with respect to the $1s$ core-level and directly coupled to the Madelung energy. Thus, the shift reflects modification of the charge-transfer energy imposed by the hetero-interface. Additionally, as seen in Fig. 4.3(c), there is a corresponding systematic change in the full-width at half-maximum (FWHM) which implies a strong narrowing of $3d$ electron bandwidth due to the reducing Ni-O-Ni resonant hopping integral with increasing tensile strain. These experimental findings demonstrate the control of the strain-modulated ligand hole density.

It is interesting to conjecture that by reversibly accessing these interactions and by controlling

Table 4.1: In-plane pseudocubic lattice constants, a_{sub}, of the used substrates and their corresponding lattice mismatch (ε) with $NdNiO_3$ (3.803 Å). YAO, SLAO, LAO, SPGO, SLGO, NGO, LSAT, STO, and DSO stand for $YAlO_3$, $SrLaAlO_4$, $LaAlO_3$, $SrPrGaO_4$, $SrLaGaO_4$, $NdGaO_3$, $(La_{0.3}Sr_{0.7})(Al_{0.65}Ta_{0.35})O_3$, $SrTiO_3$, and $DyScO_3$, respectively.

	(YAO)	(SLAO)	(LAO)	(SPGO)	(SLGO)	(NGO)	(LSAT)	(STO)	(DSO)
a_{sub} (Å)	3.692	3.757	3.794	3.812	3.843	3.858	3.868	3.905	3.955
ε (%)	-2.9	-1.2	-0.3	+0.3	+1.1	+1.4	+1.8	+2.7	+4.0

the relative weight of charge-transfer energy Δ *vs*. *d*-electron bandwidth *W* one should be able to activate latent MI phase transitions in other correlated electron systems. To this end, we synthesized a series of fully strained $NdNiO_3$ (NNO) ultrathin films (15 u.c. $\sim$ 5.7 nm) subject to varied lattice mismatch from -2.9% to $+4\%$ (see Table 4.1), and performed the same XAS measurement at the O *K*-edge. For direct comparison, we also measured the bulk ceramics of $RNiO_3$ (R = La, Nd, Gd) across the bulk MI transition boundary.

Figure 4.4(a) shows the *K*-edge spectra at the threshold energy around 528.5 eV where the absorption pre-peak is due to Ni 3*d* states hybridized with O 2*p* states. For the bulk samples (black lines), it is found that reducing the R^{3+} ionic radius from La(1.36 Å) to Nd(1.30 Å) and then to Gd(1.08 Å) decreases the FWHM by $\sim$106 meV and $\sim$180 meV respectively. This declining bandwidth is consistent with the bulk phase behavior and the MI transition. A seemingly resemblant narrowing of the pre-peak is also observed for the heteroepitaxial NNO whose FWHM clearly scales with lattice mismatch as showed in Fig. 4.4(b); a linear fit to the full lattice mismatch range yields the value of 43(6) meV per percent of lattice mismatch. In addition to the evolving FWHM, the pre-peak also exhibits a remarkably systematic energy shift as a function of heteroepitaxial strain, as seen in Fig. 4.4(b), indicative of variations in the excitation energy. Fig. 4.4(b) illustrates the evolution of the energy shift plotted against strain. As can be seen, the pre-peak energy shifts asymmetrically - downwards by as large as 270 meV at +4% (or $\sim$80(13) meV/%) and upwards by $\sim$150 meV at -2.9% (or $\sim$34(13) meV/%). In sharp contrast, the shift is completely absent in the bulk data when varying chemical pressure and/or temperature. These results corroborate that the decrease in Madelung energy and consequently the charge-transfer energy with strain varying from the compressive to tensile side, or vice versa. The narrowing of the conduction bandwidth from the

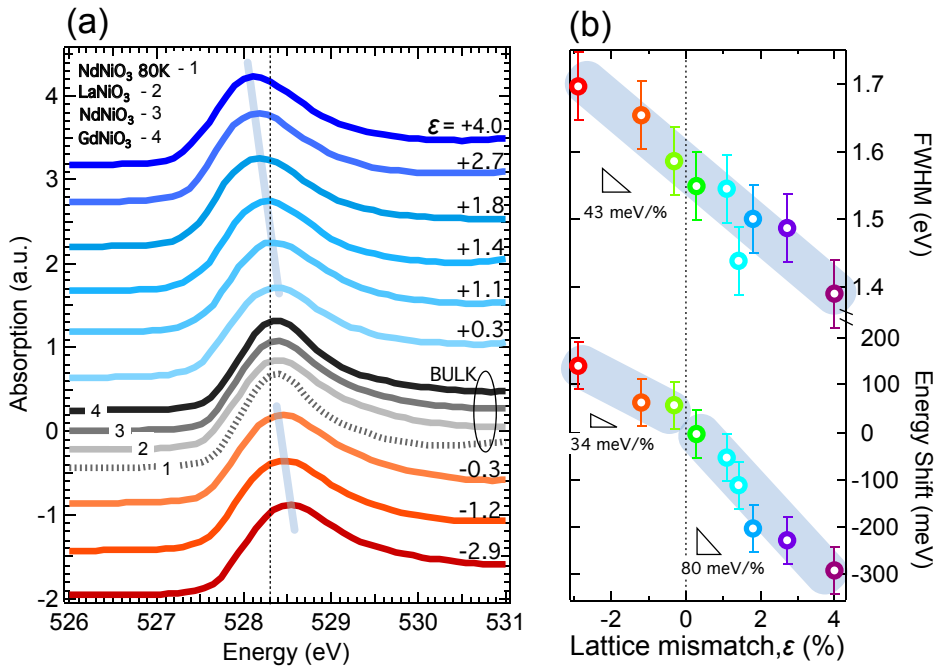

Figure 4.4: Bi-axial strain-induced covalency changes in NNO ultrathin films: (a) Low energy O K-edge pre-peak absorption around 528.5 eV for compressive (red) and a range of tensile (shades of blue) strain states (a.u., arbitrary units). The higher energy peaks above 530 eV correspond to the transition into La $5d4f$ and Ni $4s4p$ states and are omitted for clarity. (b) the normalized full-width at half-max (FWHM) and (c) energy shift relative to the bulk $RNiO_3$ energy position with respect to lattice misfit.

compressive to tensile side is also confirmed. The simultaneous variations of these energy scales uncover the control of heteroepitaxy on the self-doping mechanism via the ligand hole density.

Collective Phase Behavior

To investigate the effect of the self-doping mechanism on the MI transition and the collective ground state of NNO, we performed temperature-dependent resistivity measurements using the *van der Pauw* method. The normalized resistivity as a function of temperature is shown in Fig. 4.5. As seen, while at high temperatures the metallicity is maintained in all films, a remarkably different response emerges at low temperatures between the tensile and compressive strain with a systematic evolution in between. Specifically, under large tensile strain ($\sim$+1.8%) the samples show the presence of a strong MI transition with a sizable thermal hysteresis, characteristic of the bulk-like cooperative first order transition into the SO and CO state [112]. By lowering strain towards the

lattice-matched case (∼+0%), the high resistivity of the insulating ground state at low temperature ($\rho(2\text{ K})/\rho(\text{RT}) \approx 10^3$) decreases towards the much less resistive state ($\rho(2\text{ K})/\rho(\text{RT}) \gtrsim 1$) indicative of an increasing charge stiffness in the insulating phase. Meanwhile, as seen in Fig. 4.5, the hysteresis coercivity (the width of the hysteresis) also rapidly weakens. Since the hysteresis appears due to the cooperative SO and CO, this closing of the hysteresis signifies the decay of the SO [112]. The coercivity eventually vanishes as no hysteresis is observed at +0.3%, implying the absence of long-range magnetic ordering albeit with an insulating ground state. With the magnitude of strain increases above +1.8%, the coercivity also slowly decreases. As the lattice mismatch passes through zero towards compressive strain, the MI transition is completely quenched and a new highly metallic ground state emerges (see Fig 4.5).

To map out the phase space of the $NdNiO_3$ ultrathin films, we deduce the phase behavior by tacking two temperatures from the resistivity data. The first one is the resistivity minimum temperature T^{**} which marks the verge of $\frac{d\rho}{dT}|_{T=T^{**}} = 0$ and the emergence of a charge gap of the MI transition. The other one is the resistivity inflection point ($\frac{d\ln\rho}{d(1/T)}|_{\max}$) during the thermal hysteric behavior; we denote this temperature as T_N. The evolution with heteroepitaxial strain is summarized in the lattice mismatch-temperature phase space in Fig. 4.6(a). It is first interesting to note that, in sharp contrast to bulk $NdNiO_3$ which has an antiferromagnetic insulator (AFI) ground state with T_{MI} =200 K, ultrathin $NdNiO_3$ is tuned by heteroepitaxy to the verge of a localized-to-itinerant crossover around zero lattice mismatch. While an insulating ground state is continuously developing as approaching large tensile strain, a metallic ground state is maintained on the compressive side. This suppression of the bulk ordering around zero strain can be attributed to the inevitable heteroepitaxy-induced crystal symmetry mismatch with the substrates and the coherent interface-imposed elastic boundary condition. The former can drastically distort the lattice and particularly the octahedral units even in the absence of average lattice mismatch, while the latter may frustrate collective long-range orders (e.g. CO) that strongly couples to the lattice degrees of freedom.

Such a localized-to-itinerant crossover also infers that the heteroepitaxial $NdNiO_3$ is in prox-

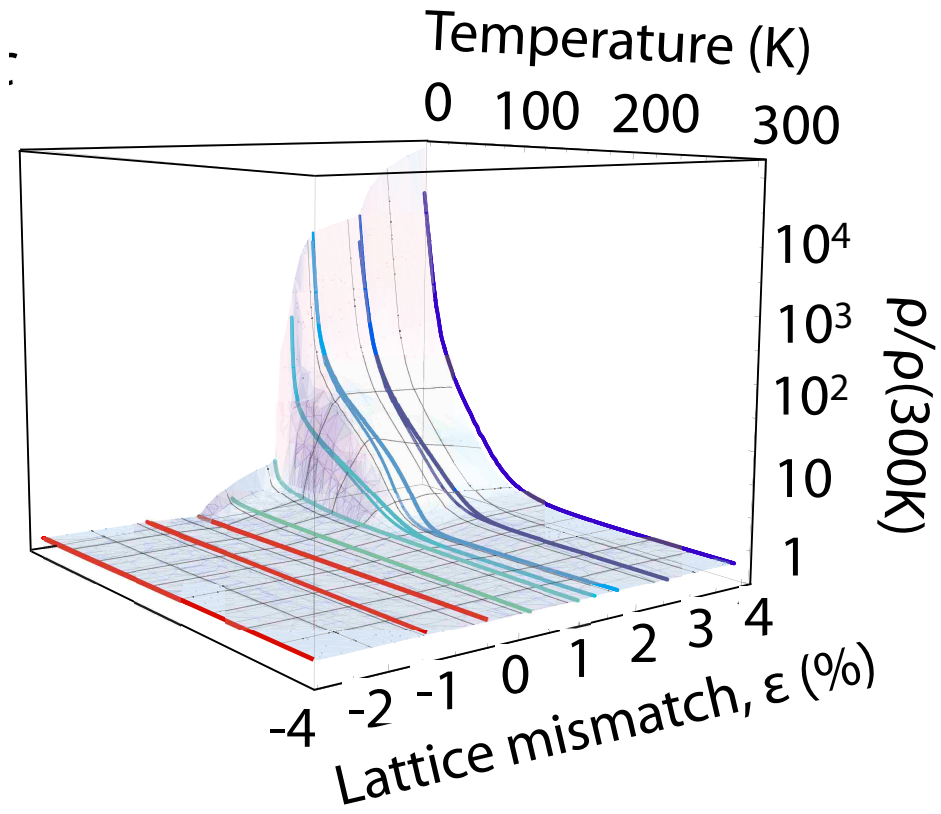

Figure 4.5: Normalized resistivity versus temperature with different lattice mismatches. Hysteresis is shown with cooling (green) and warming (blue) curves.

imity to quantum criticality with the critical lattice mismatch around zero, which is manifested in the evolution of T^{**} and T_N. Specifically, one can see that, under large tensile strain, T^{**} occurs at much higher temperatures than T_N; the opening of the charge gap tends to decouple from the magnetic ordering, implying an intermediate paramagnetic insulating phase in between. As the strain reduces, T^{**} and T_N become merging together; T^{**} is quickly decreasing, while T_N is gradually rising. This behavior is also reflected in the enhancing thermal hysteresis. Around $+1.8\%$ lattice mismatch, T^{**} and T_N exhibit parallel responses to strain, representing a broadened boundary separating the high-temperature paramagnetic metal (PM) phase and the AFI ground state. Upon further lowering the tensile strain toward zero, T_N vanishes rapidly with the weakening thermal hysteresis; the thermal hysteresis is completely closed at $+0.3\%$ lattice mismatch. T^{**}, on the other hand, is present albeit suppressed to zero relatively slowly. These different behaviors of T^{**}

and T_N indicates that a weakly insulating ground state exists without the antiferromagnetic (AFM) ordering in the vicinity of the quantum criticality. In this phase, remnant short-range magnetic correlations likely remain for the spin degree of freedom and may even result in exotic state such as spin liquid.

On the other side of the quantum MI transition, the temperature-induced MI transition is completely quenched and a new metallic ground state is developed as entering the compressive side. A fit-free analysis (see Fig. 4.6(b)) indeed reveals a low-temperature $T^{4/3}$ power-law behavior of the resistivity, characteristic of the non-Fermi liquid (NFL) behavior in the vicinity of a quantum critical point associated with the AFI phase as previously demonstrated in the bulk $PrNiO_3$ under hydrostatic pressure [110]. The power exponent of the NFL behavior also increases to $\sim$5/3, as the compressive strain increases further away from the the quantum criticality. A direct comparison to the bulk however shows that the NFL behavior here has much higher onset temperatures denoted as T' (e.g. 180 K vs. 60 K), implying strongly enhanced quantum fluctuations in the heteroepitaxial strain-stabilized quantum critical state. In addition, the rapid collapse of the SO observed here with an emerging state between the AFI phase and the NFL state is also absent in the case of pressure-control, highlighting the contrast of the quantum melting under heteroepitaxial strain observed here.

To directly detect the AFM ordering, we performed resonant x-ray diffraction measurement on the magnetic vector q =(1/4,1/4,1/4) in the pseudocubic notation. By utilizing the resonance at the Ni L-edge, this method strongly enhance the Bragg reflection due to the AFM-ordered spins on the Ni sites. Figure. 4.7 shows the development of the AFM ordering peak at (1/4,1/4,1/4) with decreasing temperature at $\varepsilon = +1.8\%$, corroborating the spin ordering (SO) in the AFI phase. In contrast, such an ordering was not found at +0.3%, consistent with the absence of thermal hysteresis in transport measurements and the absence of any long-range magnetic ordering.

This entire evolution of system demonstrates the capacity of heteroepitaxy in controlling the MI transition, reflecting the modulation in the Ni-O covalency unraveled in O K-edge XAS. The observed rapid collapse of the SO and the presence of an extended crossover region of strain where

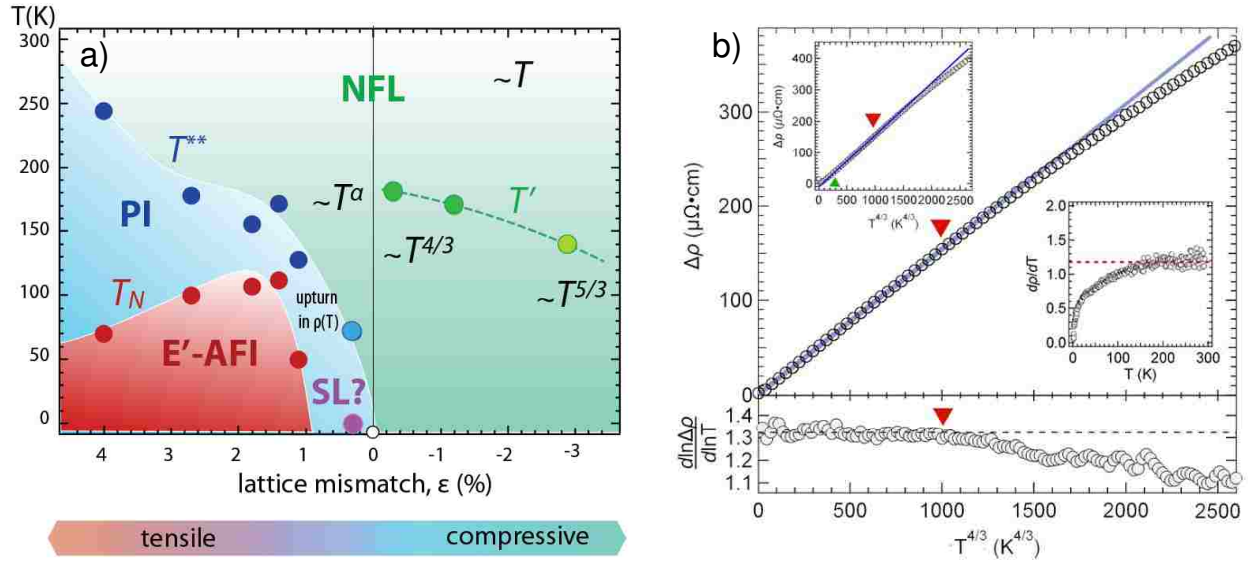

Figure 4.6: (a) lattice mismatch-temperature phase diagram. NFL, PM, PI, AFI and SL denote non-Fermi liquid, paramagnetic metal, paramagnetic insulator, antiferromagnetic insulator and spin liquid, respectively. The lines are guides to eyes. (b) $\Delta\rho$ versus $T^{4/3}$ for $NdNiO_3$ at -0.3% (upper) and the power-law exponent extracted from $d\ln\Delta\rho/d\ln T$ (lower). The solid line is a linear fit. Inset: (bottom right) $d\Delta\rho/dT$ is a constant at high temperatures, showing a T-linear behavior; (top left) $\Delta\rho$ versus $T^{4/3}$ at -1.2%. Dashed lines are guides to eyes.

the long-range magnetic order is absent in the insulating ground state highlight the importance of the modulation in the self-doping and its contrast with the conventional bandwidth-control under which the SO is always coupled with the CO at the MI transition [112]. In self-doped systems, the CO occurs on the self-doped ligand holes while local moments on the TM sites are responsible for the SO. The emerging magnetic order then very sensitively depends on the self-doped hole density of the bridging ligands which defines the fine balance between the FM and AFM types of Ni-O-Ni coupling [27]. Consequently, a small deviation in the degree of self-doping transpires to cause magnetic frustration and destroy the SO bearing the resemblance to the rapidly quenched AFM order and the magnetically disordered insulating (charge nematic) ground state in lightly hole-doped cuprates [42, 16].

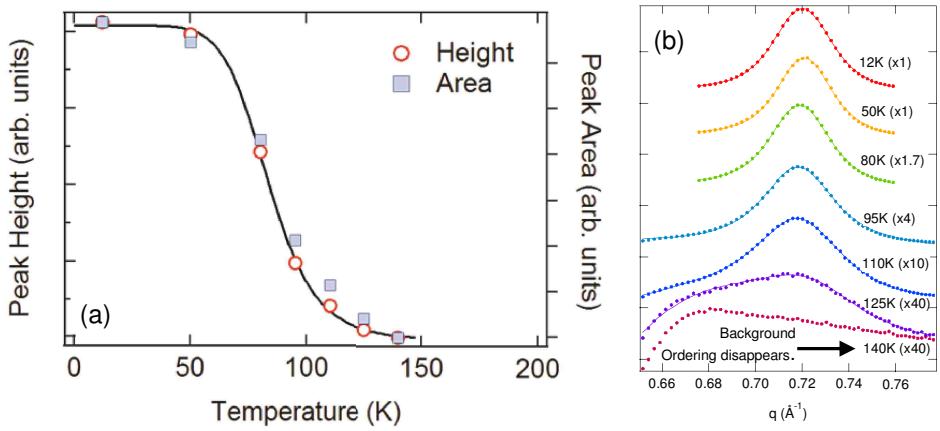

Figure 4.7: Resonant x-ray diffraction on the magnetic ordering vector. (a) temperature-dependence of the magnetic Bragg reflection peak (b) height and area.

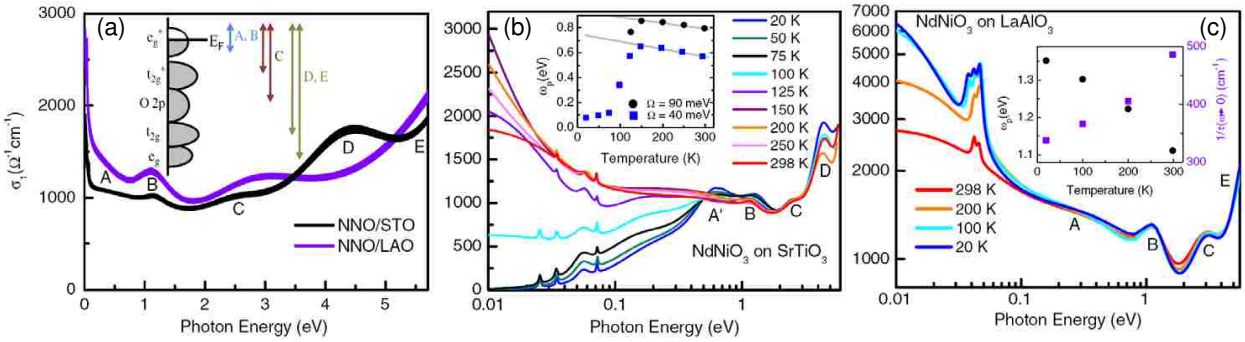

Figure 4.8: Real part of the optical conductivity for NNO on LAO and STO. (a) results at 298 K. The error bars are represented by the thickness of the curves. Inset: sketch of the NNO DOS [85, 106]. (b) NNO on STO across the MI transition. Inset: ω_p obtained from Eq. (1) with Ω =90 meV and plasma frequency obtained with Ω =40 meV. The gray lines are guides to the eye. (c) NNO on LAO at various temperatures. The Drude resonance remains prominent at all temperatures and no MI transition is observed. Inset: ω_p and 1=τ obtained from Eqs. (1) and (2).

Correlation Nature of the Metal-Insulator Transition

With the well controlled MI transition in high-quality single crystal NNO films, we performed temperature-dependent optical conductivity measurement to shed lights into the nature of the system's electrodynamics, especially in the ordered AFI phase. We first consider the real part of the optical conductivity $\sigma_1(\omega)$ given by $\sigma(\omega) = \frac{i\omega[1-\varepsilon(\omega)]}{4\pi}$, where $\varepsilon(\omega)$ is the complex dielectric function. The room temperature $\sigma_1(\omega)$ for the NNO films at +2.7% (on STO) and -0.3% (on LAO) lattice mismatch is showed in Fig. 4.8(a). Below 2 eV the two spectra exhibit the same gross fea-

tures: a Drude peak and two interband transitions labeled A and B in Fig. 4.8(a). Based on bulk band structure calculations showing a $t_{2g}^6 e_g^1$ electronic configuration [85, 106], features A and B can be attributed to transitions between the occupied and unoccupied antibonding e_g^* states (see inset in Fig. 4.8(a)). Above 2 eV, more marked differences between the two spectra are evident. Feature C is broader and centered at higher frequency for the film on LAO and a peak at 4.5 eV (feature D) is only evident for the film on STO. Feature C can be assigned to transitions from the t_{2g}^* and the nonbonding O $2p$ states to the e_g^* orbitals. Finally, D and E could be the result of excitations from the bonding t_{2g} and e_g levels to e_g^*.

Figure 4.8(b) shows the optical conductivity at various temperatures with +2.7% lattice mismatch. At low temperatures the Drude peak disappears as the system enters the insulating state. The spectral weight of feature A rapidly decreases and a new peak emerges at 0.65 eV (A' in Fig. 4.8(b)). This transfer of spectral weight from the Drude resonance to a finite energy peak is typical of charge-ordered systems in the regime of weak electron-lattice coupling [75, 18]. However, feature A', which is likely due to transitions between the e_g^* states that are gapped in the insulating state, only accounts for part of the lost Drude spectral weight. Therefore, we must take into account feature D, which also shows a strong temperature dependence opposite to that of the Drude response; its spectral weight decreases as the temperature is raised across the MI transition. Thus, this resonance is clearly involved in the spectral weight transfer that leads to the opening of the correlated gap. Figure 4.8(c) shows $\sigma_1(\omega)$ for the NNO film with -0.3% lattice mismatch. In contrast with that under large tensile strain, the Drude resonance remains prominent at 20 K and its magnitude increases. The peak A' that arises features A and B at low temperature as a result of the MI transition is not seen. This is consistent with the transport measurements described above.

To quantitatively study the temperature dependence of the Drude resonance in the metallic phase we consider the plasma frequency ω_p given by

$$\frac{\omega_p^2}{8} = \int_0^{\Omega} \sigma_1(\omega) d\omega \tag{4.1}$$

where Ω is the cutoff frequency chosen to include only the coherent contribution to $\sigma_1(\omega)$. In conventional metals the free carrier spectral weight is unaltered with temperature and the entire temperature dependence of the Drude absorption is due to a decrease in the scattering rate $1/\tau$. Correlated metals, on the other hand, often exhibit an exotic temperature dependence of ω_p [72]. In the normal state of high-T_c cuprates, for instance, a $\sim$2% enhancement in ω_p has been measured and can not be explained by the Sommerfeld model [3]. To obtain ω_p, we used Ω=125 meV and 90 meV for the film with -0.3% and +2.7% lattice mismatch, respectively, before the onset of feature *A*. As seen in the insets of Figure 4.8(b) and (c), both samples exhibit a low-temperature enhancement of ω_p, confirming the correlation effects in the metallic phase.

To investigate where the Drude spectral weight is transferred in the insulating phase, we first used Ω=2 eV for the film with +2.7% lattice mismatch. The resulting spectral weight which includes features *A* and *B* right above the charge gap is, however, still temperature dependent. We found that the total spectral weight is nearly the same at all the measured temperatures when Ω is as large as 5.6 eV including feature *D*. This spectral weight transfer within such a large energy range is drastically different from systems where the MI transition is caused by CO/SO. These orderings would only lead to the opening of a charge gap with a transfer of the free carrier spectral weight to resonances immediately above it [18]. In Fe_3O_4, for example, the redistribution of spectral weight is restricted to only 10 times the size of the energy gap [75], much smaller than the 30 times observed here for NNO. Our data are also in contrast with spin density wave systems, such as $Cd_2Os_2O_7$ [73], in which the gap closes continuously. Instead, like in other Mott systems [79], $\sigma_1(\omega)$ here increases gradually in the gap region as it is filled with states. Thus, these two observations suggest that the underlying driving force for the MI transition is strong electron-electron interaction as spectral weight is transferred on the scale of U between the Hubbard band and the quasiparticle peak. Meanwhile, the CO/SO is likely to play a role in initiating the MI transition as a triggering mechanism.

Chapter 5

Quantum Confinement on Correlated Electrons

Recently, artificial confinement of Mott electrons is emerging as a compelling route to create novel (quasi-)two-dimensional (2D) systems unobtainable in the bulk form [4, 53]. The confinement utilizes the quantum size effect to control electronic properties in heterostructures. Unlike lattice mismatch, which introduces by straining the whole film as a single system, quantum confinement may tune the parent system into a completely different material. Confining dimension and confining interface are the two key control parameters; while the former constrains the electrons in a potential well by blocking the hopping behavior in a certain direction, the latter represents the boundary condition of the potential well. When the confining dimension is smaller than the electronic length scale, a system effectively becomes a new (quasi-)2D material defined by the confining interfaces. In this chapter, we will discuss the effects of quantum confinement on correlated electrons in complex oxides. We will first show how quantum confinement induces a metal-insulator (MI) transition during the dimensional crossover and how the orbitals response in the 2D limit. To directly demonstrate the role of the interface in determining the ground state of correlated electrons, we will also compare two different quantum well geometries.

5.1 Dimensionality-Control

5.1.1 Introduction

While artificial 2D Mott materials are extremely appealing, comprehending the underlying physics and rationalizing property tailoring are formidable challenging because of the profound many-body physics and the ultrathin structure at nano or even atomic scale. An effective way for tackling this problem is to investigate the crossover from the three dimensional (3D) or bulk-like regime when subject to quantum confinement. In particular, study on the Mott MI transition during this process

in heterostructures is crucial as it has been for the bulk systems [42]. While the MI transition is conventionally driven by the bandwidth-control, recent work showed that the number of monolayers within ultrathin films can be used to fine tune the t_{2g}^1-system based on $SrVO_3$ from a bulk correlated metal into a thin Mott insulator [108]. This dimensionality-control can be a novel way to modulate Mott materials in the quantum confinement regime.

Confined e_g^1-system based on the Ni^{III} ($3d^7$) low-spin state in perovskite nickelate $RNiO_3$ (R=rare earth) is another example of great interest. As mentioned in Chapter 1, novel exotic quantum states, including topological phases [81, 107] and unconventional high-T_c superconductivity [14, 34, 31], have been proposed. These proposals has been put forward to use heterostructuring and orbital engineering by constructing quantum well structures consisting of alternating unit-cell (u.c.) thin layers of a correlated metal $LaNiO_3$ (LNO) and a band-gap dielectric $LaAlO_3$ (LAO). Despite the attractive simplicity of this quantum confinement structure, the experimental realization of a LNO/LAO superlattice (SL) presents a large degree of ambiguity in selecting a specific electronic ground state caused by (i) the intrinsic propensity of orthonickelates to charge ordering (CO), (ii) orbital polarization due to chemical confinement imposed by interfacial bonding [31], (iii) polar discontinuity described in Chapter 3. Thus, driving the confined LNO slab across the dimensional crossover provides an efficient mean to understand the nature of the correlated electron ground state in quantum well geometry. In this section, we will discuss our investigation on the dimensional crossover and the confinement-induced MI transition in LNO/LAO SLs.

5.1.2 Results and Discussion

High-quality epitaxial $[(LNO)_n/(LAO)_3]_N$ SLs ($n = 3$, 5 and 10 with $N = 10$, 4 and 2 respectively) were grown by laser molecular beam epitaxy (MBE) as described in Chapter 2. +2.2% tensile strain is applied with TiO_2-terminated (001) $SrTiO_3$ (STO) substrates. To explicate the evolution of the ground state due to quantum confinement, DC transport measurements from 400 K to 2 K were performed by using the *van der Pauw* method. The obtained temperature-dependent conductivity $\sigma(T)$ of the SL series is shown in Fig. 5.1(a). A transition from metallic to insulating behavior can

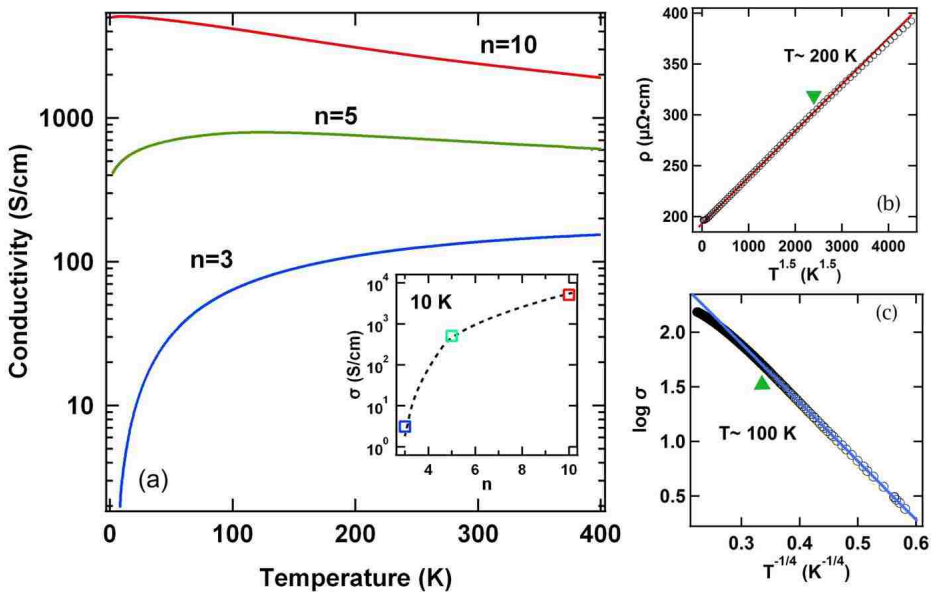

Figure 5.1: (a) Conductivity of $(LNO)_n/(LAO)_3$ SLs versus temperature. Inset: conductivity versus n at 10 K. The dashed line is a guide for eye. (b) Resistivity as a function of $T^{1.5}$ at $n = 10$. The red solid line is a guid for eye. (c) $d\ln\sigma$ as a function of $1/T^{1/4}$ for the $n = 3$ SL shows the low temperature three dimensional variable range hopping behavior.

be clearly seen with decreasing n. The inset of Fig. 5.1(a) also demonstrates orders of magnitude change in σ across the series taken at 10 K. As seen, in analogy to the bulk LNO, the $n = 10$ SL exhibits a highly metallic behavior ascribed to the three dimensional regime. On the other hand, unlike the bulk, which is known to follow a $T^{3/2}$ dependence at room temperature and switch to a low-temperature T^2 Fermi liquid behavior [112, 38, 105], the resistivity ρ at $n = 10$ switches from a T-linear behavior above 200 K to a $T^{3/2}$ power law (see Fig. 5.1(b)). Note that, while a T-linear dependence was also found in the high-temperature metallic phase of other members of the bulk $RNiO_3$ family who have a charge-ordered insulating ground state [68], the low-temperature $T^{3/2}$ behavior of Fermi liquid electrons has been attributed to scattering by bond-length fluctuations due to proximity to a Mott-type MI transition from the itinerant side [80]. These phenomena indicate enhanced electronic correlations in the quantum confinement regime and stronger vibronic fluctuations associated with charge ordering.

The intermediate thickness $n = 5$ SL still shows a clear metallic behavior at high temperatures but reaches a conductivity maximum at T_{max}= 120 K. While the metallicity of LNO films under

large tensile strain is known to cease when the thickness is $\leq$ 3nm [87], it is remarkable that the high-temperature metallic behavior is well maintained in such a thin slab ($<$ 2nm). This result unambiguously highlights the exquisite role of the confinement structure with interfaces in defining the transport properties of SLs as compared to the bulk LNO and single layer films. Notice, the conductivity σ here is also well below the Ioffe-Regel limit [63] ($\sim$ 2000 S/cm), manifesting the modification of the correlation nature of the observed behaviors and the minor role of disorder. Below $T_{\max}$, $\sigma(T_{\max}) - \sigma(2\text{ K})$ ($\sim$381.6 S/cm) is as large as $\sigma(2\text{ K})$ and almost twice of $\sigma(T_{\max}) - \sigma(400\text{ K})$. Neither hopping conductivity nor quantum corrections is found to be able to account for this $d\sigma/dT > 0$ region. This transitional behavior explicitly indicates that all the involved interactions and relevant energy scales, like electron correlations and the bandwidth, are of a similar strength and strongly competing with each other. Thus, $n = 5$ falls into a critical region of the confinement-controlled MIT. Upon further decreasing n to 3, $d\sigma/dT > 0$ at all temperatures and a variable range hopping behavior was found below 100 K (see Fig. 5.1(c)), indicating that finite density of states remains within the opening gap during the dimensional crossover.

To elucidate the origin of the MI transition induced by quantum confinement, we compare the dimensional crossover with the layer extension of cellular dynamical-mean-field theory (layer CDMFT) [48] which takes into account the competition between the short-range correlations and the reduced bandwidth. To make the problem tractable and yet relevant for the SLs, we considered the multi-layered single-band Hubbard model for Ni $3d$ and simulated the high-energy Al $3s$ states as vacuum. Note that CDMFT was recently applied to explain the opening of a correlation-induced pseudogap in $SrVO_3$ thin films [108]. The effective impurity model for each layer consisting of 2×2 plaquette coupled to 8 bath orbitals and is solved by using the Lanczos exact diagonalization method [10]. The layer CDMFT employed here goes beyond that previous study by including short-range correlations within each monolayer to capture the physics of pseudogap. The short-range correlation is antiferromagnetic as recently suggested in a similar system with the planar $d_{x^2-y^2}$ orbital configuration [33]. To neutralize the CDMFT's overemphasis on the in-plane correlations, we introduce a small anisotropy between the in-plane t_{in} and out-of-plane t_{out} hopping

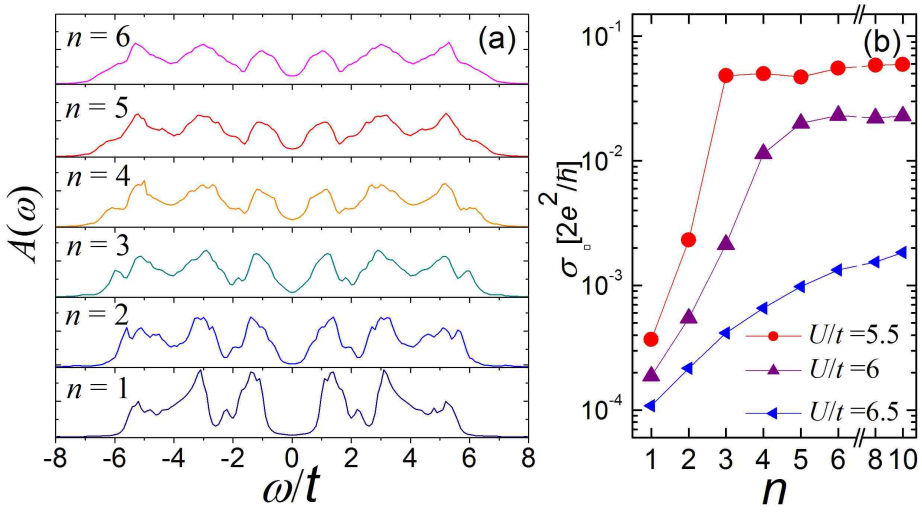

Figure 5.2: Layer CDMFT results for the multilayer Hubbard model with various thickness n. The transfer anisotropy δ is set at 0.2. (a) Average spectral function for $U/t = 6$. (b) Sheet conductance $\sigma_{\square}$ versus n for $U/t = 5.5$, 6 and 6.5.

integrals as $t_{in} = t(1-\delta)$ and $t_{out} = t(1+2\delta)$ so that t_{out} competes with the in-plane correlations. The bandwidth of the bulk non-interacting system is unchanged, $W = 12t$.

Since bulk LNO is a metal we consider moderate values of U/t ($U = 6t$). Fig. 5.2(a) presents the n-dependent evolution of the spectral function. As clearly seen, the correlation gap in the two dimensional limit is filled up and becomes a pseudogap with increasing n, lending theoretical support to the notion that the experimentally observed MI transition arises from the dimensional evolution of a quantum confined correlated carriers transforming from an insulator to a metal through a "bad" metal phase. Notice, the sharp quasiparticle peak is absent at $\omega = 0$ even in the thickest slab because out-of-plane correlations are treated on a mean-field level. To see the relation between the (pseudo) gap opening and the anomalous transport properties, sheet conductance $\sigma_{\square}$ is computed by the standard Kubo formula. An imaginary part $\eta = 0.1t$ was introduced to the real frequency ω to represent the finite impurity scattering. As shown in Fig. 5.2(b), with increasing n, $\sigma_{\square}$ increases continuously and becomes practically unchanged above a critical thickness n_c below which the pseudogap is pronounced. These results reproduce well the critical regime at $n_c \approx 5$ in the transport measurements and strongly suggest the confinement-controlled short-range electron correlations as the origin of the observed MI transition.

From the comparison above, we can see that the essential physics of metal-insulator crossover by the quantum confinement is captured by the CDMFT. On the other hand, as discussed earlier, it is known that rare-earth nickelates also have an intrinsic propensity towards the local charge disproportionation upong entering the insulating phase [11]. The result is a complicated 3D ordering of both charge and spin which might emerge as a competing ordering. To gain microscopic insight into the local electronic structure and the effect of confinement on the MI transition, we carried out detailed x-ray absorption spectroscopy (XAS) measurements. All spectra were acquired in the bulk-sensitive fluorescence-yield mode at the Ni *L*-edge. The normalized spectra obtained at 300 K are shown in Fig. 5.3(a,b). The La M_4-edge which partially overlaps with the Ni L_3-edge was subtracted with a Lorentzian profile. For direct comparison, the *L*-edge spectra of bulk LNO and $SmNiO_3$ are included. As seen, the energy position and the lineshape of the SLs are close to those of the bulk $RNiO_3$ [57, 78], indicative of a Ni^{III} charge state of the low-spin configuration. On the other hand, while the multiplet effects are smeared in the metallic bulk LNO, the L_3-edge spectra of the SL show a pronounced two-peak structure (shaded in green), closely resembling the absorption spectrum of the bulk $SmNiO_3$ (see Fig. 2.(a)), which in the bulk is a well studied case for the charge-ordered ($2Ni^{III} \rightarrow Ni^{II} + Ni^{IV}$) insulating state [56, 11]. As n decreases this multiplet effect becomes more pronounced, particularly in moving from $n = 10$ to 5. The energy separation of the two split peaks is also clearly increasing as shown in Fig. 5.3(c). The corresponding trend at the L_2-edge emerges as a developing low-energy shoulder at about 870.5 eV (see Fig. 5.3(b)). The observed evolution is reminiscent of that reported for the bulk $RNiO_3$ when crossing the MI boundary [78], unambiguously revealing the carrier localization in the presence of a developing correlated charge gap in the quantum-confined LNO slabs and a latent tendency to CO during the 3D-to2D crossover. In accordance with the observations from DC transport, the emergence of the multiplet even in the relatively thick LNO slab ($n = 10$) lends solid support to strongly confinement-enhanced correlations. Meanwhile, when subject to this enhancement, the inclination to CO corroborates its role as a primary competing ground state not only in the bulk [56] but also in the predicted heterostructured LNO [14].

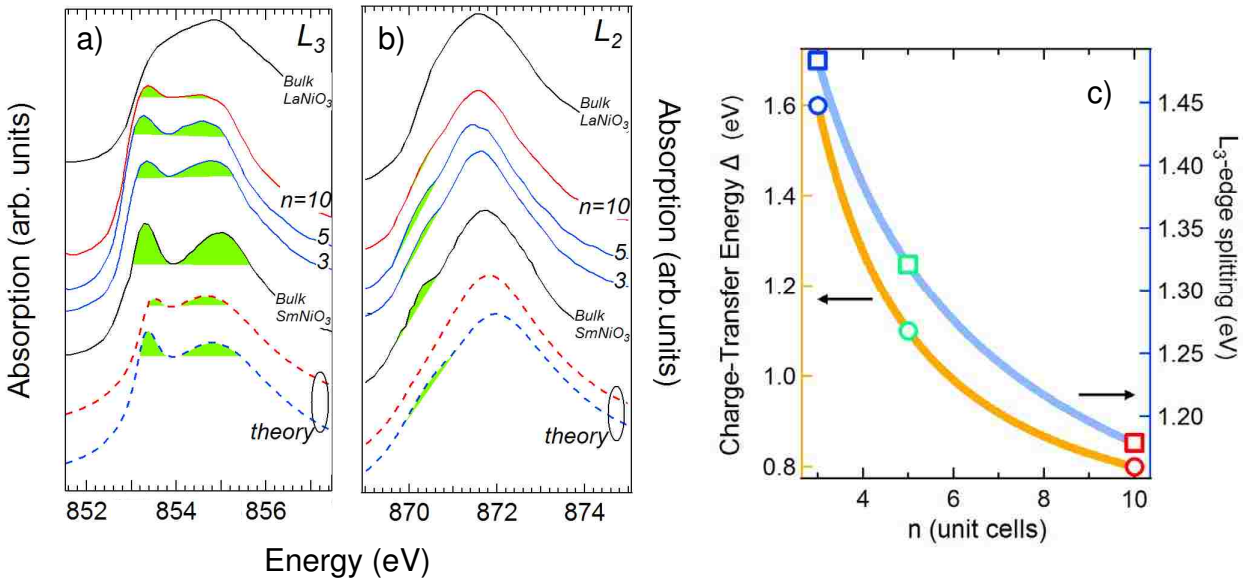

Figure 5.3: X-ray absorption spectra of $(LNO)_n/(LAO)_3$ SLs at the L_3-edge (a) and L_2-edge (b) for $n = 3, 5$, and 10 together with the theoretical calculations done for a NiO_6 cluster for a charge transfer energy of 0.8 (red) and 1.6 (blue) eV. Spectra of bulk LNO and $SmNiO_3$ are included for comparison. The shaded (green) areas indicate the most significant changes during the evolution. (c) The observed multiplet splitting energy (square) and the corresponding calculated charge transfer energy (circle) versus n. Solid lines are fits to power-law.

To shed additional light on the observed spectroscopic results, we compared the results with simulated spectra from cluster calculations on a NiO_6 cluster. The model Hamiltonian includes on-site energies, crystal field, Coulomb interaction including the full multiplet structure and spin-orbit coupling [100]. The majority of the parameters are equivalent to those in Ref.[100]. The monopole part of the Coulomb interaction is set at 6 eV. The major configurations used in the calculation are $\underline{d}^2_{e_g,\uparrow}\underline{d}_{e_g,\downarrow}$ and $\underline{d}^2_{e_g,\uparrow}\underline{L}_{e_g,\downarrow}$, where $\underline{d}_{e_g,S}$ and $\underline{L}_{e_g,\downarrow}$ stand respectively for a $3d$ hole and a ligand hole with e_g symmetry and spin $S = \uparrow, \downarrow$. The degree of Ni-O covalency here is varied by changing the charge-transfer energy Δ. Figure 5.3(a) shows the result of calculations when Δ was varied from 0.8 eV to 1.6 eV. The calculation strongly implies that when the local Ni-O covalency is reduced with increasing Δ, the observed evolution of the L_3-edge multiplet splitting with n is well reproduced. To quantify the n-dependence, the value of Δ for each SL is obtained by matching the corresponding size of the splitting. As can be seen in Fig. 5.3(c), the n-dependence of Δ clearly tracks that of the energy separation of the split peaks at the L_3-edge.

With this excellent agreement between the experimental spectra and the calculation, we can speculate on a possible physical origin of the $n-$dependence of the correlated gap energy. The increasing magnitude of Δ with decreasing number of LNO u.c. can be connected to the effect of the confinement which breaks the translation symmetry with interfaces and causes the formation of a significantly less covalent Ni-O-Al chemical bond. The absence of d-electron states on Al and its much lower electronegativity compared to Ni strongly suppresses the ligand hole density on the apical oxygen O_a [31]. Consequently, because of the proximity to the more positively charged Al ion, the Madelung potential on the interfacial O_a is further raised with respect to the planar O_p; this leads to further suppression on the apical hole density and charge transfer process. As a result, the interfacial Ni-O_a bond length becomes shorter [14], the ligand hole is transferred into the NiO_2 plane and the $d^8\underline{L}$ configuration will acquire more of the x^2-y^2 character. This effect is in close analogy to the physics of cuprates where the Madelung energy of the apical oxygen and the Cu-O_a bond length are believed to be important parameters to control the planar hole density and to stabilize the Zhang-Rice states upon hole-doping [62].

5.2 Orbital Response to Confinement

5.2.1 Introduction

Having discussed the Mott-type MI transition during the dimensional crossover, here we present our study on the possibility of chemical control of orbitals in the 2D limit in single-unit-cell LNO/LAO SLs. Recall that, in Chapter 4, we showed an asymmetrical orbital response to strain in the 3D regime. To isolate the effect of interfaces from that of strain, we also investigated SLs under both compressive and tensile strains. The results show orbital splitting in the SLs under both strain states but in different fashions. The splitting under compressive strain is consistent with expectations of elastic theory, but no significant orbital polarization was observed. The SL under tensile strain, on the other hand, shows no evidence of crystal field splitting yet displays a significant x^2-y^2 orbital polarization. These behaviors manifest a concerted effort of broken symmetry at the interface, chemical confinement, and heteroepitaxial strain in manipulating the orbital

polarization, confirmed by Density functional theory (DFT) calculations with an on-site Coulomb repulsion term.

5.2.2 Results and Discussion

Fully epitaxial $[(LNO)_1/(LAO)_1]_20$ SLs were grown on (001) TiO_2-terminated STO and LAO single-crystal substrates by laser MBE as described in Chapter. 2. As expected from the dimensional crossover discussed above, temperature-dependent resistivity measurements using the *van der Pauw* method showed that both SLs have insulating behaviors (see Fig. 5.4). The XAS was measured in bulk-sensitive fluorescence-yield mode at the Ni L-edge. From the polarization-averaged XAS, we determine that the valence of Ni is bulk-like 3+ testifying to the absence of oxygen vacancies (see Fig. 5.5(a)). The data are showed in comparison to bulk $NdNiO_3$ above and below the MI transition. A strong multiplet feature develops on the leading edge of both the L_3- and L_2-edges, which has been identified as a signature of localized carriers in charge-ordered insulating nickelates as discussed in the previous section. The similarity between the SLs and the bulk corroborate that a charge gap is open for the correlated electrons, in agreement with the transport measurements and the previously discussed confinement-induced Mott-type insulating ground state.

The effect of confinement and strain on orbital occupancies can be probed directly by light with tunable linear polarization. Due to the strong overlap between the La M_4- and Ni L_3-edges, however, for the polarization dependence we focus on the behavior at the L_2-edge only. First, in the case of compressive strain (LAO) as shown in Fig. 5.5(b), the spectrum with the out-of-plane polarization (V) exhibits a shift of $\sim$100 meV to lower energy with respect to that of the in-plane polarization (H). This energy shift is related to the energy scale for the strain-induced crystal field splitting which stabilizes the $3z^2 - r^2$ orbital via octahedral elongation distortion, consistent with the behavior in the 3D regime showed in Chapter 4. However, compared with the 3D regime, the two polarizations display much smaller difference in their absorption intensities in the SL, indicating rather similar population of the two e_g orbitals. This x-ray linear dichroism (XLD) is best

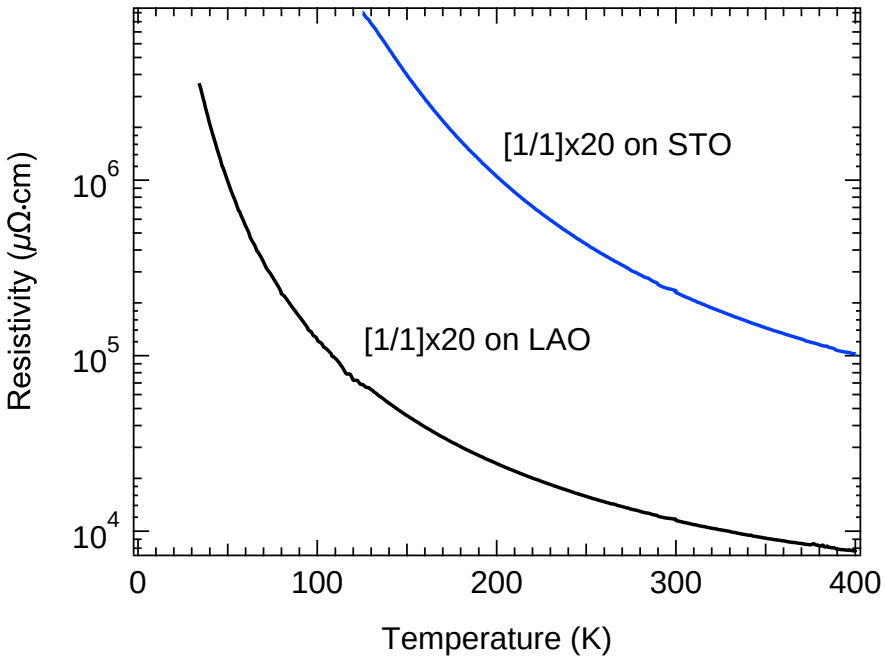

Figure 5.4: Resistivity of $(LNO)_1/(LAO)_1$ SLs versus temperature

seen in the difference spectrum showed in Fig. 5.5(b); the XLD shows a derivative like lineshape with equal positive and negative spectral weights, confirming that the polarization dependence originates from an energy shift between two spectra.

For the case of tensile strain, under the assumption of a symmetric strain response, one would expect a similar behavior with an opposite sign. But the data in Fig. 5.5(c) shows practically no energy splitting between the two orbitals. Instead, there is a significant difference in peak intensity between the two polarizations. The lack of energy shift strongly implies that the octahedra are rather undistorted from the uniform shape, resembling the behavior in the 3D regime showed in Chapter 4. On the other hand, even though there is no energy splitting between the e_g orbitals under tensile strain, the difference in intensity signifies a significant departure from the equal occupations of the $3z^2 - r^2$ and $x^2 - y^2$ orbitals in the 3D regime. In this case, the XLD spectrum shows a small negative spectral weight in the region of the rising edge of the absorption peak but a large positive signal near the peak maximum due to the difference in e_g orbital occupancies, indicative of an $x^2 - y^2$ orbital character for the e_g electron.

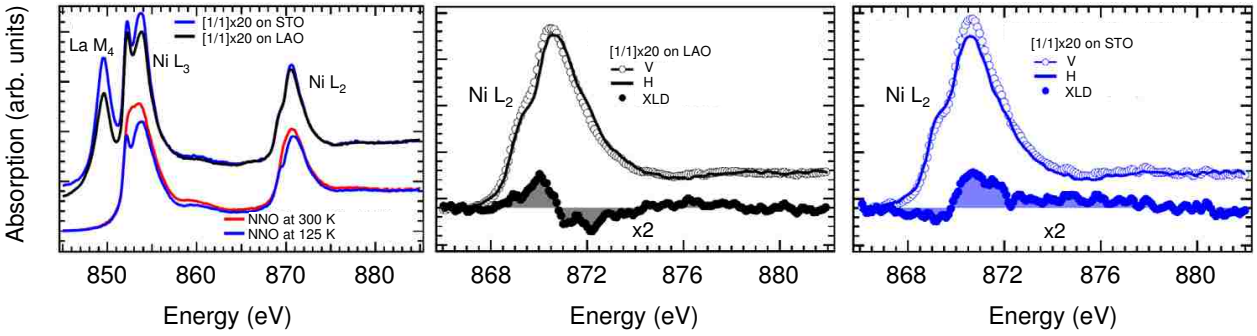

Figure 5.5: (a) Polarization-averaged Ni L-edge spectra of the $[1/1]_{20}$ SLs in comparison with bulk $NdNiO_3$ above and below the MI transition. Polarization-dependent absorption at the Ni L_2-edge for SLs under both compressive (b) and tensile (c) strain. XLD difference spectra ($I_{E\|c} - I_{E\perp c}$) are also included.

To quantify the differences in strain-dependent orbital occupancy, we integrate the area under the peak to count the number of unoccupied states (holes) which scales with the orbital occupancies. Proper counting of holes requires measurement of the entire L-edge, which is not possible due to the La M_4-edge intrusion into the L_3-edge. However, under the assumption that spin-orbit coupling in the $3d$ states is constant with strain, by integrating the L_2-edges we can extract the relative orbital occupancies [99]. For tensile strain though, there is a significant increase in the number of holes in the out-of-plane $3z^2 - r^2$ orbital states, i.e. a relatively larger electron occupancy of the $x^2 - y^2$ orbital. By defining orbital polarization through the relative areas, there is about 5% reduction in $3z^2 - r^2$ occupancy for tensile strain, while for compressive strain the orbital polarization is close to zero. This orbital polarization under tensile strain agrees well with recent measurements using polarized x-ray reflectivity [5].

The key feature under both tensile and compressive strain states can be concluded as the increased hole density on $3z^2 - r^2$ orbital in the SLs from that in the 3D regime. This behavior in proximity to the interface is consistent with the reduced covalency in the interfacial Ni-O-Al molecular bond suggested in the previous section. That is, compared with the oxygen orbitals in the NiO_2 plane, the much stronger ionicity of the Al-O bond versus the Ni-O bond reduces the bridging apical oxygen hole density in the $2p_z$ orbital by pulling the electron density from the Ni $3z^2 - r^2$ orbital. This effect gives rise to a chemical means of controlling the orbital occupan-

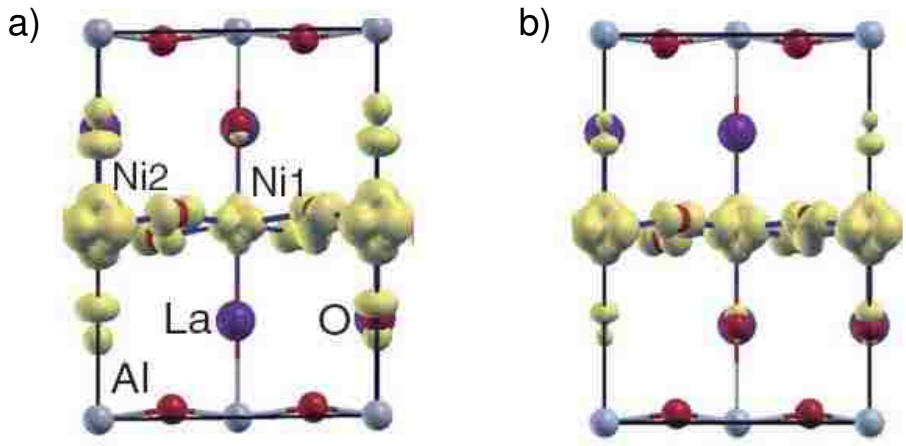

Figure 5.6: Distributions of unoccupied density of states between the Fermi level and 2.5 eV above in $(LNO)_1/(LAO)_1$ SLs under tensile strain (a) and compressive strain (b).

cies in addition to strain as also noted by a recent theoretical study [31]. To give more insight into this interfacial control, we compare the results with density functional theory calculations of $(LNO)_1/(LAO)_1$ SLs with the full-potential linearized-augmented-plane-waves method as implemented in the WIEN2k code [6]. Figure 5.6 shows the spatial hole density distribution for SLs under both strain states. As can be seen, the most profound effect is the reduction of the apical oxygen hole density when compared with that in the NiO_2 plane. This leads to a reduction in electron occupancy on the $3z^2 - r^2$ orbital under tensile strain even in the absence of crystal field splitting of the e_g orbitals. The $3z^2 - r^2$ orbital polarization due to octahedral distortion under compressive strain is also compensated by this effect. As a result, the ligand hole in the $3d^8\underline{L}$ state obtain a stronger in-plane character, corroborating the effect of the chemical confinement. Note that, for the SL under tensile strain, the CO ($2Ni^{3+} \rightarrow Ni^{3+\delta} + Ni^{3-\delta}$) is also stabilized in the calculation, leading to nearly complete suppression on the hole density at the apical oxygen of the $Ni^{3+\delta}$ site.

From above, we can see clearly that the orbital response and the ground state of the system is a result of the interplay of three control parameters: strain, confinement, and interfacial covalency. These results again highlight that rational manipulation of orbitals requires an understanding that extends beyond the conventional picture of how heteroepitaxial strain alters electronic properties.

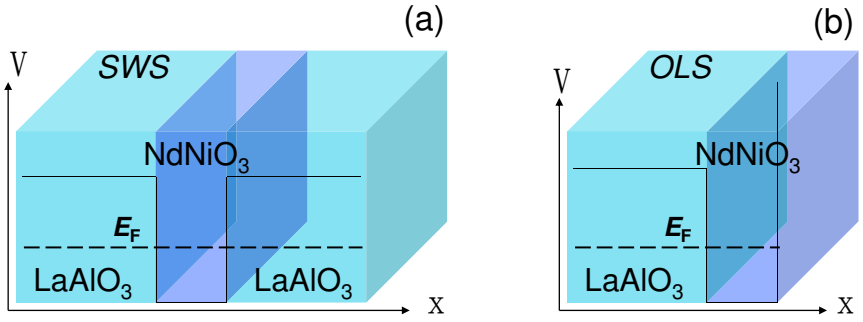

Figure 5.7: Cartoons of the two quantum well geometries with potential schematics. (a) Confinement by wide-gap dielectrics ($LaAlO_3$) on both sides (sandwiched slab). (b) Confinement by a dielectric ($LaAlO_3$) on one side and vacuum on the other.

In addition, the chemical control offers new opportunities to modulate orbital configurations in ultrathin oxide heterostructures even in the absence of strain.

5.3 Role of the Interface

5.3.1 Introduction

From the previous section we have seen how the confinement in the quantum well structure may control the orbital degree of freedom via interfacial coupling. The first section also shows that, under the quantum confinement, the ground state of LNO evolves from a 3D correlated metal to a (quasi-)2D Mott insulator with propensity to charge and spin orderings (CO/SO) in LNO/LAO SLs. On the other hand, reported results have suggested that LNO confined in the ultrathin film form has a similar itinerant-to-localized behavior [86, 30]. In addition, the underlying mechanism of confinement behind this Mott MI transition is under debates between theory and experiment [33, 50]. The key question therefore rests on the fundamental role of the confining interface in modulating the collective orderings in Mott quantum wells beyond affording the blocking boundary.

While previous studies were devoted to LNO, which is a paramagnetic metal in the bulk, $NdNiO_3$ (NNO) represents a more attractive case of a Mott insulator with cooperative orderings of charge and spin that can melt into a correlated metal under increased temperature [11, 58, 92],

and/or compressive heteroepitaxial strain as we showed in Chapter 4. In this section, we demonstrate the remarkable capability of the confinement boundary condition on controlling the emerging electronic phase transitions of strongly correlated system in e_g^1 quantum wells consisting of a NNO active layer. We investigated the dimensional crossover in two types of quantum wells (see Fig. 5.7) with both of them under an identical compressive strain. The first type involves a sandwiched well structure (SWS) where both sides are interfaced with dielectric LAO, while the other type employs an overlayer structure (OLS) where one of the confining boundaries is replaced by the interface with vacuum, i.e. surface. The results revealed that, while reducing dimensionality can introduce a MI transition in both confinement geometries, the transition temperature and the associated charge- and spin-ordered insulating ground state are remarkably enhanced in SWS compared with OLS. Polarization-dependent XAS also identified an orbital reconstruction between the two geometries, causing different degrees of CO instability that couples with the MIT.

5.3.2 Results and Discussion

To create the quantum wells, high-quality epitaxial NNO ultrathin slabs oriented along the pseudo-cubic (001) direction were grown by laser MBE, as described elsewhere in in Chapter 3. The compressive strain was achieved via the -0.3% epitaxial lattice mismatch with LAO single crystal substrates. While ultrathin films of NNO correspond to the LAO/NNO/vacuum OLS, additional 3-unit-cell (u.c.) slabs of LAO were added on the top to achieve the LAO/NNO/LAO SWS. The evolution of the ground state was studied by DC transport measurements from 300 K to 2 K using the *van der Pauw* method.

Figure 5.8(a) and (b) show the obtained temperature-dependent sheet resistance of two series of quantum wells of OLS and SWS, respectively, with the $NdNiO_3$ slab thicknesses of 15, 10, and 5 u.c.. As seen, while metallicity is well maintained at high temperatures in all samples, the OLS and SWS display distinctly different low-temperature evolutions upon reducing the confining dimension. Specifically, the 15-u.c. OLS remains metallic at low temperatures, which is expected as mentioned earlier due to the complete suppression of the bulk charge- and spin-ordered insulating

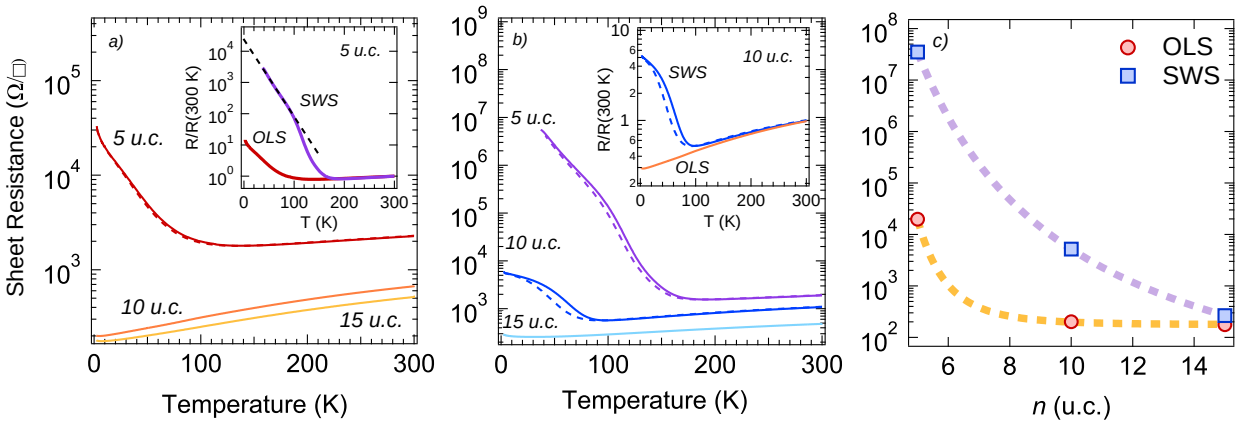

Figure 5.8: Sheet resistance versus temperature in NdNiO3 quantum wells under OLS (a) and SWS (b). Solid curves are warming data. Cooling data are shown in dashed curves for samples that have hysteresis. Inset of (a): warming curves for 5 u.c. slabs in both geometries. The dashed line is a guide to eye for the extrapolation to lower temperatures in SWS. Inset of (b): comparison of the 10 u.c. OLS and SWS. (c) Sheet resistance versus n at 10 K. The dashed line is a guide for eye.

ground state by the compressive heteroepitaxial strain. A similar behavior is observed in the 15 u.c. SWS, indicating that quantum confinement is playing a secondary role for thicker slabs, *i.e.* in the 3D regime. However, upon shrinking the quantum well to 10 u.c., while no significant change occurs to the low-temperature behavior in OLS, a MI transition clearly emerges in SWS at $\sim$100 K below which the resistance raises gradually with a sizable thermal hysteresis, manifesting a strong first order character of the transition. These observations mark the striking difference between the two confinement structures as they are compared in the inset of Fig. 5.8(b). Upon further reduction of the NNO slab thickness to 5 u.c., the enhanced quantum confinement facilitates an insulating ground state in OLS, due to the increased correlation/effective mass [71]. As seen in Fig. 5.8(a), below $\sim$140 K, the resistance becomes gradually increasing with decreasing temperature accompanied by a small thermal hysteresis between cooling and warming, characteristic of a weak first order MI transition. On the other hand, Fig. 5.8(b) shows that the insulating ground state is radically strengthened in SWS; the onset of the first order transition increases towards $\sim$200 K, below which the resistance is drastically raised by orders of magnitude and eventfully reaching the measurement limit below 40 K, denoting a strong MI transition. The sharp contrast with the 5 u.c.

slab in OLS can also be readily seen in the inset of Fig. 5.8(a) when the resistance data taken on warming are plotted together. An extrapolation for the 5-u.c. SWS suggests that the resistance jump differs by more than three orders of magnitude from that of the OLS.

From the observations described above, one can clearly see that, while both types of confinement structures undergo a dimensionality-controlled MI transition, the correlated electrons in NNO quantum wells of OLS and SWS display drastically different behavior in proximity to the 2D regime. These results unambiguously demonstrate that, when coupled with quantum confinement, the interface has a tremendous effect on driving the MI transition and the underlying collective long-range ordering. In connection to this, it is interesting to note that due to the reduced coordination of a top atomic layer, the surface is usually believed to have enhanced correlations [51]. In variance, this surface effect is ruled out by the suppressed MI transition in OLS. Since NNO represents an iconic example of synergetic CO and SO [11, 58], the suppression/enhancement of these collective electronic behaviors in the quantum well regime accentuates the pivotal role of the confining boundary. Specifically, the strong first order MI transition in SWS implies that the ordered insulating phase is favored by the interface with LAO. The surface, on the other hand, effectively suppresses these orderings and the first order character of the transition in OLS, and opposes the carrier localization driven by confinement-induced correlations as the electrons remain relatively mobile. Given that the NNO slab interfaces with LAO on the other side, the effect of the surface in destabilizing CO and SO is conceivably much stronger than that in OLS. Moreover, note that the appearance of the first order MIT at the dimensional crossover in NNO quantum wells is in sharp contrast with the observed second order MI transition and Néel transition in confined LNO [86, 8]. One possible reason is that the NFL metallic ground state in compressively strained NNO is much closer than that in LNO to the instability of the charge-ordered AFI phase in the 3D regime, as showed in the phase diagram in Chapter 4. The proximity to this quantum criticality may render the 3D-like CO/SO a much stronger competing phase in confined NNO during the dimensional crossover.

While the spin degeneracy of localized d-electrons is lifted via SO, CO in single valent systems

like $RNiO_3$ is to remove the e_g orbital degeneracy via charge disproportionation (e.g. $2Ni^{III} \longrightarrow Ni^{II} + Ni^{IV}$), instead of the typical Jahn-Teller route [56], as mentioned in Chapter 1. In addition, the orbital physics has also been suggested to be crucial in realizing the cuprate-like behavior in heterostructured e_g^1-systems [14, 31]. To gain further microscopic insight in to the orbital response, we have performed detailed resonant soft X-ray absorption measurements at the Ni *L*-edge with linear polarization-dependence. To precisely determine the charge state, all spectra were aligned to a NiO standard measured simultaneously with the samples. Here we will focus on the 5-u.c. quantum wells with the absorption data for bulk NNO included for direct comparison. First, we note, that for the given small thicknesses of the NNO slab ($\sim$ 2 nm) and the top LAO slab ($\sim$1.2 nm), the fluorescence-yield signal is very weak, but the electron-yield probing depth ($\gtrsim$12 nm) is significantly larger than the total film thicknesses of both OLS and SWS; thus, in either case, the NNO slab is assumed to be uniformly probed. Moreover, the Ni L_3-edge is overlapped by the intense La M_4-edge from LAO, rendering the lineshape distortion. From the distortion-free L_2-edge (see Fig. 5.9), however, one can observe that the spectra of the NNO quantum wells taken at 300 K are similar to those of the bulk [57, 78], indicative of a Ni^{3+} charge state of the low-spin configuration (S=1/2). In particular, the spectra consist of a main peak at $\sim$871.2 eV and a weak shoulder at the low-energy side due to the multiplet structure. This spectral lineshape can be well described by the strong mixing of the d^7 and $d^8\underline{L}$ configurations, as discussed in the first section. Meantime, a direct comparison of the spectra shows that, while the low-energy shoulder at the L_2-edge is smeared in the bulk, this feature emerges stronger in the quantum well regime and has been attributed to the reduced effective dimension in the previous sections.

Next, both OLS and SWS exhibit linear polarization-dependence across at the L_2-edge (see Fig. 5.9). As seen at the bottom of Fig. 5.9, this dependence is further substantiated by the difference spectra ($I_{E\|c} - I_{E\perp c}$). In particular, the difference spectra in OLS and SWS share a similar lineshape. We recap that the presence of XLD is the signature of charge anisotropy due to reduced local symmetry. The larger negative dichroic spectral weight at the high-energy side of both edges indicates that the overall absorption cross section is smaller with $E \parallel c$, implying a preferential

electron (hole) occupation of the $3z^2 - r^2$ ($x^2 - y^2$) orbital in both OLS and SWS. This assignment of orbital polarization is consistent with that of the NiO_6 octahedron distorted by compressive strain. On the other hand, one can see that the orbital polarization is substantially larger in OLS than in SWS; the linear dichroic effect in OLS is about three times of that in SWS. The relative suppression of the $3z^2 - r^2$ orbital polarization in SWS strongly implies that the confining interface stabilizes the preferential occupation of the $x^2 - y^2$ orbital for the e_g electron, opposing the crystal field effect of compressive strain. This effect of the confining block originates from the interfacial interaction between Ni and Al across the apical oxygen, as showed in the previous section. In contrast, the absence of the confining layer on one side of the quantum well selects the $3z^2 - r^2$ orbital character, acting synergetically with the compressive strain; this observation is in good agreement with the recent density functional theory calculations [32].

Identifying this counteracting effect between SWS and OLS in lifting orbital degeneracy elucidates the underlying role of the confining boundary in controlling the collectively ordered correlated ground state and the first order MIT of the quantum wells. Specifically, while Jahn-Teller distortion is characteristic of orbitally degenerate d-electrons in the strong interaction limit, CO (charge disproportionation) instability coupled with carrier localization has been shown to be a potent competing pathway to lift the orbital degeneracy on the verge of the localized-to-itinerant crossover in charge-transfer compounds [56]. This is due to the energy gain in the Hund's coupling which overcomes the reduced loss in Coulomb interaction. This mechanism is particularly efficient in charge-transfer systems such as $RNiO_3$ where charges fluctuate strongly via $d^7 \longleftrightarrow d^8\underline{L}$ and the charge-disproportionated Ni^{IV} site can be readily stabilized by forming a singlet state from the $d^7\underline{L}$ and $d^8\underline{L}^2$ configurations rather than creating the energetically unfavorable d^6 state. In fact, this CO picture has been successfully applied to explain the complex SO in $RNiO_3$ with the absence of orbital ordering [61]. The CO instability, however, would be naturally suppressed when orbital splitting is artificially introduced and/or enhanced *e.g.* in quantum well structures. As a result, in the critical region of the quantum confinement, when the interface compensates the orbital splitting induced by strain, the CO instability initiates the strong MIT in SWS, In contrast,

the ordered insulating ground state is rapidly weakened in OLS and the in-plane charge fluctuation $d^7_{3z^2-r^2} \longleftrightarrow d^8\underline{L}_{x^2-y^2}$ becomes more stable, as the orbital polarization is increased. This difference in the propensity to CO instability between OLS and SWS is further amplified by the absence of Madelung potential from the confining LAO layer on one side of OLS; as the prerequisite to the e_g orbital degeneracy, the d^7 configuration is stabilized by the Madelung potential.

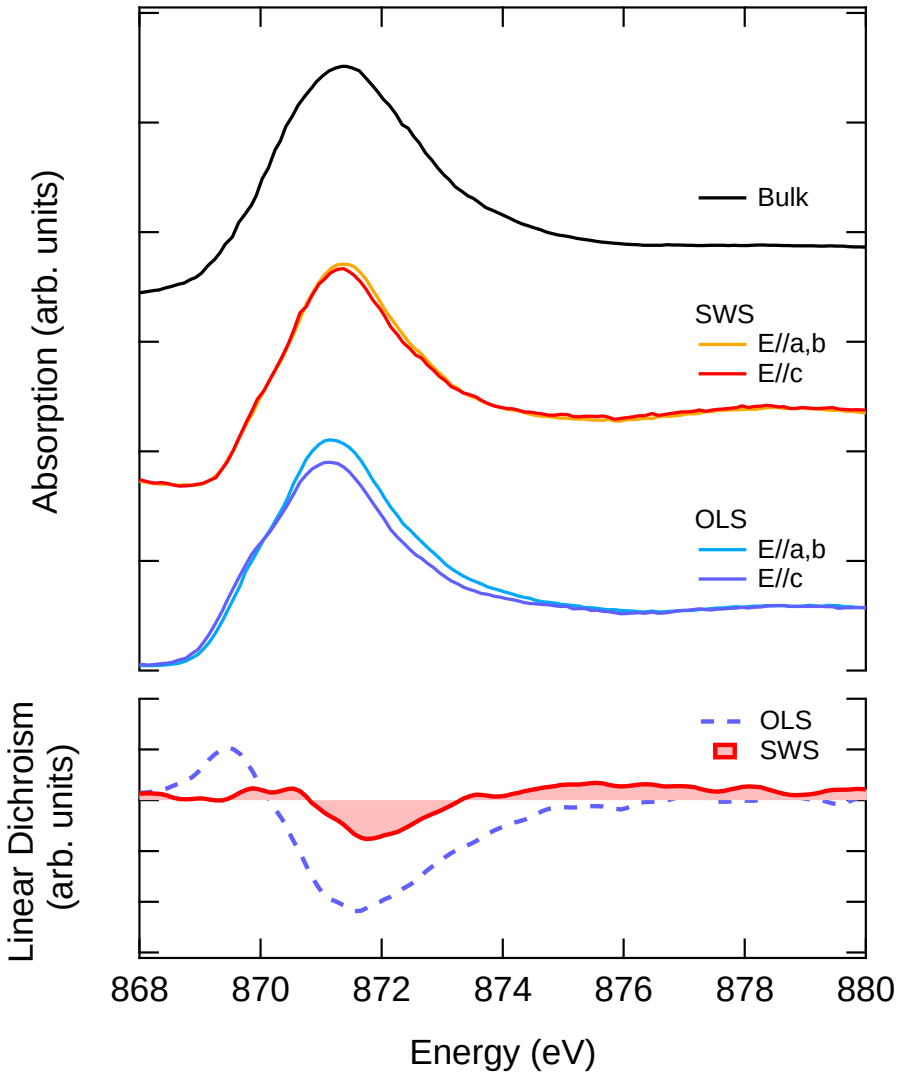

Figure 5.9: Polarization-dependent Ni L-edge x-ray absorption spectrum (upper) and linear dichroism spectra (lower) ($I_{E\|c} - I_{E\|a,b}$) of 5-u.c. slabs of $NdNiO_3$ in OLS and SWS. Absorption spectrum of bulk $NdNiO_3$ is included for comparison. Note, different samples are compared by normalization to the whiteline intensity at the L_2-edge.

Chapter 6

Summary and Future Prospects

6.1 Conclusions

We have developed the Layer-by-layer growth for synthesizing fully epitaxial ultrathin layers of $RNiO_3$ (R = rare earth) by pulsed laser deposition with *in situ* reflection high energy electron diffraction monitoring. In virtue of this digital growth control, both ultrathin films and heterostructures of $RNiO_3$ were synthesized under different heteroepitaxial strains on a variety of substrates. Atomic force microscopy imaging, synchrotron-based x-ray diffraction and x-ray absorption studies have confirmed the excellent morphology and bulk-like stoichiometry of the samples. The high quality of the samples is also reflected on the fact that the bulk like metallic ground state can be maintained in ultrathin films as thin as 10 unit cells ($\lesssim$4 nm) under large tensile strains, while reported results in literature show that similar samples grown without *in situ* control are semiconductors.

By monitoring the Ni valence state as the control parameter, the effect of polarity mismatch on the electronic properties of $LaNiO_3/LaAlO_3$ superlattices was also investigated. The initial growth stage is found to experience marked changes of the Ni electronic structure. We suggest that to a large extent these results can be consistently explained by a tri-layer growth model. Growing a buffer layer is found to efficiently circumvent the polarity mismatch issue and allows to preserve the electronically active Ni ions from changing the valence. These findings indicate a chemical pathway to resolve the polarity mismatch, which can be relevant for a wide range of complex oxides and should pave a way to the growth of ultrathin heterostructures with controlled electronic state of transition metal ions.

Having the growth established, we used resonant x-ray absorption spectroscopy combined with linear polarization-dependence to study the e_g orbital splitting in $LaNiO_3$ subject to heteroepitaxial

strain. A fundamental asymmetry in the orbital-lattice reconstruction to the sign of the heteroepitaxial strain was revealed. An excellent control of heteroepitaxial strain on Ni-O covalency was also uncovered. The results show that both the bandwidth and the Madelung energy are systematically tuned, signifying a self-doping mechanism. As a result, we are able to drive $NdNiO_3$ across the quantum metal-insulator transition. In particular, a rapid collapse of the antiferromagnetic ordering within the insulating phase was observed, corroborating that, while the magnetic ordering consists of the local Ni moments, the exchange coupling is mediated by the self-doped ligand holes. The emerging insulating phase without long-range magnetic orderings may serve as a candidate for spin liquid. Optical measurements across the metal-insulator transition confirmed that the carrier localization is driven by strong electron-electron repulsion, while the charge and spin orderings play a triggering role in initiating the transition.

After exploring the physics in the ultrathin films and their the strain-dependence, we investigated the quantum confinement effects on the electronic properties of correlated e_g^1 quantum wells. When the dimensionality of the confined $LaNiO_3$ layer was lowered in $LaNiO_3$/$LaAlO_3$ superlattices, enhanced electron correlations were observed to drive an emergent Mott-type MIT with the latent competing state of charge ordering. X-ray absorption spectroscopy indicated that an reduction of the apical ligand hole density due the strong ionicity of the Ni-O-Al bond. This interfacial interaction also induces e_g orbital polarization, as revealed by further studies with linear polarization-dependence on one-unit-cell-thick $LaNiO_3$ layer in $LaNiO_3$/$LaAlO_3$ superlattices. This result demonstrated new opportunities to control orbital configurations in ultrathin oxide heterostructures even in the absence of strain. Finally, to explicitly show the crucial role of the interface in defining the many-body ground state of correlated electrons, we investigated two different confinement geometries of $NdNiO_3$ quantum wells. The direct comparison under the stringent dimensionality-control unambiguously illustrated the constructive coupling between the interfacial effect and the quantum confinement. In particular, by modulating the e_g orbital splitting with different interfacial conditions, the charge-ordered insulating phase many be enhanced or suppressed.

6.2 Future Work

Following the work in this dissertation, an important direction is to tune the carrier concentration in the e_g^1 quantum wells by electric field gating. Carrier doping has been one of the most powerful and crucial ways to control electronic phases in both correlated systems and conventional semiconductors. Electric field gating is not only a clean method for this purpose, but also naturally sets up a platform for device applications. It will be very interesting to see what phases carrier doping drives the confined $RNiO_3$ into. If the observed insulating ground in the two dimensional regime is indeed similar to the parent phase of cuprate, carrier doping may introduce superconductivity. Even if superconductivity is absent, achieving gating-control on the metal-insulator transition is already a big step toward realizing novel electronics with Mott materials, so-called Mottronics.

Another important topic will be to explore the nature of the ground state of the e_g^1 quantum wells, particularly the spin degree of freedom. This is true not only for this system but also for other complex oxide heterostructures. In fact, the key distinction of correlated electron systems from conventional materials described by band theory is the presence of magnetism, due to the fact that correlation is governed by local atomic-like physics, e.g. the Hund's rules. However, when ferromagnetism is absent, there is a very limited number of experimental tools for probing magnetic orderings, especially antiferromagnetic ordering, in ultrathin heterostructures, which is a major roadblock for understand the physics at correlated interfaces. Neutron scattering which is the main technique used for bulk crystals fails to this task simply because it requires a large amount of sample material to obtain an observable signal. Conventional magnetization or magnetic susceptibility measurements also experiences the same problem due to the presence of signals from other sources, such as the substrates and magnetic contaminations. There are also spectroscopies, such as x-ray magnetic circular dichroism, muon spin spectroscopy, magneto-optic Kerr effect, and so on, but they are not directly sensitive to long-range orderings. One promising technique at this point is resonant x-ray diffraction, as we demonstrated in Chapter 4. The drawback is that one would need to know where to look within the reciprocal space.

From the material perspective, e_g^1 quantum wells grown along other crystallographic axes would be a highly intriguing subject. While the knowledge and experience gained from the (001)-oriented system can be great guides on the effects of strain and dimensionality, changing to another lattice plane to break the translational symmetry may lead to a very different landscape of electronic phases. An attractive example is the (111) direction where the quantum wells would have a two dimensional honey-comb lattice. Exotic behaviors such as topological phases have indeed been proposed. The interfacial couplings are expectedly much stronger since three of six oxygen ions of an octahedral contribute to the formation of the interface.

References

[1] K. H. Ahn, T. Lookman, and A. R. Bishop. *Nature*, 428:401, 2004.

[2] J. A. Alonso, J. L. Garcia-Munoz, M. T. Fernandez-Diaz, M. A. G. Aranda, M. J. Martinez-Lope, and M. T. Casais. *Physical Review Letters*, 82:3871, 1999.

[3] D. N. Basov, R. D. Averitt, D. van der Marel, M. Dressel, and K. Haule. *Reviews of Modern Physics*, 83:471, 2011.

[4] J. G. Bednorz. *Nature Materials*, 6:821, 2007.

[5] E. Benckiser, M. W. Haverkort, S. Bruck, E. Goering, S. Macke, A. Frano, X. P. Yang, O. K. Andersen, G. Cristiani, H. U. Habermeier, A. V. Boris, I. Zegkinoglou, P. Wochner, H. J. Kim, V. Hinkov, and B. Keimer. *Nature Materials*, 10:189, 2011.

[6] P. Blaha, K. Schwarz, GKH Madsen, D. Kvasnicka, and J. Luitz. *An Augmented Plane Wave + Local Orbitals Program for Calculating Crystal Properties*. K. Schwarz, Techn. Uni. Wien, Austria, 2001.

[7] D. H. A. Blank, G. Koster, G. Rijnders, E. van Setten, P. Slycke, and H. Rogalla. *Journal of Crystal Growth*, 211:98, 2000.

[8] A. V. Boris, Y. Matiks, E. Benckiser, A. Frano, P. Popovich, V. Hinkov, P. Wochner, M. Castro-Colin, E. Detemple, V. K. Malik, C. Bernhard, T. Prokscha, A. Suter, Z. Salman, E. Morenzoni, G. Cristiani, H. U. Habermeier, and B. Keimer. *Science*, 332:937, 2011.

[9] A. Brinkman, M. Huijben, M. Van Zalk, J. Huijben, U. Zeitler, J. C. Maan, W. G. Van der Wiel, G. Rijnders, D. H. A. Blank, and H. Hilgenkamp. *Nature Materials*, 6:493, 2007.

[10] M. Caffarel and W. Krauth. *Physical Review Letters*, 72:1545, 1994.

[11] G. Catalan. *Phase Transitions*, 81:729, 2008.

[12] J. Chakhalian, J. W. Freeland, H. U. Habermeier, G. Cristiani, G. Khaliullin, M. van Veenendaal, and B. Keimer. *Science*, 318:1114, 2007.

[13] J. Chakhalian, J. W. Freeland, G. Srajer, J. Strempfer, G. Khaliullin, J. C. Cezar, T. Charlton, R. Dalgliesh, C. Bernhard, G. Cristiani, H. U. Habermeier, and B. Keimer. *Nature Physics*, 2:244, 2006.

[14] J. Chaloupka and G. Khaliullin. *Physical Review Letters*, 100:016404, 2008.

[15] C. T. Chen, F. Sette, Y. Ma, M. S. Hybertsen, E. B. Stechel, W. M. C. Foulkes, M. Schluter, S. W. Cheong, A. S. Cooper, L. W. Rupp, B. Batlogg, Y. L. Soo, Z. H. Ming, A. Krol, and Y. H. Kao. *Physical Review Letters*, 66:104, 1991.

[16] F. C. Chou, N. R. Belk, M. A. Kastner, R. J. Birgeneau, and A. Aharony. *Physical Review Letters*, 75:2204, 1995.

[17] D. B. Chrisey and G. K. Hubler. *Pulsed Laser Deposition*. New York: John Wiley and Sons, 1994.

[18] S. Ciuchi and S. Fratini. *Physical Review B*, 77:205127, 2008.

[19] N. Combe and P. Jensen. *Physical Review B*, 57:15553, 1998.

[20] E. Dagotto. *Science*, 309:257, 2005.

[21] F. de Groot and A. Kotani. *Core Level Spectroscopy of Solids*. CRC Press, 2008.

[22] J. W. Freeland, J. Chakhalian, H.-U. Habermeier, G. Cristiani, and B. Keimer. *Applied Physics Letters*, 90:242502, 2007.

[23] J. W. Freeland, J. C. Lang, G. Srajer, R. Winarski, D. Shu, and D. M. Mills. *Review of Scientific Instruments*, 73:1408, 2002.

[24] D. Fuchs, E. Arac, C. Pinta, S. Schuppler, R. Schneider, and H. V. von Lohneysen. *Physical Review B*, 77:014434, 2008.

[25] J. L. Garcia-Munoz, M. A. G. Aranda, J. A. Alonso, and M. J. Martinez-Lope. *Physical Review B*, 79:134432, 2009.

[26] J. L. Garcia-Munoz, J. Rodriguez-Carvajal, and P. Lacorre. *Physical Review B*, 50:978, 1994.

[27] J. B. Goodenough. *Journal of Solid State Chemistry*, 127:126, 1996.

[28] O. Y. Gorbenko, S. V. Samoilenkov, I. E. Graboy, and A. R. Kaul. *Chemistry of Materials*, 14:4026, 2002.

[29] A. Gozar, G. Logvenov, L. F. Kourkoutis, A. T. Bollinger, L. A. Giannuzzi, D. A. Muller, and I. Bozovic. *Nature*, 455:782, 2008.

[30] A. X. Gray, A. Janotti, J. Son, J. M. LeBeau, S. Ueda, Y. Yamashita, K. Kobayashi, A. M. Kaiser, R. Sutarto, H. Wadati, G. A. Sawatzky, C. G. van de Walle, S. Stemmer, and C. S. Fadley. *Physical Review B*, 84:075104, 2011.

[31] M. J. Han, C. A. Marianetti, and A. J. Millis. *Physical Review B*, 82:134408, 2010.

[32] M. J. Han and M. van Veenendaal. *Physical Review B*, 84:125137, 2011.

[33] P. Hansmann, A. Toschi, X. P. Yang, O. K. Andersen, and K. Held. *Physical Review B*, 82:235123, 2010.

[34] P. Hansmann, X. P. Yang, A. Toschi, G. Khaliullin, O. K. Andersen, and K. Held. *Physical Review Letters*, 103:016401, 2009.

[35] T. Higuchi, Y. Hotta, T. Susaki, A. Fujimori, and H. Y. Hwang. *Physical Review B*, 79:075415, 2009.

[36] T. Holden, H.-U. Habermeier, G. Cristiani, A. Golnik, A. Boris, A. Pimenov, J. Humlicek, O. I. Lebedev, G. Van Tendeloo, B. Keimer, and C. Bernhard. *Physical Review B*, 69:064505, 2004.

[37] W. Hong, H. N. Lee, M. Yoon, H. M. Christen, D. H. Lowndes, Z. G. Suo, and Z. Y. Zhang. *Physical Review Letters*, 95:095501, 2005.

[38] K. Horiba, R. Eguchi, M. Taguchi, A. Chainani, A. Kikkawa, Y. Senba, H. Ohashi, and S. Shin. *Physical Review B*, 76:155104, 2007.

[39] S. Hormoz and S. Ramanathan. *Solid-State Electronics*, 54:654, 2010.

[40] M. Huijben, A. Brinkman, G. Koster, G. Rijnders, H. Hilgenkamp, and D. H. A. Blank. *Advanced Materials*, 21:1665, 2009.

[41] A. Ichimiya and P. I. Cohen. *Reflection High-Energy Electron Diffraction*. Cambridge University Press, 2004.

[42] M. Imada, A. Fujimori, and Y. Tokura. *Reviews of Modern Physics*, 70:1039, 1998.

[43] G. Jackeli and G. Khaliullin. *Physical Review Letters*, 101:216804, 2008.

[44] P. Jensen and B. Niemeyer. *Surface Science*, 384:L823, 1997.

[45] M. Kawasaki, K. Takahashi, T. Maeda, R. Tsuchiya, M. Shinohara, O. Ishiyama, T. Yonezawa, M. Yoshimoto, and H. Koinuma. *Science*, 266:1540, 1994.

[46] D. I. Khomskii. *Lithuanian Journal of Physics*, 37:65, 1997.

[47] D. I. Khomskii and J. van den Brink. *Physical Review Letters*, 85:3329, 2000.

[48] G. Kotliar, S. Y. Savrasov, G. Palsson, and G. Biroli. *Physical Review Letters*, 87:186401, 2001.

[49] P. Lacorre, J. B. Torrance, J. Pannetier, A. I. Nazzal, P. W. Wang, and T. C. Huang. *Journal of Solid State Chemistry*, 91:225, 1991.

[50] S. B. Lee, R. Chen, and L. Balents. *Physical Review B*, 84:165119, 2011.

[51] Liebsch. *Physical Review Letters*, 90:096401, 2003.

[52] G. Logvenov, A. Gozar, and I. Bozovic. *Science*, 326:699, 2009.

[53] J. Mannhart and D. G. Schlom. *Science*, 327:1607, 2010.

[54] S. J. May, J. W. Kim, J. M. Rondinelli, E. Karapetrova, N. A. Spaldin, A. Bhattacharya, and P. J. Ryan. *Physical Review B*, 82:014110, 2010.

[55] S. J. May, P. J. Ryan, J. L. Robertson, J.-W. Kim, T. S. Santos, E. Karapetrova, J. L. Zarestky, X. Zhai, S. G. E. te Velthuis, J. N. Eckstein, S. D. Bader, and A. Bhattacharya. *Nature Materials* , 8:892, 2009.

[56] I. I. Mazin, D. I. Khomskii, R. Lengsdorf, J. A. Alonso, W. G. Marshall, R. A. Ibberson, A. Podlesnyak, M. J. Martinez-Lope, and M. M. Abd-Elmeguid. *Physical Review Letters*, 98:176406, 2007.

[57] M. Medarde, A. Fontaine, J. L. Garciamunoz, J. Rodriguezcarvajal, M. Desantis, M. Sacchi, G. Rossi, and P. Lacorre. *Physical Review B*, 46:14975, 1992.

[58] M. L. Medarde. *Journal of Physics-Condensed Matter*, 9:1679, 1997.

[59] W. Meevasana, P. D. C. King, R. H. He, S. K. Mo, M. Hashimoto, A. Tamai, P. Songsiriritthigul, F. Baumberger, and Z. X. Shen. *Nature Materials*, 10:114, 2011.

[60] T. Mizokawa, A. Fujimori, T. Arima, Y. Tokura, N. Mori, and J. Akimitsu. *Physical Review B*, 52:13865, 1995.

[61] T. Mizokawa, D. I. Khomskii, and G. A. Sawatzky. *Physical Review B*, 61:11263, 2000.

[62] M. Mori, G. Khaliullin, T. Tohyama, and S. Maekawa. *Physical Review Letters*, 101:247003, 2008.

[63] N. F. Mott. *Philosophical Magazine*, 26:1015, 1972.

[64] D. A. Muller, N. Nakagawa, A. Ohtomo, J. L. Grazul, and H. Y. Hwang. *Nature*, 430:657, 2004.

[65] N. Nakagawa, H. Y. Hwang, and D. A. Muller. *Nature Materials*, 5:204, 2006.

[66] N. M. Nemes, M. Garcia-Hernandez, S. G. E. te Velthuis, A. Hoffmann, C. Visani, J. Garcia-Barriocanal, V. Pena, D. Arias, Z. Sefrioui, C. Leon, and J. Santamaria. *Physical Review B*, 78:094515, 2008.

[67] C. Noguera and J. Goniakowski. *Journal of Physics-Condensed Matter*, 20:264003, 2008.

[68] X. Obradors, L. M. Paulius, M. B. Maple, J. B. Torrance, A. I. Nazzal, J. Fontcuberta, and X. Granados. *Physical Review B*, 47:12353, 1993.

[69] A. Ohtomo and H. Y. Hwang. *Nature*, 427:423, 2004.

[70] A. Ohtomo, D. A. Muller, J. L. Grazul, and H. Y. Hwang. *Nature*, 419:378, 2002.

[71] S. Okamoto. *Physical Review B*, 84:201305(R), 2011.

[72] M. Ortolani, P. Calvani, and S. Lupi. *Physical Review Letters*, 94:067002, 2005.

[73] W. J. Padilla, D. Mandrus, and D. N. Basov. *Physical Review B*, 66:035120, 2002.

[74] V. Pardo and W. E. Pickett. *Physical Review Letters*, 102:166803, 2009.

[75] S. K. Park, T. Ishikawa, and Y. Tokura. *Physical Review B*, 58:3717, 1998.

[76] V. Pena, Z. Sefrioui, D. Arias, C. Leon, J. Santamaria, M. Varela, S. J. Pennycook, and J. L. Martinez. *Physical Review B*, 69:224502, 2004.

[77] R. Pentcheva and W. E. Pickett. *Physical Review Letters*, 102:107602, 2009.

[78] C. Piamonteze, F. M. F. de Groot, H. C. N. Tolentino, A. Y. Ramos, N. E. Massa, J. A. Alonso, and M. J. Martinez-Lope. *Physical Review B*, 71:020406, 2005.

[79] M. M. Qazilbash, M. Brehm, G. O. Andreev, A. Frenzel, P. C. Ho, B. G. Chae, B. J. Kim, S. J. Yun, H. T. Kim, A. V. Balatsky, O. G. Shpyrko, M. B. Maple, F. Keilmann, and D. N. Basov. *Physical Review B*, 79:075107, 2009.

[80] F. Rivadulla, J. S. Zhou, and J. B. Goodenough. *Physical Review B*, 67:165110, 2003.

[81] A. Ruegg and G. A. Fiete. *Physical Review B*, 84:201103(R), 2011.

[82] J. Salafranca and S. Okamoto. *Physical Review Letters*, 105:256804, 2010.

[83] A. Sambri, S. Amoruso, X. Wang, F. M. Granozio, and R. Bruzzese. *Journal of Applied Physics*, 104:2975363, 2008.

[84] R. D. Sanchez, M. T. Causa, A. Caneiro, A. Butera, M. ValletRegi, M. J. Sayagues, J. GonzalezCalbet, F. GarciaSanz, and J. Rivas. *Physical Review B*, 54:16574, 1996.

[85] D. D. Sarma, N. Shanthi, and P. Mahadevan. *Journal of Physics-Condensed Matter*, 6:10467, 1994.

[86] R. Scherwitzl, S. Gariglio, M. Gabay, P. Zubko, M. Gibert, and J. M. Triscone. *Physical Review Letters*, 106:246403, 2011.

[87] R. Scherwitzl, P. Zubko, C. Lichtensteiger, and J. M. Triscone. *Applied Physics Letters*, 95:3269591, 2009.

[88] Z. Sefrioui, D. Arias, V. Pena, J. E. Villegas, M. Varela, P. Prieto, C. Leon, J. L. Martinez, , and J. Santamaria. *Physical Review B*, 67:214511, 2003.

[89] S. S. A. Seo, M. J. Han, G. W. J. Hassink, W. S. Choi, S. J. Moon, J. S. Kim, T. Susaki, Y. S. Lee, J. Yu, C. Bernhard, H. Y. Hwang, G. Rijnders, D. H. A. Blank, B. Keimer, and T. W. Noh. *Physical Review Letters*, 104:036401, 2010.

[90] J. Son, P. Moetakef, J. M. LeBeau, D. Ouellette, L. Balents, S. J. Allen, and S. Stemmer. *Applied Physics Letters*, 96:062114, 2010.

[91] J. Stahn, J. Chakhalian, Ch. Niedermayer, J. Hoppler, T. Gutberlet, J. Voigt, F. Treubel, H-U. Habermeier, G. Cristiani, B. Keimer, and C. Bernhard. *Physical Review B*, 71:140509(R), 2005.

[92] U. Staub, G. I. Meijer, F. Fauth, R. Allenspach, J. G. Bednorz, J. Karpinski, S. M. Kazakov, L. Paolasini, and F. d'Acapito. *Physical Review Letters*, 88:126402, 2002.

[93] H. Takagi and H. Y. Hwang. *Science*, 327:1601, 2010.

[94] K. S. Takahashi, M. Kawasaki, and Y. Tokura. *Applied Physics Letters*, 79:1324, 2001.

[95] M. Takizawa, Y. Hotta, T. Susaki, Y. Ishida, H. Wadati, Y. Takata, K. Horiba, M. Matsunami, S. Shin, M. Yabashi, K. Tamasaku, Y. Nishino, T. Ishikawa, A. Fujimori, and H. Y. Hwang. *Physical Review Letters*, 102:236401, 2009.

[96] A. Tebano, C. Aruta, S. Sanna, P. G. Medaglia, G. Balestrino, A. A. Sidorenko, R. De Renzi, G. Ghiringhelli, L. Braicovich, V. Bisogni, and N. B. Brookes. *Physical Review Letters*, 100:137401, 2008.

[97] S. Thiel, G. Hammerl, A. Schmehl, C. W. Schneider, and J. Mannhart. *Science*, 313:1942, 2006.

[98] Y. Tokura and N. Nagaosa. *Science*, 288:462, 2000.

[99] G. van der Laan and B. T. Thole. *Physical Review Letters*, 60:1977, 1988.

[100] M. A. van Veenendaal and G. A. Sawatzky. *Physical Review B*, 50:11326, 1994.

[101] R. Werner, C. Raisch, A. Ruosi, B. A. Davidson, P. Nagel, M. Merz, S. Schuppler, M. Glaser, J. Fujii, T. Chasse, R. Kleiner, and D. Koelle. *Physical Review B*, 82:224509, 2010.

[102] P. R. Willmott, S. A. Pauli, R. Herger, C. M. Schleputz, D. Martoccia, B. D. Patterson, B. Delley, R. Clarke, D. Kumah, C. Cionca, and Y. Yacoby. *Physical Review Letters*, 99:155502, 2007.

[103] T. Wolfram and S. Elllaltioglu. *Electronic and Optical Properties of d-Band Perovskites*. Cambridge University Press, 2006.

[104] S. M. Wu, S. A. Cybart, P. Yu, M. D. Rossell, J. X. Zhang, R. Ramesh, and R. C. Dynes. *Nature Materials*, 9:756, 2010.

[105] X. Q. Xu, J. L. Peng, Z. Y. Li, H. L. Ju, and R. L. Greene. *Physical Review B*, 48:1112, 1993.

[106] S. Yamamoto and T. Fujiwara. *Journal of the Physical Society of Japan*, 71:1226, 2002.

[107] K.-Y. Yang, W. Zhu, D. Xiao, S. Okamoto, Z. Wang, and Y. Ran. *Physical Review B*, 84:201104(R), 2011.

[108] K. Yoshimatsu, T. Okabe, H. Kumigashira, S. Okamoto, S. Aizaki, A. Fujimori, and M. Oshima. *Physical Review Letters*, 104:147601, 2010.

[109] J. Zaanen, G. A. Sawatzky, and J. W. Allen. *Physical Review Letters*, 55:418, 1985.

[110] J. S. Zhou, J. B. Goodenough, and B. Dabrowski. *Physical Review Letters*, 94:226602, 2005.

[111] J. S. Zhou, J. B. Goodenough, B. Dabrowski, P. W. Klamut, and Z. Bukowski. *Physical Review Letters*, 84:526, 2000.

[112] J. S. Zhou, J. B. Goodenough, B. Dabrowski, P. W. Klamut, and Z. Bukowski. *Physical Review B*, 61:4401, 2000.